Design and Functionality of a Calcium-responsive CEST Contrast Agent for Hyperpolarized Nuclei

Dissertation

zur Erlangung des akademischen Grades
Dr. rer. nat. in Biochemie

vorgelegt im Juni 2022 von

Dipl.-Ing. Ursula Pfeiffer

am
Fachbereich Biologie, Chemie, Pharmazie
der Freien Universität Berlin

Verteidigt am 24.10.2022

Erstgutachter: Dr. rer. nat. Leif Schröder
Zweitgutachter: Prof. Dr. rer. nat. Christian Freund

Danksagung

Während der Promotion hatte ich das Privileg, sehr viel neues zu lernen, und gleichzeitig zu forschen. Das war unheimlich bereichernd und fordernd zugleich. Diese Promotion hat mich mit einigen neuen Fähigkeiten und Einblicken ausgestattet, die ich mir sonst wohl nie angeeignet hätte. Ich hatte außerdem die Möglichkeit, bestehende Kenntnisse und Fähigkeiten in einem ungeahnten Maß auszubauen. Die Unsicherheit, die mit der Entdeckung von etwas neuem wie cryptophan-CEST silencing einhergeht, entwickelte sich für mich zu einem Training des sachlichen Denkens und Entscheidens. Dafür bin ich sehr dankbar.

Ich bedanke mich bei meinen Eltern und meinem Bruder für Verständnis und Unterstützung in wirklich jeder Phase der Promotion. Eure offenen Ohren haben mir so viel Mut gegeben! Ihr wurdet nie müde, Euch die Geschichten aus meiner Forschung immer und immer wieder anzuhören. Ihr wart euch nie zu fein, auch mal nachzuhaken und zu diskutieren. Die Gespräche mit Euch waren immer konstruktiv, ehrlich und ermutigend. Ich danke meinem liebsten Freund, der mich mit seiner Faszination für Physik und Chemie nochmal daran erinnert hat, wie spannend es ist, zu experimentieren und zu forschen, und dann selbst kaum noch forschen konnte, weil er sich stundenlang um unseren Sohn gekümmert hat, damit ich diese Promotion machen kann. Ich danke auch unserem Sohn, denn er zeigt mir jeden Tag, was es alles zu erforschen gibt. Für ihn bin ich stärker, ruhiger und mutiger geworden.

Ich danke meinen KollegInnen, insbesondere Leif Schröder, der meine Arbeit von Anfang an betreut und unterstützt hat und sich immer wieder Zeit genommen hat, mich beim Einstieg in die Magnetresonanz mit HP-Xenon unermüdlich zu unterstützen, und mir für alle meine Vorträge und Poster, sowie jedes Kapitel dieser Dissertation wertvolles, ausführliches und konstruktives Feedback zu geben. Ich danke Dorothea Fiedler und dem FMP für die Verlängerung meiner Stelle während der Elternzeit und der Pandemie. Ich danke Christian Freund für etscheidende wertvolle Hinweise und offene Ohren für mein Projekt. Ich danke Christopher Witte für die Geduld, mir beim müh-

samen erlernen erster Python-codes zu helfen. Ich danke Patrick Schuenke für die Erstellung der PyCEST-GUI (sie hat mir die Datenanalyse so viel schöner gemacht!) aus diesen codes und für die Unterstützung beim Aufnehmen meiner ersten Bildgebungsdaten. Ich danke Jan Oliver Jost für die Synthese der bis jetzt kleinsten Cryptophan-CEST silencing-fähigen Moleküle, zahlreiche und gelegentlich auch kantige Diskussionen, die zum wissenschaftlichen Diskurs dazu gehören. Mein Dank geht an Jabadurai Jayapaul, der mir wirklich zahlreiche Fragen beantworten konnte, und mir wertvolle Lesetipps gegeben hat. Ich bedanke mich besonders bei Christian Freund, Matthias Müller, Kathrin Motzny, Heike Nikolenko, Sascha Lange, und Andreas Oder, die mich nicht nur einluden, in ihren Laboren meine Untersuchungen zu machen, sondern mich dabei sogar unterstützt haben. Mein Dank geht an meine mitpromovierenden Patrick Werner, Hen-Amit Morik und unseren Stipendiaten Tahoe Fiala für gute Fragen, konstruktive Gespräche und ein besonders respektvolles und angenehmes Miteinander, sowie für zahlreiche Handgriffe, die sie im Labor für mich während meiner Schwangerschaft erledigt haben.

Ich danke allen promovierenden am FMP, einer guten Gemeinschaft, mit der ich immer Ideen, Fragen, Freud und Leid teilen konnte, vor allem meinen Freundinnen Thais Gazzi, Petra Ryl und Annika Manns: Ihr habt mich immer daran erinnert, wo ich mit dieser Promotion hin wollte, und nie daran gezweifelt, dass ich auch dort ankomme. Ihr wart ein Sonnenschein an meinem Arbeitsplatz, egal bei welchem Wetter. Ich danke meinen KollegInnen und MentorInnen bei The Writing Academic, die mich beim Schreiben unter besonderen Bedingungen großartig motiviert und unterstützt haben.

Selbstständigkeitserklärung

Hierdurch versichere ich, dass ich diese Dissertation selbstständig verfasst und keine anderen als die von mir angegebenen Quellen und Hilfsmittel verwendet habe. Ich versichere, dass ich meine Dissertation nicht schon einmal in einem anderen Promotionsverfahren eingereicht habe.

I hereby assure that I have created this dissertation on my own and independently, and that I have used only the tools and resources that I declared. I assure that I have never submitted my dissertation in another doctorate examination procedure before.

Träger Dieser Arbeit

Diese Arbeit wurde in der Arbeitsgruppe von Dr. Leif Schröder am Forschungsinstitut für Molekulare Pharmakologie (FMP) in Berlin-Buch wissenschaftlich betreut und angefertigt.

Abstract

This thesis starts out by introducing the objective of the project. This first chapter also provides the reader with a basic understanding of the key principles of Molecular biosensing, intracellular calcium signaling and CaM, Cryptophane, NMR, Xenon NMR and Xenon HyperCEST in particular. The connection between all these very different topics will be provided alongside, in the introduction. The importance of intracellular calcium signaling is explained as part of the motivation for this project.

The chapter "Responsive MR Biosensors for Ca^{2+} Detection" illustrates the development of Ca^{2+} biosensing in research. This history of investigations resulted in many useful biosensors, which are becoming increasingly sensitive, specific and biocompatible. The chapter illustrates that there is a community of researchers, large and diverse in their fields, which pursue Ca^{2+} biosensing and imaging and the thereby gained possibilities to study neuronal patterns of all kinds and more. It also describes the many possibilities to measure and report intracellular Ca^{2+}, and how different approaches are used to measure that in NMR.

The aim is outlined and stated afterward, to clarify the motivation and objective of the project.

Then, the results of the study are described in the chapter "Results". Afterwards, the results are discussed and interpreted in the chapter "Discussion". The chapter "Summary, Conclusion and Outlook" features a short summary of the discussion, after which conclusions from the entire project are drawn. An Outlook is provided afterwards, to illustrate connection points for further research, or follow-up projects. Materials and Methods are explained at the end, as a repository of further information.

Zusammenfassung

Diese Dissertation beginnt mit der Motivation des Projekts, aus dem diese Promotion entspringt. Die Einleitung führt zunächst in die Grundkonzepte molekularer Biosensoren und intrazellulärer Kalziumsignale ein. Zentrale Moleküle wie Calmodulin und Cryptophan, sowie Schlüsselthemen wie NMR, insbesondere Xenon-NMR, spin-hyperpolarisation und HyperCEST-NMR werden vorgestellt. Diese sehr unterschiedlichen Themen werden außerdem in einen Zusammenhang gebracht. Die zentrale Rolle der Kalziumionen in der intrazellulären Kommunikation wird in diesem Zusammenhang erklärt. Die ubiquitäre und zentrale Bedeutung von Kalziumsignalen für die zelluläre Entwicklung lässt erkennen, warum anhaltend an ihrer Sichtbarmachung und Erforschung gearbeitet wird.
Das Kapitel „Responsive MR Sensors for Ca^{2+} Detection" veranschaulicht die Entwicklung von Ca^{2+} - Biosensoren in der Forschung. Im Verlauf der Forschung und Entwicklung an Ca^{2+} - Biosensoren sind viele und vielseitig nutzbare Biosensoren entstanden, die sich immer spezifischer und empfindlicher auf Kalziumsignale reagieren können. Auch die Verträglichkeit und Biokompatibilität dieser Biosensoren wird stetig verbessert. Die Forschung rund um Ca^{2+} - Biosensoren und Ca^{2+} - Bildgebung wird von Forscherinnen vieler verschiedener Fachrichtungen betrieben, von denen jede einen eigenen Blick auf Kalziumsignale und die ihnen zugrundeliegenden zellulären oder neuronalen Prozesse beiträgt. Diese Diversität wird auch in den vielen Möglichkeiten, Kalziumsignale zu messen, wiedergespiegelt. Allein für die Kernspinresonanz gibt es dafür unterschiedliche Ansätze, und es werden fortlaufend neue entwickelt.
Nach dieser Einführung wird das Ziel dieser Promotionsarbeit konkret und kurz formuliert. Anschließend werden die Ergebnisse im Kapitel „Results" beschrieben. Im darauf folgenden Kapitel „Discussion" werden diese Ergebnisse dann interpretiert und diskutiert. Das Kapitel „Summary, Conclusion and Outlook" fasst die Diskussion zusammen, um am Ende zu Schlussfolgerungen aus dem gesamten Projekt zu gelangen. Anschließend wird ein Ausblick gegeben, in dem Möglichkeiten beschrieben werden, gegebenenfalls aus anderen Fachrichtungen an das Projekt anzuknüpfen. Alle verwendeten Methoden und Materialien sind am Ende der Arbeit beschrieben.

Contents

1 Introduction

1.1 Key Tools and Concepts

1.1.1 Motivation: Calcium as a Target

An unusual intracellular calcium level is the very beginning of cell proliferation or death, and often the first sign of dysfunctional ion channels. Therefore intracellular calcium is an excellent target for early diagnosis. The most severe pathologies include unusual levels of intracellular calcium. Important channel proteins for calcium extrusion are missing or dysfunctional in multiple sclerosis patients and animal models, resulting directly in unnaturally high levels of intracellular calcium [47]. Lately, severe diseases have been found out to be channelopathies: several Cancers [52] and Alzheimer's Disease [79] are associated with a high intracellular calcium level at the beginning. The link between chronic hepatitis B and hepatic carcinoma is a protein, which elevates cytosolic calcium signals [94]. Ehling et al.propose that Multiple Sclerosis might be a channelopathy as well [23].

A comprehensive view of intracellular calcium levels has the potential to reveal sites of initiation of many of those diseases. Currently, clinical diagnosis requires a large enough damaged region of tissue (lesions, etc.). A calcium map of entire organs bears the potential of much earlier diagnosis.

1.1.2 Calcium Signaling

Calcium is an essential second messenger in all cells. The modulations in intracellular calcium concentration have characteristic patterns, either frequency or amplitude encoded. The calcium binding proteins of the cell receive this encoding pattern and react to it by recruiting other proteins. Which proteins are recruited, depends on the encoding pattern and the locus in the cell. Calcisomes, multi-protein aggregates, are assembled of these proteins, and execute further functions, effectively translating a calcium modulation and a spatiotemporal component into an aspect of cellular fate. Haiech's 2001 review [30] describes this role of calcium in the signaling context.

There are over 100 calcium binding proteins, and probably the most important one is calmodulin

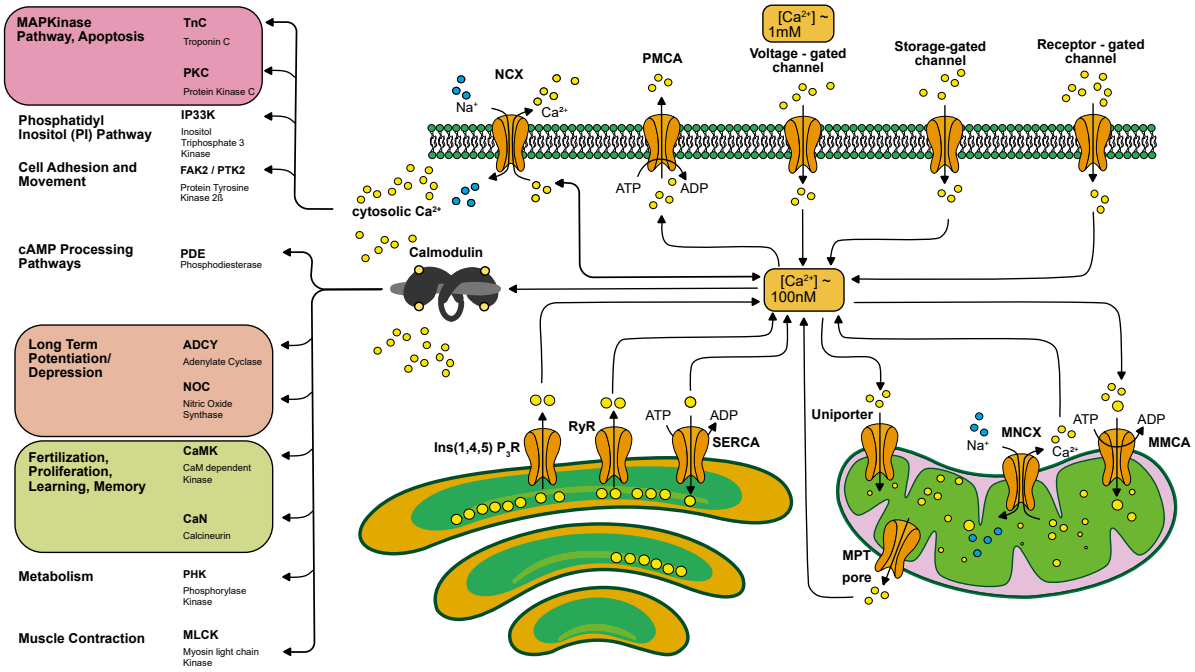

Figure 1.1: This non- exhaustive schematic calcium signaling map illustrates the calcium fluctuations in and out of the cell, and within it, the many pathways that are governed by calcium, and the pivotal role of CaM in this tightly controlled network of calcium signaling. It was adapted from ref. [13].

(CaM). "Similar to a hub, it [CaM] is central to a large and finely tuned network, receiving information, integrating it and dispatching the cognate response.", describes Haiech accurately in [30].

CaM regulates the calcium flux and homeostasis within the cell as well as the entry and exit of calcium into the cell via different channel proteins. Fig. 1.1 is a non-exhaustive schematic map of the calcium signaling network across the cell, illustrating how central CaM is to calcium signaling. The calcium transporting channel proteins can be roughly classified into voltage operated, ligand or receptor opterated, store operated and second messenger operated channels, and all of them can be influenced by CaM. An example for Calmodulation of a channel is the regulation of voltage-gated channels: One of their peripheral domains is preassociated with the calcium-free Apo-CaM. Upon calcium binding, subtle rearrangements of the conformation lead to a reduced ion transmission [10]. There are also active transport and diffusion of Ca^{2+} across the outer cell membrane and in and out of organelles, and these too are influenced by CaM. To buffer all in- and efflux to and from the cytoplasm and maintain calcium homeostasis, there are hundreds of different calcium-binding proteins, of which CaM is one. Calcium-binding proteins are distributed ubiquitously throughout

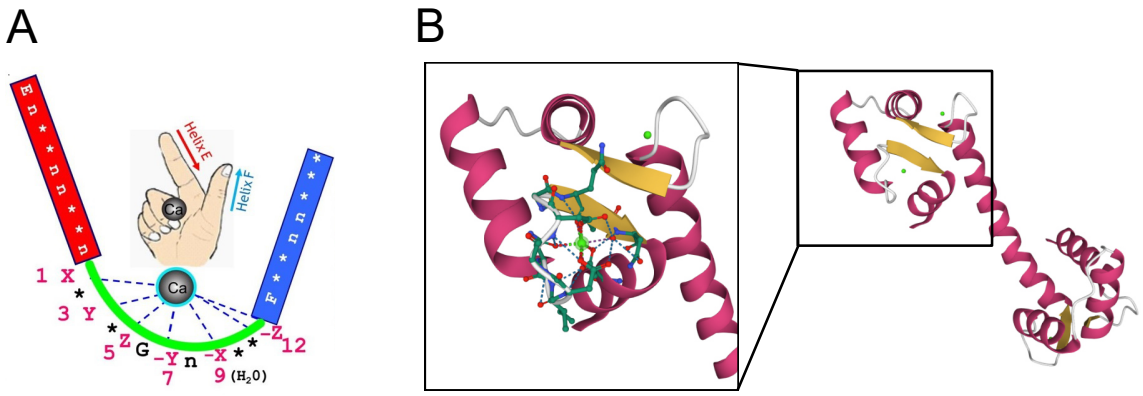

Figure 1.2: A: Schematic illustration of the conserved parts of the sequence and the functionality of the EF-Hand. Reprinted with permission from Zhou et al. [97]. B: PDB structure of Rat Calmodulin (CaM), according to the PDB identifier 3CLN [5]. Ca^{2+} ions are marked in green.

the cell, to absorb any excess of calcium ions.

The 174 residues of CaM are organized in two structurally similar domains, containing mainly two EF-hands per domain. The EF-hand is a structural motif that occurs across all life forms, and has developed to bind calcium by electrostatic interactions with negatively charged residues. The functional and structural principle of an EF-hand is illustrated in Fig.1.2A. With four EF-hands, one CaM molecule binds four calcium ions (as shown in Fig.1.2B), and is enabled to bend in the middle and ultimately translate this event into regulatory information.

CaM is not merely a calcium binding and buffering protein, as fig. 1.1 shows, but a very important regulatory signaling hub. It evolved to be optimal for binding the autoinhibitory domains of many regulatory proteins. It functions like a guided key, unlocking further signaling routes, and thereby the downstream flow of information. CaM has the ability to receive and transmit local calcium signals (by binding site specific targets) and global ones (by being ubiquitously present).

The two parts of CaM are connected by a long helical domain with a possibility to bend in the middle, allowing the two EF-hand-pairs to wrap tightly around the rod-shaped, helical binding partner. The PDB Structure shown in fig. 1.3, depicts the Ca^{2+} saturated CaM (also called Holo-CaM) bound tightly to a peptide in what is called the wrap-around binding. The target shown there is named M13, and it comprises the autoinhibitory domain of smooth muscle myosin light chain kinase (SMLCK), which is CaM's highest affinity target.

The helical peptides for this study are chosen to represent the canonical wrap-around binding mode. One of them is M13, shown in fig.1.3, and the other one is called RS20.

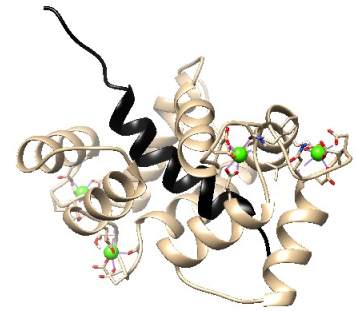

Figure 1.3: PDB structure 2BBM, according to Ikura et al.[34], showing human Holo-CaM bound to M13, an artificial peptide crafted to resemble the autoinhibitory domain of smooth muscle myosin light chain kinase. Ca^{2+} ions are marked in green

The helical CaM binding peptide can be very diverse in sequence, as the wide variety of CaM binding partners demand this high flexibility. Yet its helix propensity, amphiphilicity and anchor residues are conserved. The anchor residues are one or two hydrophobic residues which upon target recognition, are buried in hydrophobic, methionine-coated pockets within CaM, and so act as anchors, stabilizing CaM-target binding. In ref.[26], the authors explain the anchoring mechanism, and its pivotal role in target recognition and binding in more detail. By wrapping around it, CaM occupies the autoinhibitory domain of its target enzyme, thereby activating the enzyme and downstream regulatory cascades.

The enzyme or pathway types, which are listed on the left side of fig.1.1, indicate bundles of enzymes or effective downstream paths for calcium and CaM. For example, a calcium signal can begin with the CaM mediated activation of one kinase from a set of kinases, which phosphorylates another enzyme from a set of enzymes, which converts a substrate. The CaM dependent kinases, their target enzymes and their downstream substrates are numerous, this leads to a myriad of possible outcomes of a modulation in calcium concentration.

The highly sensitive signaling hub CaM is only present at very low concentrations. Wu and Bers report a total concentration of 2-25 µM CaM in cultured mammalian cells[92]. They also report free CaM concentrations of 50-74 nM in rabbit cardiac myocytes, which is less than 1% of the total CaM concentration. A study on the availability and motility[70] of i.c. CaM reported similar total CaM concentrations from an expression in HEK293 cells, and confirmed that the fraction of free CaM is very small. These two studies describe CaM mediated signaling as a harsh competition among the family of over 100 CaM binding proteins for the scarcely available CaM.

1.1.3 Molecular Biosensors

For most molecular analysis driven by electronic devices, i.e. spectrometers, magnetic and electrical fields or optical detectors, except for mass spectrometry and surface plasmon resonance, calcium in aqueous solution is indistinguishable from other divalent cations. The unperturbed observation of calcium ions requires additional reporting mechanisms. Especially for the observation of calcium in living cells and organisms, molecular biosensors are the only way to discriminate between the different divalent cations. The calcium signals shown in Fig.1.1 are among the first signs of calcium-related diseases. At the center of Fig.1.1 is a rough estimate of the resting calcium concentration in many cell types:100 nM. This concentration requires molecular biosensors with high sensitivity, especially considering how densely packed the cytosol is with other molecules. This is why molecular biosensors are absolutely essential for the development of early diagnosis methods of any calcium-related diseases. The definition of a biosensor is quite open. Generally, a biosensor is the missing link between the biological molecule of interest and the electronic device for detection. The detailed and elaborate IUPAC definition of a biosensor[62] shows that many different things and combinations can be a biosensor. What makes our molecule combination a biosensor is its two-component system, illustrated in Fig.1.4: There is a targeting unit and a detection unit, of which the biosensor consists. The targeting unit interacts specifically with biological target molecules, highlighted in green in Fig.1.4, indicating a biologically relevant event. The targeting unit is shown in light gray in Fig.1.4. It is a CaM-binding peptide, which binds to calcium-loaded CaM.

The reported biological event is the rise and fall of intracellular calcium levels. When CaM binds to the peptide, which is the targeting unit, this peptide influences the detection unit, the round molecule attached to the peptide in Fig.1.4. The detection unit emits a detectable and distinguishable signal, which can be physically measured by an electronic device. In this study, this signal is indicated by the graph in Fig.1.4. Many biosensors have detection units that are unconditionally detectable. This biosensor is only detectable under certain conditions, that are met when it is bound to the target. Because this is instantly reversible, the biosensor can respond to dynamic changes in calcium concentration. This makes our biosensor responsive.

In short, responsive biosensors have several main advantages:

- The biosensor reports not only on target presence, but also on target binding functionality
- Unbound biosensor molecules do not influence the measurement
- Dynamic changes of target binding activity can be recorded accurately

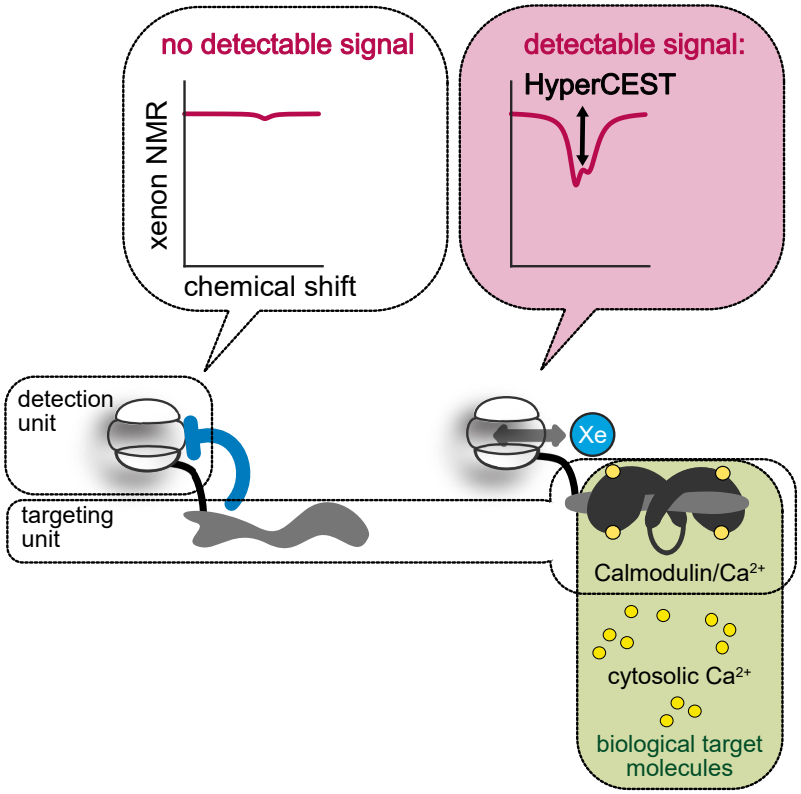

Figure 1.4: The biosensor principle, shown with the biosensor of this study. The components that make it a biosensor are marked ba the different boxes: The detectable signal, the detection unit, which issues the signal, the targeting unit, and the biological target molecule(s), with which the target unit can bind specifically. The green box illustrates the flexible definition of this biosensor: The native CaM of the cell can be viewed as part of the biosensor to sense calcium signals, or as biological target molecule, embodying calcium/CaM signaling.

Ideally, a response is the consequence of binding and another essential chemical interaction, e.g. metabolization or activation in combination. The next chapter features many examples of responsive MR biosensors for calcium detection.

1.1.4 Intermolecular Binding

In the cytoplasm, CaM-target binding is the association of two proteins, of which CaM often is the smaller one. The roles of receptor and ligand are irrelevant in that context. A ligand is just a molecule that binds to another molecule to serve a biological purpose. In the biochemical laboratory, when CaM is titrated with just the short binding region of a CaM-binding protein until excess, the pair can be declared as receptor and ligand, and corresponding models can be applied. Then, the binding reaction can be described as:

$$\mathrm{R} + \mathrm{L} \rightleftharpoons \mathrm{RL}$$

In the preliminary binding experiments of this study, one binding partner was a short peptide, and another was holo-CaM (CaM saturated with calcium) or apo-CaM (calcium-free CaM). To assess, the binding activity of CaM and the affinity for the modified peptides, titrations were performed. Because the measurable signal indicating formation of the binding complex originates from the peptide, the peptide concentration needed to remain constant, and holo-CaM was supplied until saturation. The conditions for a binding curve for this titration are met if one very unusual declaration is made: holo-CaM is regarded as the ligand, the peptide as the receptor. The biosensor in this study ultimately indicates tiny changes in the concentration of calcium ions. Sufficient CaM-peptide binding however, is only an essential prerequisite for this, but not the main goal. The main goal is to derive a binding constant for calcium, to match this biosensor's calcium affinity to a target calcium signal, and to compare this biosensor with others. Calcium titrations were performed, and several calcium-dependent binding processes lead to a measurable signal, the CEST effect. One of these binding processes is calcium-CaM binding. One CaM molecule can bind four calcium ions, and does this in a positively cooperative fashion. With every bound calcium ion, the affinity for calcium ions increases. In a living cell, the total concentration of free calcium ions is several orders of magnitude higher than the CaM concentration. However, these numbers vary spatially and temporally throughout the cell, and this variation is essentially the calcium signaling pattern.
With a certain calcium scarcity, the binding between peptide and CaM takes place in multiple variations at the same time. Not only holo-CaM can bind the peptide. All other calcium-containing CaM molecules bind the peptide at different rates with different affinities, ascending with the

number of bound calcium ions. The preliminary check for binding with holo-CaM and apo-CaM can only access a small excerpt of the actual molecular interplay at work. This is shown in a comprehensive figure by Valeyev et.al. [85], shown in Fig.1.5

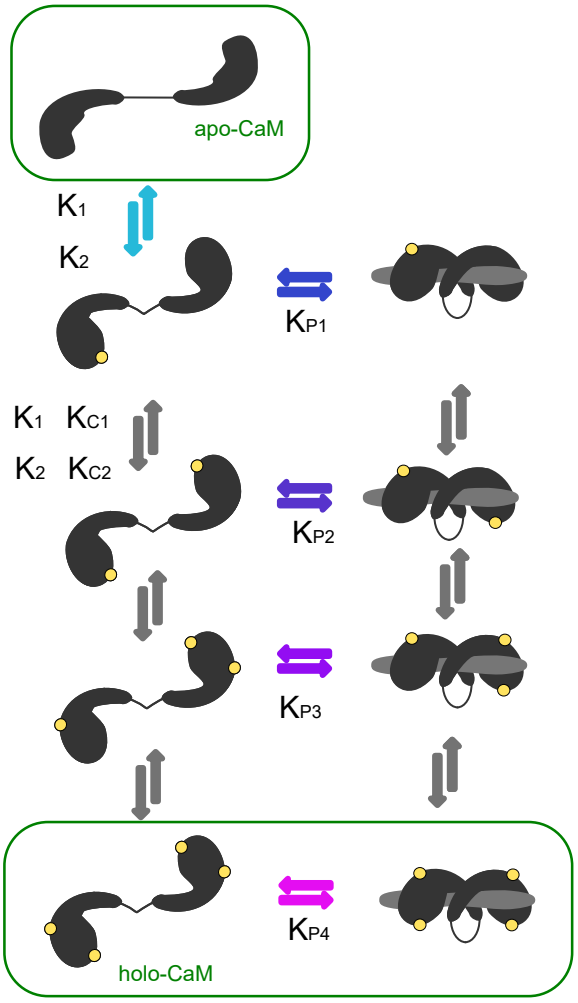

Figure 1.5: Schematic of Calcium-CaM-peptide interactions, under the assumption of cooperativity between the EF-hand motifs. Adapted from Valeyev et.al [85]. The colour of each arrow represents an individual set of association/dissociation equilibrium constants. Apo- and holo-CaM are framed in green.

Such cooperative multiple-site binding processes are best described with a sigmoidal curve. But also first-order binding reactions without cooperativity can have sigmoidal kinetcis. This is the case when a conformational change is induced by binding, or a mix of different isoforms of a binding partner is present [19]. During calcium-CaM-peptide binding, CaM undergoes several conformational

rearrangements, driven by calcium binding and peptide binding. The peptide changes conformation upon CaM binding, and peptide binding and calcium binding cooperate. Calcium-CaM-peptide binding probably is a superposition of several sigmoidal transition processes.

A.P. Hill began to develop a description of cooperative multiple-site binding in 1910, when they described oxygen binding to hemoglobin with the Hill equation and the Hill coefficient [31]. Many dose-response relationships are described using variants of the Hill equation, mainly because of its simplicity.

A dose-response-curve with a hill coefficient can be over-interpreted, and there are indeed more accurate descriptions of cooperative multiple-site binding [89] and the calcium-CaM-peptide system [85]. However, the aim of this study was not to describe the kinetics of the calcium-CaM-dependency of the CEST effect, but to quantify it roughly and to relate the calcium-CaM dependent CEST effect to possible targets and other similar biosensors. Moreover: the prerequisites for the Hill equation are met here: a high degree of positive cooperativity and true allostery (independent and individual calcium binding sites).

1.1.5 Nuclear Magnetic Resonance as a Diagnostic Tool

From the first description of the phenomenon of Nuclear Magnetic Resonance (NMR) by Isidor Rabi in 1938, for which Rabi received the Nobel prize in 1944, NMR went through an impressive history of discovery and development. Nowadays, NMR is a standard tool for high-quality medical imaging. Almost any part of the human body can be imaged with it, including void spaces, such as the lung. Many MR images come with a rich set of additional data, such as rates for gas transfer in the lung, or blood flow. Conventional NMR pictures the signal coming from ^{1}H nuclei, which are very abundant in all living tissue. Figure1.6 illustrates a Magnetic Resonance Image (MRI) of the entire human body, a brain image, and images of different diseased brains in comparison. All this can be achieved with ^{1}H nuclei.

The brains in the pathological MRI's of Fig.1.6 are heavily deteriorated, and the disease is very clear to see there. There are more subtle signs, at earlier stages of the diseases, which conventional MRI cannot detect. For their detection, contrast enhancement is necessary. The introduction of molecules with signal enhancing magnetic properties, contrast agents, is the mostly used approach, but this is often accompanied with toxicity or side effects of the contrast agent. For example: As gadolinium may accumulate to toxic levels, gadolinium contrast agents can only be used to a limited extent. That is also the case with radioactive isotopes, which also provide highly sensitive and specific contrast enhancement. Methods that make use of inherent molecules and their magnetic

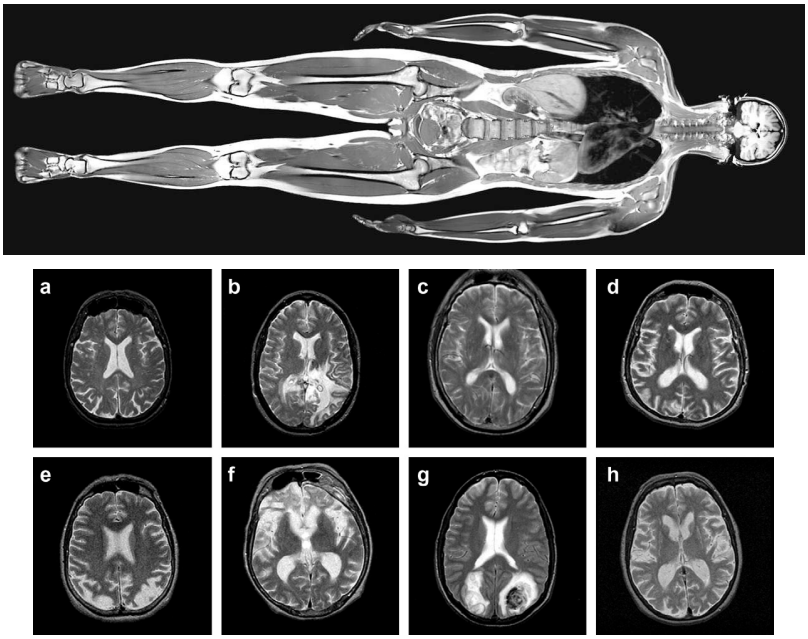

Figure 1.6: Top: Magnetic resonance image of the entire human body from J.T.Vaughan, Columbia University, Zuckerman Institute [63]. This kind of imaging can help diagnose and monitor metastatic diseases. Bottom: a) normal brain, b)glioma, c)meningoma, d)Altzheimer (AD) e) AD plus visual agnosia f) Pick's disease g) sacroma h) Huntington's disease. Figure excerpt reprinted with permission from Zhang et al [96].

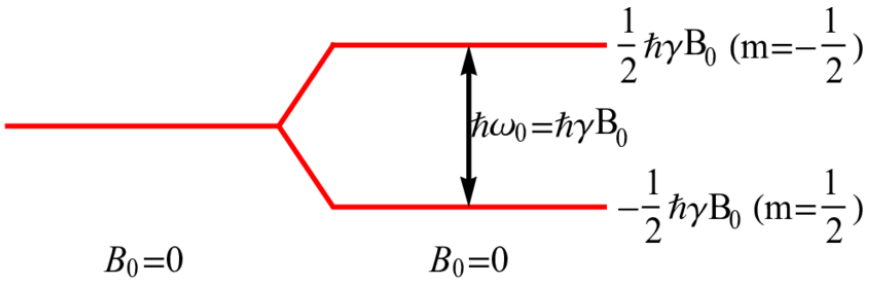

Figure 1.7: Zeeman splitting of a H nucleus, the simplest nucleus. Figure reprinted with permission from [81].

properties, like BOLD (Blood Oxygen Level Dependent) and other functional MRI techniques, and ^{1}H Chemical Exchange Saturation Transfer (CEST), can be done without a certain indication and repeated a limitless number of times. However, this is tied to the availability of the intrinsic molecules. Coupling physical contrast enhancement methods with the introduction of molecules extends the range of possibilities for detection.

NMR originates from the spin of a nucleus. Spin is an intrinsic property of a nucleus or sub-atomic particle. Spin is the "quantum of magnetic material" (I.Kuprov, Undergraduate Magnetic Resonance Lecture 01 [46]), and it determines the magnetic moment of that nucleus. The magnetic moment is directly proportional to the nuclear spin via the gyromagnetic ratio.

$$\vec{\mu} = \gamma * \vec{S}$$

The gyromagnetic ratio is the ratio of its magnetic moment to angular momentum. It is an intrinsic property of a nucleus, of which the orientation of its Larmor precession can be derived. The magnetic moment has an orientation, too, and it can be pictured as an arrow or vector pointing in a certain direction. The energy of a magnetic moment placed in a magnetic field is:

$$E = \vec{\mu} * \vec{B}$$

The different orientations of the individual magnetic moments result in different energies. Those can be seen as different energy levels. The nuclei on these levels are in different energetical states. To transition between these states, they can absorb and emit energy as electromagnetic radiation. This splitting of the energetical state into several possible states of one nucleus is called the Zeeman splitting, named after its discoverer P.Zeeman. These different levels are illustrated in Fig. 1.7.

The magnetic moment of a nucleus is determined by the distribution of nuclear spins onto the different spin states. In a spin $\frac{1}{2}$ nucleus, like ^{1}H or ^{129}Xe, the available spin states are called up

and down, and the corresponding nuclear spin quantum number m can be $+\frac{1}{2}$ (spin up) or $-\frac{1}{2}$ (spin down), as indicated in Fig 1.7. The energy of one particular state is proportional to the outer magnetic field B_0 and the gyromagnetic ratio γ. These are multiplied by m and Planck's constant $\hbar$ to quantify the energy at that state. The transition between the states is consequently termed

$$\delta_E = \hbar * \omega = \hbar * \gamma * \vec{B}$$

Frequencies best describe the form of energy, by which those energy levels can be accessed: electromagnetic radiation, delivered as radio waves. That's why, in NMR, energy is usually expressed in terms of frequency. Frequency can easily be converted back into energy by multiplication with Planck's constant. Given that only the magnetization in z direction is relevant, the contribution of the field can be reduced to its z component. The frequency for the transition between the different spin states amounts to

$$\omega = \gamma * B_z$$

This frequency required for the transition is called the on-resonant frequency for a particular nucleus in a particular situation. All other frequencies are off-resonant or offset for that nucleus. The on-resonant frequency can be changed by changing the outer magnetic field, or the gyromagnetic ratio, bearing in mind that the latter is an intrinsic property of each nucleus. The situation of the nucleus is its chemical vicinity, its location and spatial distribution. Depending on its situation, the nucleus will respond to (or resonate with) radio waves that are irradiated at different offset frequencies. The nucleus is then perturbed, and returns to its unperturbed state eventually, emitting another radio wave. This process is called relaxation.

The energy difference between the spin states is always relatively tiny, when compared to rotational and vibrational splittings, or chemical bonds. This is why one nucleus only contributes a tiny fraction to the signal. ^{1}H is the most frequently used nucleus in NMR, because it is highly abundant in most organic substances and in all tissues. So, a sufficient amount of net magnetization is only provided by all ^{1}H nuclei in a sample, summarized as a spin ensemble. From this net magnetization, a detectable signal can be obtained.

The signal from any nucleus in a magnetic field can be intensified by shortening the relaxation time, using interactions with contrast agents, which are magnetic molecules. The overall signal can be boosted by a stronger outer magnetic field. This requires even more extremely cooled, superconductive magnet coils, and even more power. Current high-field NMR spectrometers nowadays operate at field strengths over 21 T. Observing a different nucleus by using an additional set of

radio frequency coils adds new information to the NMR spectrum or image. Tracer molecules, labeled with special isotopes, like ^{13}C or ^{19}F, can be followed throughout their path. Occasionally, as for ^{13}C, their natural abundance can tell about the age of a sample.
Another way to boost the NMR signal is to work with the spin population differences. The polarization of a spin system is defined as the population excess, normalized by the total number of spins in the system.

$$P = \frac{N_+ - N_-}{N_+ + N_-}$$

As the energy gap, and thus the NMR signal, is proportional to the spin population difference, a modification of the spin population can boost the signal. The possibility of enhancement depends on how many spins can be forced to overpopulate one level, and how stable this overpopulation is. This artificial overpopulation of one level is also called spin hyperpolarization, while the naturally occurring population difference is called thermal spin polarization.

1.1.6 Xenon Hyper-CEST NMR

At first glance, xenon does not strike as an excellent probe for molecular sensing. But the ^{129}Xe isotope, is a spin $\frac{1}{2}$ system with excellent NMR properties. Due to its large and highly polarizable electron cloud, its sensitivity for its chemical neighborhood is extremely high, giving it a very large chemical shift range, and therefore, highly resolved spectra in comparison to ^{1}H. The nucleus contains numerous spins and is highly polarizable, which bears great potential for signal amplification.

Being a noble gas, xenon is practically inert. This can be used as an advantage, as undesired interactions with other molecules, accumulation or toxicity are out of the question. The inertness of xenon does not mean it does not interact with other molecules at all. It only means that, due to xenon's complete set of 8 electrons on the outer shell, chemical reactions are excluded. There are weak and transient interactions with other molecules, which can be distinguished well on the broad chemical shift range of xenon. So, without chemical reaction, xenon can report on interactions with various, even very similar, molecules.

However, as mentioned previously, xenon has a sensitivity issue: As the atom is quite rare, the net magnetization is very small. In a thermally polarized xenon nucleus, the spin population difference is so small that about nine in a million spins[74] contribute to the net magnetization. Additionally, the energy difference is much lower than in ^{1}H nuclei. That and the generally low abundance

of xenon make NMR detection of thermally polarized xenon impossible under real conditions. To make use of xenon's excellent NMR properties under real conditions, hyperpolarization is necessary.

Xenon can be hyperpolarized using different techniques. The one used here is spin exchange optical pumping (SEOP). The essentials of SEOP are neatly described for non-physicists as a three-step process in ref.[74]. In the Methods and Materials chapter, this description is featured. Hyperpolarized xenon is the result of this process. More specifically, up to 50 % of the xenon can be hyperpolarized after SEOP. SEOP is only functional and efficient for a gas mix with a low percentage of xenon. Usually 5% or 2% xenon are used, which is sufficient to generate signal.

As mentioned earlier, xenon reports on its chemical vicinity with high accuracy , interacting with it via weak interactions, like van-der-Waals forces and Coulomb forces. These interactions cause xenon to partition into lipophilic regions, like membranes, micelles, or macromolecular cavities. But as xenon interacts unambiguously with all these regions, molecular specificity needs to be generated otherwise.

In this study, a unique combination of physical contrast enhancement and chemical saturation transfer is employed: HyperCEST, which is a combination of CEST with hyperpolarization. CEST is the acronym for chemical exchange saturation transfer, a method originally developed with ^{1}H nuclei. It is a way of indirect observation of specific or unaccessible groups of nuclei. This technique originated from Amide Proton (MR) Imaging (API), which is an excellent example for the explanation of CEST: The hydrogens on Amide groups are labile, meaning that they can detach from the molecule, and be replaced by hydrogens from the bulk water around it. The hydrogens are seen as two pools, the bulk water pool and the amide bound pool. Compared to the bulk water, there are very few amide-bound hydrogens. These two pools can be separated by their chemical shift, which directly translates into a saturation frequency, which can be irradiated onto them as a radio wave, destroying their polarization (which they have, even in thermal equilibrium). With absolutely no polarization they become "invisible" in MR, and do not longer contribute to the overall MR signal. As the hydrogens exchange, every depolarized or saturated hydrogen is eventually replaced by a new, still polarized one from the other pool. Saturating the nuclei from the smaller pool of interest again and again will eventually diminish the signal from the larger bulk pool. It becomes evident that the decline in bulk signal is strongest around a center frequency. By sweeping through a set of frequencies, a spectrum is generated, which is known as the Z-Spectrum. The bulk signal reduction over the frequency has a lineshape and magnitude in this spectrum, from which further information can be deduced. The same can be done for xenon, only that xenon is not bound, like the amide protons, but in a transient interaction with another molecule. Fig.1.8

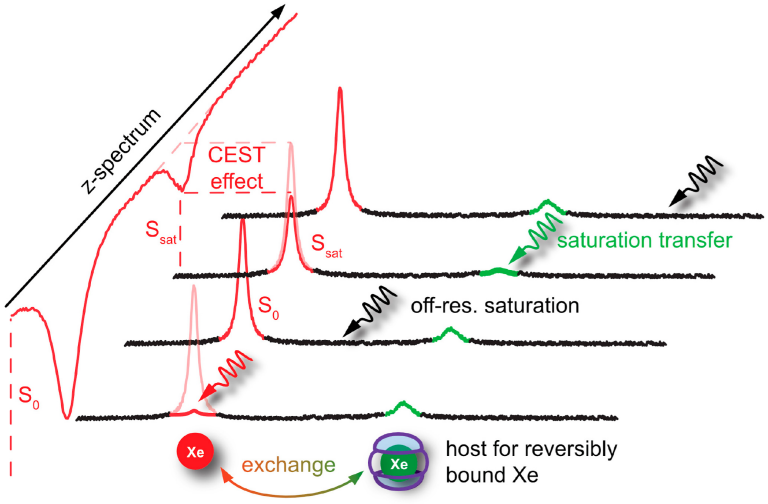

Figure 1.8: Principle of CEST detection with xenon, reprinted with permission from [37].

shows a Z spectrum and its components of xenon.

In xenon CEST, the bulk pool is the dissolved xenon in solution. The other pool can be anything that transiently interacts with xenon. To generate specificity, xenon should interact with specific molecules in a recognizable way. For that, a specific molecule that interacts with xenon and provides a defined chemical vicinity, is necessary. This molecule is called a host molecule. Xenon transiently resides there for a defined residence time, and is replaced by another xenon subsequently. Whilst residing in the host, xenon can be depolarized by a saturation radio frequency pulse, and so diminish the MR signal from the bulk xenon pool, just as during ^{1}H CEST. Targeting molecules, which specifically detect biologically relevant molecules, can then be coupled to the complex of xenon and the host molecule, reporting on this specific chemical vicinity.

Using CEST, different pools of nuclei can be labeled selectively. This can be done with all MR-active nuclei, also ^{129}Xe. For ^{129}Xe NMR, the unique combination of hyperpolarization and CEST, called HyperCEST, is the most efficient way of maximally amplifying the signal from a minimal number of ^{129}Xe nuclei. This is illustrated in Fig.1.8, and explained in ref. [37]: S_0 is the full signal from xenon in solution. Highlighted in green is the signal from xenon in the host, which in a direct spectrum, as is depicted along the horizontal axis, would probably go unnoticed. The saturation (radio frequency) pulses are indicated as arrows, and the decrease in signal and its dependence on the frequency is shown. As over time, xenon exchanges many times, an on-resonant saturation pulse

(green arrow) accumulates depolarization and diminishes the xenon signal in solution significantly to S_{sat}. The difference between S_0 and S_{sat} is the maximally pronounced CEST effect.

CEST effect can be measured in % saturation, as:

$$\frac{S_0 - S_{sat}}{S_0}$$

But that is only a momentary, frequency-specific term. In the Z spectrum, a CEST also has an individual lineshape and broadness, which originate from the exchange rate and saturation pulse strength. The integrated area under the curve was used as a very rough measure of magnitude, in order to reduce CEST to a number and compare. The maximally pronounced CEST (CESTmax) at the center frequency can also be used for this. The less the lineshape is conserved, the less accurate and reliable the CESTmax becomes as a measure of magnitude.

1.1.7 Cryptophane

The first and most studied xenon host is a molecule called cryptophane. Its original purpose was the encapsulation of small molecules.
The encapsulation of small molecules has always been a highly active research field with numerous applications and a perpetual demand for new insights. The cryptophane core depicted in infobox 1.1.1 is established as the standard molecule for xenon exchange and encapsulation.
The first cryptophane molecules were reported in 1987 by J.Gabard and A.Collet [18]. By design, cryptophanes consist of two concentrically stacked cyclotriveratylene (CTV, also often called cyclotribenzylene, CTB) units, which are linked to each other by alkyl linkers [14]. The cavity within is perfectly suited to accomodate small, non-polar molecules in a reversible manner. By modifying the linkers, the cavity can be varied in its accessibility, flexibility and size. Introducing functional groups can vary the affinity for charged or uncharged guests, as well as the solubility in water.

Box 1.1.1 Cryptophane Nomenclature

The first and most studied xenon hosts are cryptophanes: They consist of two cyclotriveratylene (CTV) caps, connected by three (usually dioxy-) alkyl linkers. Cryptophane A, depicted below, is the first cryptophane, prepared by Collet et.al.[18]. It is the host of choice in this study.

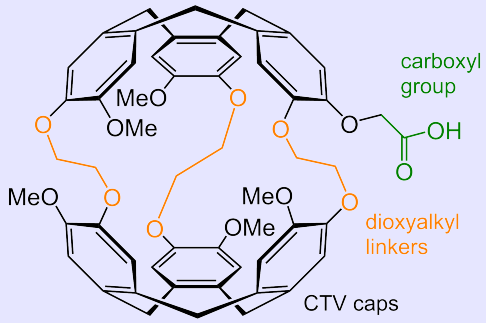

The names of cryptophane A,B,C... etc. do not reflect chronological order or structural features of the molecules. They were given in a rather arbitrary way. Therefore, a more consistent nomenclature is necessary. The **nml core nomenclature** is the most widespread and comprehensive way to specify a cryptophane. The letters **nml** refer to the number of **available carbons at the linkers**. The **nature and number of the functional groups** on the caps can be named afterwards, so that **cryptophane-A is [222](OMe)$_6$**.
Cryptophanes can also be classified based on their molecular symmetry. The orientation of the caps and the functional groups on the linkers defines a cryptophane as *syn* or *anti* diastereomer. The chiral *anti* isomer has better binding properties than the *syn* isomer.

The cryptophane A-monoacid shown here is therefore
***anti*-cryptophane[222](OMe)$_5$COOH**

The [222]cryptophanol is used for the vast majority of xenon biosensing applications. Functionalization at the only carboxyl group is possible "without encountering symmetry problems"[9]. The Cryptophane core however with its 5 remaining methoxy groups on the aromatic ring structures is hardly water soluble. This also causes the tendency to partition into hydrophobic environments, such as cell membranes, intracellular membranes, liposomes, micelles, etc., and to self-aggregate at high concentrations.
Theoretically, each cryptophane can exist in 4 different conformers in parallel, according to the

conformers of it's CTB caps: crown-crown(CC), crown-saddle(CS), crown-inverted corwn(CCi) and inverted corwn-crown(CiCi)[9]. The length of the linkers however determines the possible conformers. Cryptophanes with short linkers tend to be more rigid, whereas longer linkers give a cryptophane more conformational flexibility[9].

Box 1.1.2 Cryptophane Conformation

Cryptophanes can assume different conformers. This is mostly based on the conformation of the CTV caps, which can assume 3 conformational states: the crown (C), inverted crown (Ci) and the saddle (S) conformation.

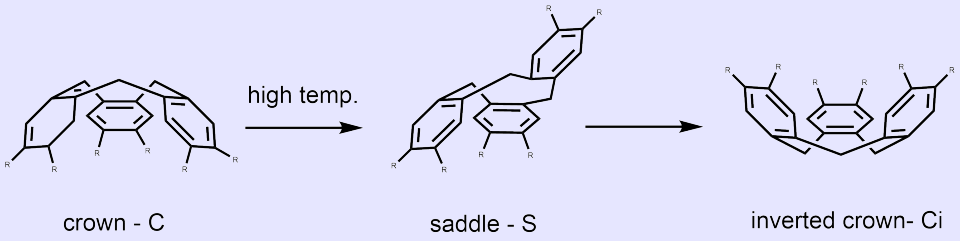

A conversion from C to S is reached by exposure to heat. This applies to CTV, as well as cryptophane, which concequently assumes a CS, aka. "imploded" conformation.
Here, the possible conformations of cryptophane are shown schematically:

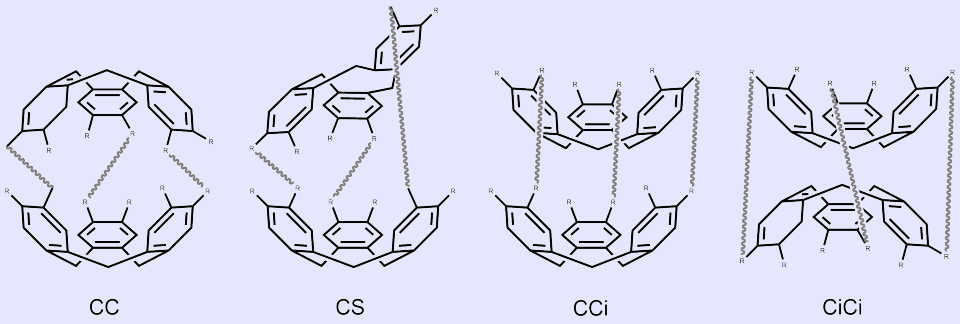

Cryptophanes have been constantly modified and improved since their invention. Nowadays, the encapsulation of a large variety of guests is possible with cryptophanes. Xenon encapsulation is particularly favorable and has a wide range of applications in NMR spectroscopy and imaging, with and without spin polarized ^{129}Xe nuclei.

The first hint for interactions of xenon with cryptophanes was the xenon - cyclodextrin interactions, first reported by Bartik and colleagues in 1995. The authors report a measurable interaction, merely entertained by van-der-Waals forces using H-NMR and Xe-NMR, in water and an organic solvent [8]. A later study of bartik and colleagues demonstrates reversible xenon-cryptophane binding as the most stable host-guest interaction with cryptophane. This study also explained reasons for this stability:

1. The spherical, monoatomic xenon and the cryptophane cavity match in size, so that the complex is neither too tight nor too lose, which makes it enthalpically stable.

2. This is due to an *induced fit* conformation, meaning that the cryptophane adjusts to fit the guest's volume and shape upon encapsulation, guided by an enthalpically favourable state it reaches thereafter [40] [83].

3. There is no or little entropy loss, because there is no rotational or vibrational entropy loss, as xenon is monoatomic and spherical, and cryptophane's conformational freedom is reduced when xenon resides in the cavity [7].

These properties paved the way for developing robust molecular biosensing applications, which rendered the pair cryptophane-xenon especially interesting for medical imaging.
A host entering cryptophane is most likely "squeezed" through the flexible gates. Entry and exit of guest molecules are regulated by a gatekeeping mechanism. Passage is only successful if the guest molecule matches the cavity in size (vdW Volume), shape (globular is best), and polarizability. The single xenon atom, to which all of the above apply, is "squeezed" through the flexible gates, after which the cavity accommodates around it. This accommodation is described in [83] as "induced fit". Because the reversible binding is rather constrictive, the exchange is comparatively slow.

1.2 Responsivity and Cryptophane Silencing

Cryptophanes were known to exchange xenon unambiguously, and so, cryptophanes were thought to be unconditionally detectable by xenon NMR. So far, any specific target detection with a cryptophane conjugate has been realized by xenon chemical shift change.
In its most simple mode, a biosensor is bound to the target, excess molecules are washed out, and the detection indicates a presence of target molecules. The detection unit can however be linked to a reporting mechanism, such as metabolization, structural rearrangement, mechanical torsion,

cleavage or another kind of activation. This reporting mechanism can be reversible. When this is the case, it is called a dynamic response, and the biosensor is dynamically responsive.

The peptide, which was originally meant to be only a binding site for CaM, turned out to be a molecule that can block the reversible binding of xenon with cryptophane, so that the HyperCEST effect cannot take place. Consequently, there is no sign of cryptophane in the Z-spectrum, which is why I prefer to call this novel effect **cryptophane CEST silencing**. On top of this highly interesting finding, cryptophane CEST silencing was found to be dynamically reversible in this study. By enabling CaM-peptide binding, for example by an elevation of the calcium concentration, cryptophane CEST silencing is remediated, and the HyperCEST effect is reactivated. This occurs simultaneously and proportionally to the rise in calcium concentration.

In Fig.1.9, the molecular interactions of the biosensor are symbolically illustrated. This provides an overview of the dynamically responsive biosensor of this study and its subsequent components. The way from the biologically relevant molecule to the response can be roughly outlined in the following steps:

1. A calcium wave or spike causes a rise of the intracellular calcium concentration.

2. CaM binds 4 calcium ions. This causes a kink in the central connecting helix domain, which enables CaM to wrap around its binding partner.

3. CaM and the helical peptide of the biosensor (shown in Fig. 1.9 as a rod) undergo wrap-around binding.

4. With CaM wrapped around it, the helical peptide is occupied and cannot engage in other molecular interactions. The peptide can no longer interact with cryptophane.

5. Cryptophane is no longer silenced by the peptide and exchanges xenon.

6. A HyperCEST effect is reconstituted and can be measured.

In the following chapter, "State of the Art", several cryptophane biosensors are described, but most of them are not dynamically responsive. The dynamic response of this biosensor is indeed a novelty, especially considering the concentration regime in which it is effective. The phenomenon of cryptophane CEST silencing is initially characterized in this study, hopefully encouraging further research towards defining a chemical mechanism.

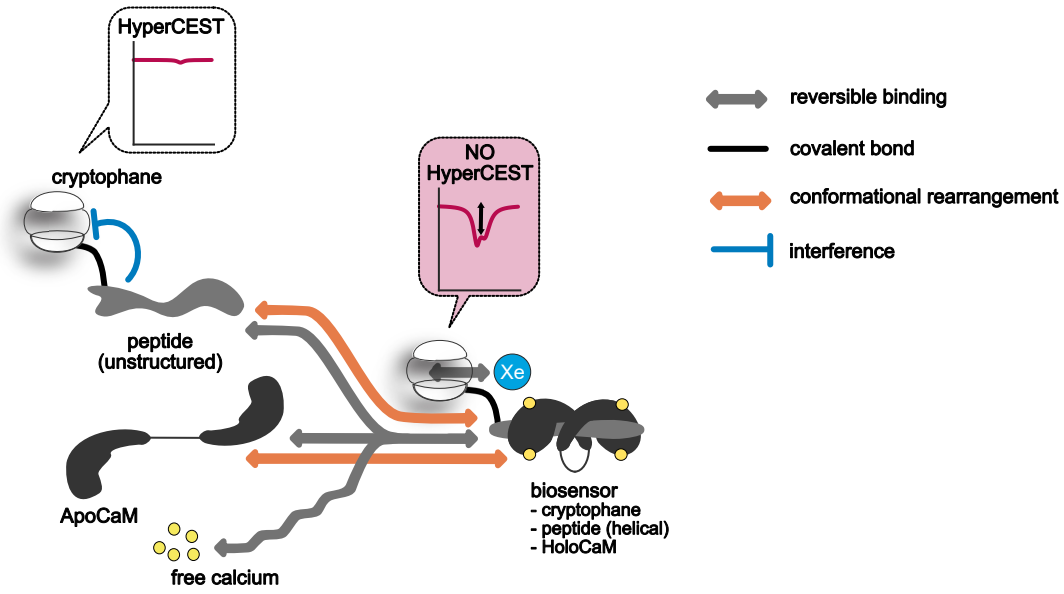

Figure 1.9: The molecular interactions of this biosensor.

1.3 Key Questions

This thesis contributes to the description of the new chemical function of cryptophane molecules, the dynamic calcium ion concentration dependent crytophane CEST silencing, monitored with a novel biosensor for Xenon HyperCEST. The key questions of this thesis can be summarized as follows:

1. Is tissue wide, highly sensitive, and fast responsive imaging of intracellular calcium possible with MR?

2. Can one build a biosensor similar to GCamP for NMR, and what does it contribute in the field?

3. What is behind cryptophane silencing, and is there a chemical mechanism behind it?

Nuclear magnetic resonance (NMR) is a great tool for research on intracellular calcium signalling in the live and unpreturbed human brain. The beauty of NMR in medicine lies within the combination of practically limitless signal depth and the complete medical noninvasiveness. This renders the entire human body (NMR-) transparent, whilst observations can be repeated as often as the specimen or patient can hold still. But NMR has sensitivity limitations, which need to be overcome in order to measure targets with low concentrations, like intracellular calcium. To overcome

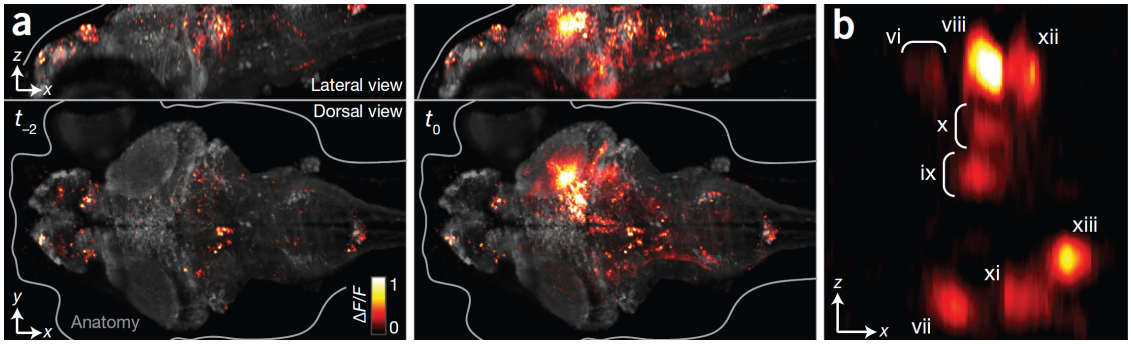

Figure 1.10: Whole live brain image of a juvenile zebrafish, excerpt reprinted with permission from Ahrenas et al.[2]. The image was generated with light sheet microscopy, and calcium was indicated using transgenic GCaMP5 fish. A time - resolved calcium recording analogous to this image is publicly available was well (https://www.youtube.com/watch?v=lppAwkek6DI).

these sensitivity limitations, contrast enhancement techniques are perpetually being improved and invented. The technique used in this study, xenon HyperCEST, bears no exception. Once fully understood, the newly discovered cryptophane silencing can be useful to further develop xenon HyperCEST.

The research around NMR of hyperpolarized xenon has always pursued more sensitive and specific targeting in NMR. The conventional ^{1}H MRI is nowadays the basic platform of a diagnostic process, on which methods of contrast enhancement and targeting stand.

Numerous fluorescence microscopy studies unraveled the pivotal role of intracellular calcium signaling on the state and fate of a tissue in samples as large as a zebrafish brain. The most impressive example, shown in Fig.1.10 shows brain activity purely by calcium fluctuations as a publicly available video clip, originally published in ref[2]. But the hard limits of light sheet microscopy restrict whole-brain *in vivo* calcium imaging to the size and transparency of a juvenile zebrafish. Anything larger or less transparent is only accessible with NMR.

The example for the novel MR biosensor are the GCaMP (which is an acronym for Green fluorescent Protein-CaM-Peptide) proteins, a family of genetically encoded biosensors for intracellular calcium, described in ref.[3]. The biosensors that were studied here have been designed after the example of GCaMP proteins. However, it has shown that a complex and large molecule like GCaMP is not necessary for the most intriguing feature of the biosensor: Cryptophane silencing. A simpler and fully synthetic calcium sensitive molecular architecture is probably best for further research and development.

Throughout this thesis, it will become evident that the endeavor to create an NMR biosensor

for intracellular calcium is quite feasible. However, the development towards MRI of intracellular calcium poses major challenges, most of all in temporal resolution. Additionally, although cellular resolution is also feasible, imaging in volumes as large as the human brain is probably accompanied by challenges with xenon distribution, biosensor distribution, and NMR-specific scale-up challenges, to say the least.

This thesis comes to the conclusion that cryptophane silencing needs to be fully understood to be applied and developed. This is essential for any application or further research along this path. Initial findings provided here may help guide the research to be more efficient in the future.

1.4 Responsive MR Biosensors for Ca^{2+} Detection

1.4.1 Responsive Magnetic Resonance Contrast Agents for Calcium Detection

MR detection of dynamic changes in intracellular calcium concentration is a much pursued scientific goal, which has been approached in many different ways.

^{13}C compounds:

Without hyperpolarization, ^{13}C compounds already serve as valid MR reporters for calcium. Using other nuclei than ^{1}H reduces background effects significantly. Hyperpolarization additionally amplifies the NMR signal. Figure 1.11 shows ^{13}C – EGTA, a contrast agent for the detection of divalent ions, specifically calcium. Its NMR signal shifts characteristically, depending on which divalent ion is chelated. Figure 1.11 also shows the spectrum for calcium in red. With ^{13}C – EGTA hyperpolarized by DNP, as little as 40 µM calcium was detected in an aqueous sample [59]. A sample in human serum posed no additional difficulties for this detection method [59]. The limited lifetime of the hyperpolarized EGTA molecule *in vivo* however is a disadvantage of this calcium detection method.

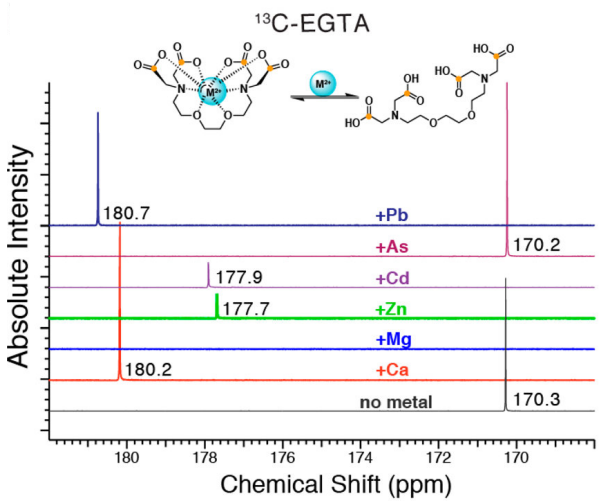

Figure 1.11: An example for a ^{13}C based responsive contrast agent, specific for divalent ions. Its structural rearrangement upon M^{2+} chelation, that causes the contrast enhancement, is shown here. The Ca^{2+} - bound sensor is inidcated in red, and below, in black, is the ^{13}C MR spectrum of the sensor with no metal bound. Figure reprinted with permission from Mishra et al.[59].

Super-Paramagnetic Iron Oxide Nanoparticles - SPION:

Caclium specific detection with SPIONs is described by Atanasijevic et.al.[4] and Xu et.al.[93], images reproduced with permission. The two SPIONs are depicted schematically in Fig.1.12, along with their MRI contrast performance. Nanoparticles with paramagnetic iron cores influence the relaxivity of nearby protons, and thereby enhance MR contrast. Decorated with two compatible moieties that connect in dependence of calcium, these SPIONs can form large aggregates and thereby achieve contrast enhancement via T_2 decrease. The nanoparticles decorated with calmodulin and the calmodulin binding peptide M13, as shown in the top part of Fig. 1.12 and described in[4], were able to report changes in the calcium concentration near 1 µM, using particle concentrations in the nanomolar range. EGTA decorated SPIONs, shown in the bottom part of Fig. 1.12, which chelate calcium and thereby aggregate, are described in[93]. In their study, the authors report concentration changes in the range of 100 µM calcium as detectable. Both[4] and[93] show, that SPIONs at super low concentrations can be used for calcium dependent imaging. SPIONs are rather large, too large for a convenient administration into cells. Once in the cell, interactions with intracellular proteins and endosomes pose further challenges to this sensor type. The calcium dependent aggregation observed in[4] takes about 1 hour to reach equilibrium. It was not mentioned in[93], how long the aggregation of the EGTA SPIONs takes. According to both studies,

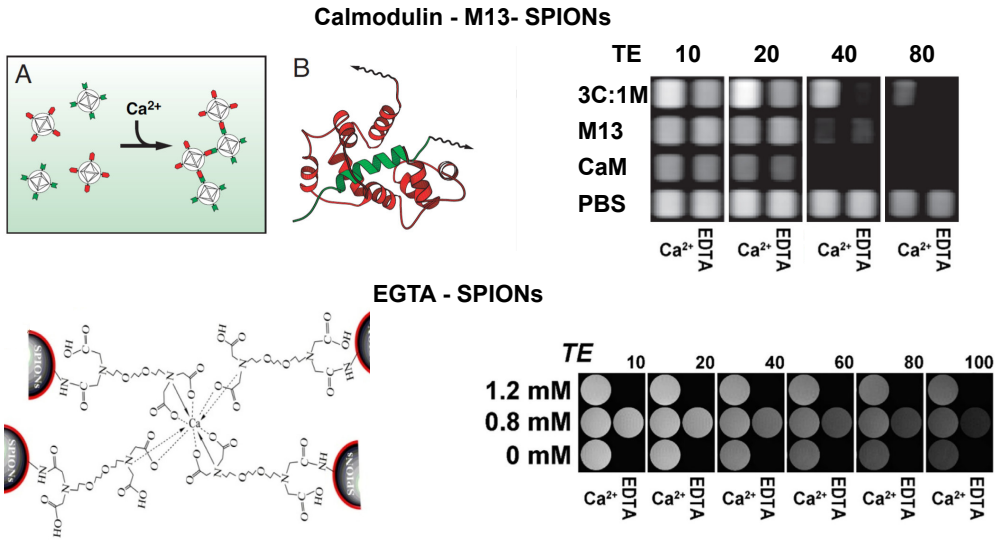

Figure 1.12: SPIONs decorated with Calmodulin/M13 ([4],top) and EGTA ([93], bottom). The aggregation is shown schematically on the left side. The right side depicts the MRI performance: In the top row of the top set, the contrast between calcium depletion (EDTA) and saturation (Ca^{2+}) becomes increasingly visible with increasing echo time (TE). The middle row of the bottom set shows the same tendency. This figure is adapted from Atanasijevic et.al.[4] and Xu et.al.[93] and the images were reused with permission.

there are potentially a few types of calcium transients that could theoretically be observed *in vivo* using SPIONs.

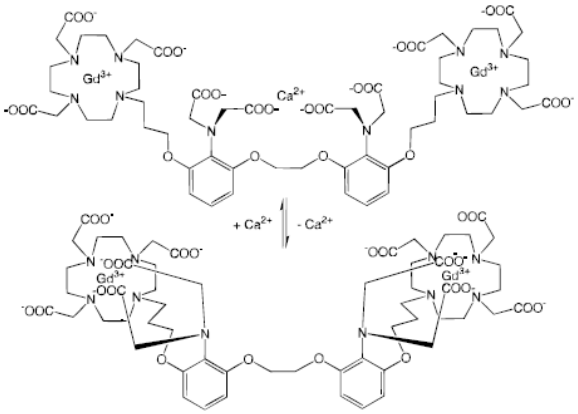

Figure 1.13: An example for a calcium responsive contrast agent based on lanthanide complexes is Gd^{3+}DOPTA. Its structural rearrangement upon Ca^{2+} chelation, that causes the contrast enhancement is shown here. Figure was adapted from Li et.al.[51], images from the publication were used with permission.

Macrocyclic complexes with lanthanides, such as Gd^{3+}DOPTA, shown in Fig.1.13, have been developed for decades, and are thus quite advanced.

But the core principle of macrocyclic complexes with lanthanides still is the same as with the earliest of these compounds. Contrast enhancement is based on the chelated paramagnetic lanthanide ion and its accessibility to water (protons). This can be coupled to a targeting mechanism, which, in the case of calcium, is chelation. Gadolinium DOPTA is an early macrocyclic lanthanide complex for calcium detection that consists of two macrocyclic gadolinium chelators, connected by the calcium chelating molecule BAPTA. Upon calcium chelation, BAPTA conformationally rearranges to bind calcium, which is depicted schematically in Fig.1.13, and allows the chelated Gd^{3+} to bind water directly, thereby accelerating the T_1 of its protons, which ultimately leads to a calcium dependent contrast enhancement. A dissociation constant of $K_D = 0.69$ µM was determined by measuring the relaxivity in dependence of the calcium concentration. The most pronounced change in relaxivity was observed between 0.1 and 10 µM of free calcium ions[51]. To form contrast agents that have superior diffusion properties in brain tissue, lanthanide chelating macrocycles were organized as large dendrimers[29]. But there are also disadvantages: As other lanthanides, gadolinium is toxic. Chelation reduces the toxicity, but there is still the possibility of gadolinium accumulation after decomposition/decay of the contrast agent. Admittedly, reducing the necessary amount of contrast agent lowers the risk of intoxication as well. However, generally, proton based contrast enhancement requires a high proton density and accessibility and may suffer from immense background effects, especially *in vivo*, depending on which type of tissue or organ is imaged.

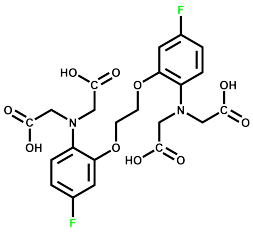

(a) ^{19}F–BAPTA, the earliest and most simple ^{19}F contrast agent.

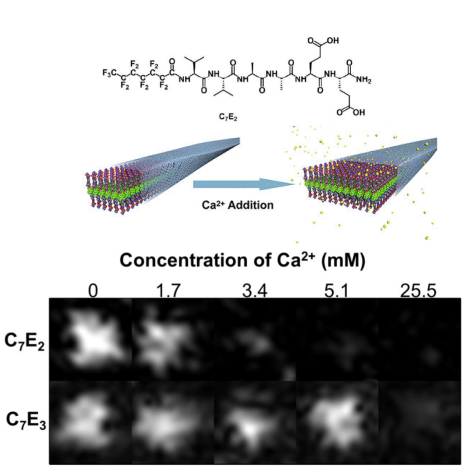

(b) C_7E_2, an amphiphilic oligopeptide (structure shown on top) exhibiting an MR contrast modulating aggregation pattern (middle) influenced by calcium. The calcium dependent MR contrast is shown on the bottom. Images reused with permission.

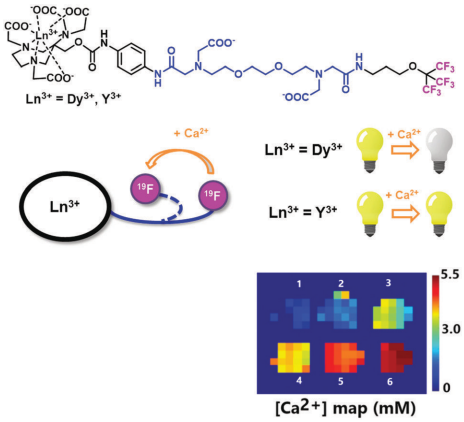

(c) Ratiometric probe $\mathbf{Ln^{3+}L}$ (structure shown on top) that combines the use of ^{19}F and chelated lanthanide ions, using their synergy (shown in the middle) to generate a more sensitive calcium dependent MR contrast (shown on the bottom). Images reused with permission from Gambino et al [28].

Figure 1.14: A few examples for ^{19}F MR contrast agents that detect calcium.

^{19}F compounds:

Very simple and highly complex ^{19}F-conjugated compounds are available to match a broad range of applications. A few examples of contrast agents with ^{19}F are shown in Fig.1.14. There is technically no background with ^{19}F-conjugated compounds. However, comparatively high concentrations are needed, when only relying on ^{19}F resonances for imaging. ^{19}F–BAPTA, as depicted in 1.14a, reflects calcium chelation as a characteristic spectral shift. ^{19}F–BAPTA has only achieved 10^{-5} the sensitivity of standerd MRI methods (proton MRI), according to [4]. The most recent calcium sensor with ^{19}F is a combination of a perfluorinated *tert*-butylether, a calcium chelating linker and a macrocyclic lanthanide chelator, in which the lanthanide can vary between Y^{3+} and Dy^{3+}, as described in [28]. Depending on which lanthanide is chelated, the sensor reacts differently to calcium binding, allowing a ratiometric quantification of calcium. Moreover, each paramagnetic lanthanide ion has its specific influence on the MR signal of ^{19}F through paramagnetic relaxation enhancement (PRE) and pseudocontact shifts (PCS). This ultimately causes the differential response to calcium from the two equal compounds with different lanthanide ions in the macrocyclic chelation site.

1.4.2 Host Molecules for Xenon

Molecular cavities for the encapsulation of xenon, transiently and permanently, have been discovered, designed, and even found by coincidence. They can be chemically synthesized or genetically expressed. They vary vastly in size, volume and xenon exchange capacity and velocity. Because of their hydrophobic interior, which provides a space for xenon to inhabit preferably, these molecules are known as xenon hosts. Xenon hosts that can be fused or functionalized are essential for the design of a xenon-based biosensor. One important advantage of synthetic hosts is their small size, which facilitates the infiltration of tissue and cells. A frequently used approach to guide this infiltration to a target is covalently linking a synthetic host to another molecule, which serves as transport or targeting unit. Individual alterations can usually be made quite freely on these molecules, e.g. to alter their physical and chemical properties. But there are also disadvantages: Biocompatibility as well as toxicity can be an issue. Synthetic xenon hosts are rarely enantiopure, which is hard to achieve and accompanied by a compromised yield. Covalent linking and functionalization to other molecules can be challenging during synthesis and purification, too. So far reported synthetic hosts are:

- **Cryptophanes**, the most studied synthetic xenon hosts, combine immense versatility with reliable xenon exchange. A small and robust core molecule, but also large and complex derivates have been developed, broadening the range of applications. The core molecule, which contains the cavity, can be modified and functionalized to alter the chemical and physical properties. Cryptophanes are described further in the infoboxes 1.1.1 and 1.1.2, in 1.4.5 in the introduction.

- **Lipopeptides:** Since xenon and cryptophane are rather lipophilic, lipid environments (e.g. lipid droplets and membranes) absorb them very efficiently. Cryptophane embedded in a lipid membrane combines a fast xenon exchange rate with a locally elevated xenon concentration and a large chemical shift change (up to 10ppm). An example for such a biosensor is shown in Fig.1.15 and explained as follows: Schnurr et.al.[73] have recently gained new insights on the more efficient use of CrA-functionalized lipopeptides within self-assembling nanoparticles. Small micelles have an improved xenon depolarization efficiency, compared to the previously developed liposomes[72]. The high local cryptophane concentration, and the additional high local xenon density, marks the strength of this contrast agent. Because of this and their compact size, the improved micelles surpass the previously developed liposomes and micelles. The auhors show the specific uptake of the micelles into cultured human brain microvascular

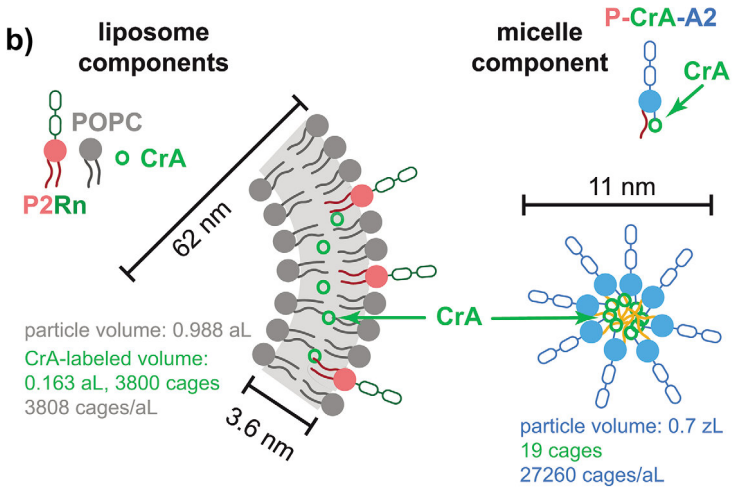

Figure 1.15: Liposomal carriers[72] (left side) and small micelles[73] (right side) are schematically illustrated for comparison. Note the cryptophane content per volume, which is given in molcules per atolitre (cages/aL) at the bottom of each scheme. The figure was used with permission from the 2020 publication by Schnurr et al.[73].

endothelial cells (HBMEC), which *in vivo* embody the blood brain barrier (BBB).

Cryptophane can partition completely into lipid environments, when the lipid fraction is over 0.1, so that the Xe@CrA concentration in the surrounding aqueous solution dwindles below the detection level. Especially when approaching more tissue-like samples or cell suspensions (which in terms of cryptophane and xenon behave similar to membrane models) with cryptophane biosensors, this partitioning needs to be taken into account[56].

- **Cucurbituriles** (furtheron called CBs) are composed of several covalently bound subunit, arranged in a torus - like ring structure. To date, there are CBs with 5-14 subunits[17,50]. Cucurbit[6]uril, a comparatively efficient in terms of xenon exchange, is shown schematically in Fig. 1.16. It is water soluble and commercially available. It exchanges xenon much faster than cryptophane, allowing faster build-up of the CEST effect. However, fast xenon exchange comes with substantial line broadening. Moreover, cucurbit[6]uril-mediated xenon exchange is significantly influenced by ions[87]. The CB core is less difficult to synthesize than the cryptophane core, yet it is much harder to graft onto other molecules, making targeting challenging[56]. CBs have also been described in detail in[43].

- **Rotaxanes**, schematically shown in Fig. 1.17 are an assembly of a cucurbituril core of choice and a competetive guest, which can regulate or completely inhibit xenon exchange by blocking the CB cavity. This competetive guest has a triazol diammonium centre, which fits

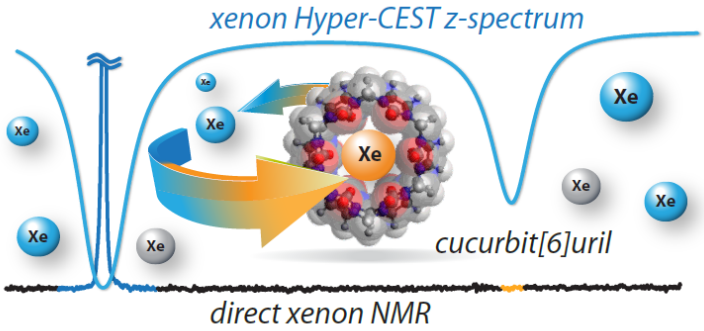

Figure 1.16: Cucurbit[6]urile, schematic representation of xeonon exchange with the molecule cucurbit[6]uril, its xenon exchange and the corresponding Z spectrum. Figure reprinted with permission from Kunth [43]

.

inside the cucurbituril ring, and two larger stopper moieties. The stoppers hinder the free exchange of this guest with the solution. A cleavable linker enables a controlled release of the guest, and thereby a controlled activation of xenon exchange. The competetive host of the rotaxane is easy to graft onto a targeting unit. However, the role of the competetive host is not exclusive to the synthetic molecule. Cadaverin and putrescin have been shown to function as competetive hosts as well, creating a hardly predictable background problem in a tissue-like situation. [25]

- **Perfluorocarbon** emulsions are essentially phospholipid-coated nandroplets filled with a perfluorocarbon. It is known since 1999 that they capture hyperpolarized xenon [91]. Klippel et. al. have shown that they exchange xenon at rates useful for HyperCEST, which resulted in the published multichannel CEST MRI [41], featured in Fig. 1.18. PFOBs are compatible with live cells and blood flow. Note that PFOB are nanoparticles, accompanied by a reduced targeting specificity and other challenges typical for their size.

Genetically encoded xenon hosts are considerably larger than most synthetic hosts. They cannot infiltrate cells as simply by passing through membranes, they are highly likely to cluster and aggregate independently. They can be recognized and destroyed by an immune system, and are often sensitive to mechanical forces. But expressed in specific cells, they can exist and be measured under the protection of those cells. Their expression can easily be induced and regulated chemically. Localization tags can be applied additionally, to guide the expression.
Published genetically encoded hosts are:

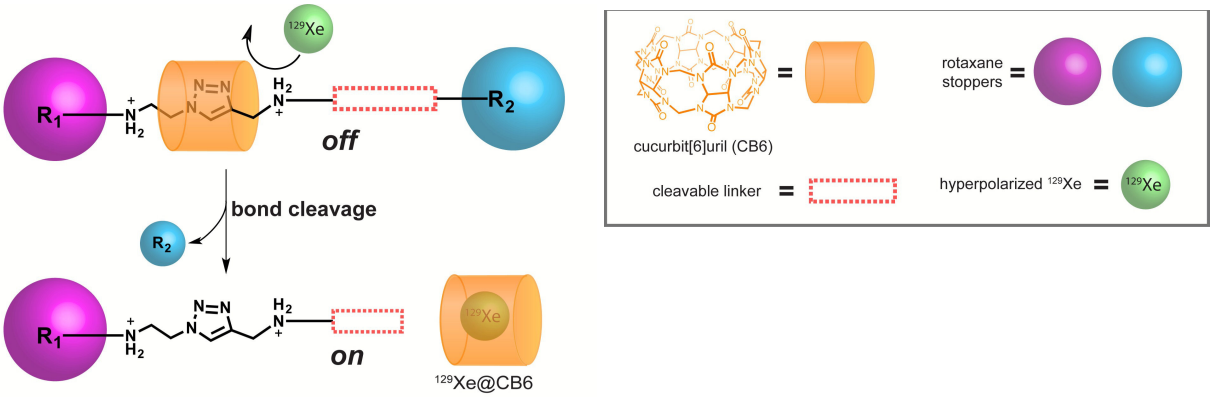

Figure 1.17: Schematic illustration of CB-based rotaxanes. The CB is blocked by the triazole until xenon exchange is "switched on" by the cleavage of the linker. Figure reprinted with permission from Finbloom et al.[25].

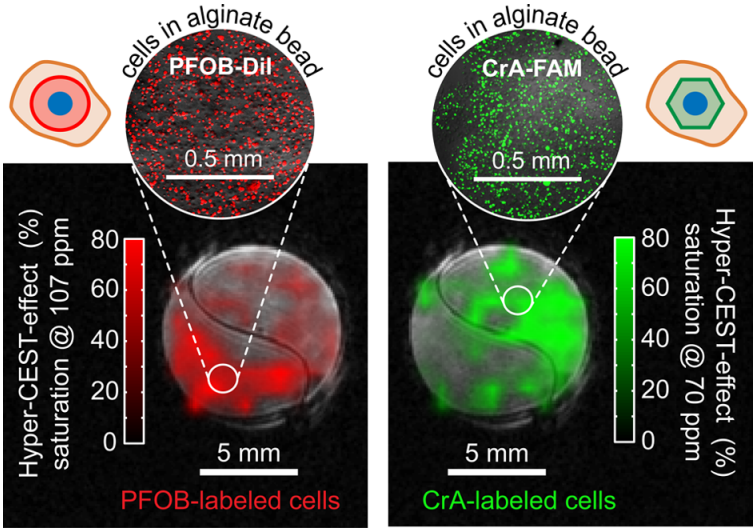

Figure 1.18: MRI of cells labelled with cryptophane (green) and PFOB (red), which exhibits a HyperCEST response sufficient for imaging and equivalent to cryptophane. Figure reprinted with permission from Klippel[41].

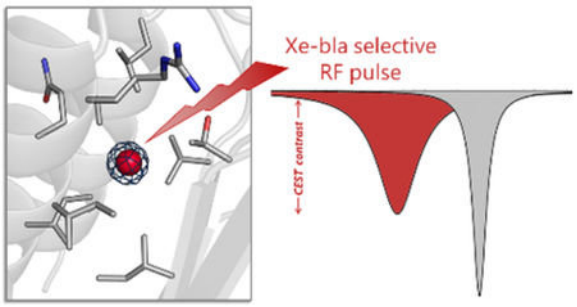

Figure 1.19: Excerpt of the structure of xenon in a pocket of the enzyme Beta - Lactamase 1, next to a schematic of the resulting Z spectrum in comparison to buffer solution. Figure reprinted with permission from Roose et al. [66].

- Cavities within a few **proteins** are able to reversibly bind xenon, as schematically outlined in Fig. 1.19. Z spectra of TEM1-β-lactamase (Bla) and maltose binding protein (MBP) show, that hyperCEST with proteins can report on structural rearrangements under native conditions [66]. As the exchange is specific for certain cavities, the literature suggests that this phenomenon could be generalized.

- **Viral capsids** self-assemble and infiltrate cells easily. Moreover, they provide a reliable way of protein coating for relatively large and versatile compartments which can encapsulate and exchange xenon. Meldrum et.al. published such a capsid labeled with cryptophane on the interior and targeting units on the exterior [57] and observed a CEST response with only 0.7 nM of it.

- **Bacterial gas vesicles** that regulate the buoyancy of water-borne bacteria harbor and exchange relatively large amounts of xenon, which makes them excellent host molecules. They are illustrated in Fig. 1.20 in a TEM micrograph, alongside with a xenon HyperCEST MR image. Their xenon exchange capacity has not been reached elsewhere so far. Full signal saturation in an image was achieved with as little as 100 pM [78], extending the detection limit of xenon hyperCEST. As fast exchanging hosts, gas vesicles cause a substantial line broadening which must be taken into account. Their relatively large volume ($4.1 - 16.5 * 10^9 A^3$ [37]) leads to a significant portion of the labelled cell being filled with gas, which influences the cell viability. Also, the vesicles are quite sensitive to pressure changes.

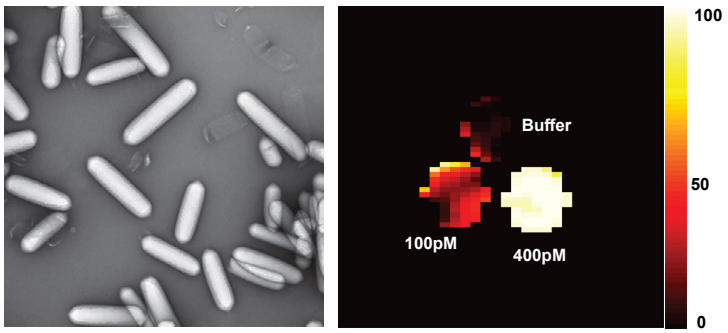

Figure 1.20: Bacterial gas vesicles, in a TEM micrograph (left) and in a xenon HyperCEST MR image (right). Figure excerpt from Shapiro et. al. reprinted with permission [78].

1.4.3 Cryptophane - From a Host Molecule to a Xenon Biosensor

Cryptophanol, which can be grafted to many different moieties via its hydroxyl group(s), marks the gateway towards cryptophane-complex biosensors. Darzac et.al. published the synthesis of cryptophanol as a building block for monofunctionalized cryptophanes in 2002 [20]. Pines and coworkers synthesized the first cryptophane-biotin biosensor, depicted in 1.21, and showed detectable binding to the target protein avidin in 2001 [80].

The sensitivity of this first cryptophane-complex biosensor was verified by chemical shift change, which was translated into an image. This was followed by a series of diverse biosensors. Xenon binding to a cryptophane sensor on avidin-coated beads was shown to be detectable in xenon MR spectroscopy and imaging by Hilty et.al. in 2006 [33]. In 2006, Weil et.al. published a cryptophane biosensor targeting the protein MMP-7(matrix metalloproteinase 7), which upon target binding, is enzymatically cleaved. The so introduced chemical modification results in a chemical shift around 0.4ppm [88], which is depicted in Fig.1.22.

In 2007, Hill et.al. showed unprecedented binding affinity of cryptophane for xenon in human blood plasma [32], using ITC and fluorescence quenching. Roy and coworkers published the first detection of nucleosides via a DNA-conjugated cryptophane biosensor, shown in Fig.1.23, in direct spectroscopy with laser polarized xenon. [69].

The structure of a cryptophane biosensor co-crystallized with the enzyme carbonic anhydrase II (CAII) has been published in 2008 by Aaron et.al. [1]. Xenon within the cryptophane cavity was co-crystallized as well and included in this structure, which is shown in Fig.1.24, on the left side. A benzenesulfonamide tether with a terminal amide on the cryptophane, shown in the middle part of Fig.1.24, interacts strongly with Zn^{2+} ions that reside in the active site of the enzyme. A specific

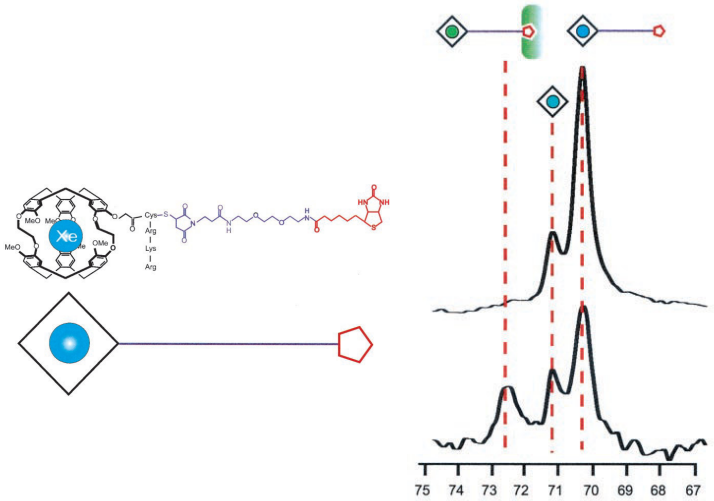

Figure 1.21: The structure of cryptophane-biotin is shown on the left side, a schematic below. Its chemical shift, depending on its surroundings, in a direct Xe NMR spectrum is shown on the right. Figure adapted from Spence et al.[80] with permission.

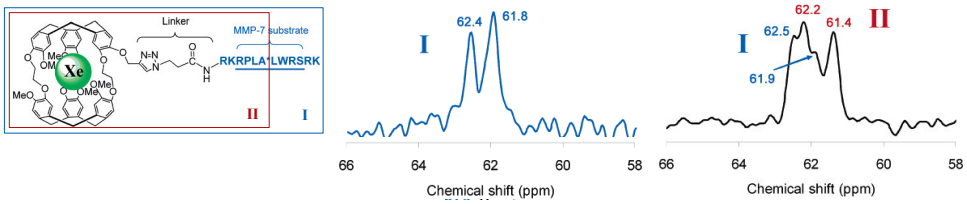

Figure 1.22: A biosensor targeted to MMP7, and the chemical shift change in the direct Xe spectrum resulting from its cleavage. Figure adapted from Wei et al.[88] with permission.

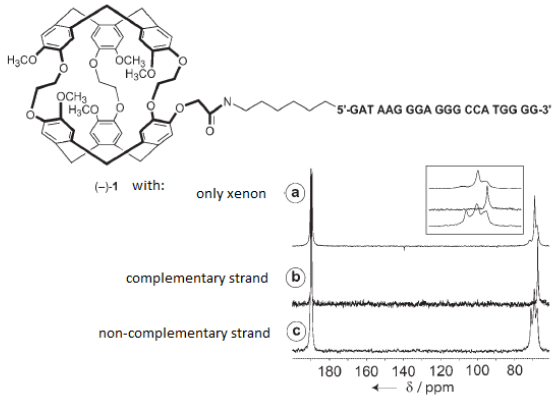

Figure 1.23: Cryptophane, covalently bound to a DNA probe, serves as a detector for complementary and non-complementary strands, as it has differentiated responses for each case. Figure adapted from Roy et al.[69], reused with permission.

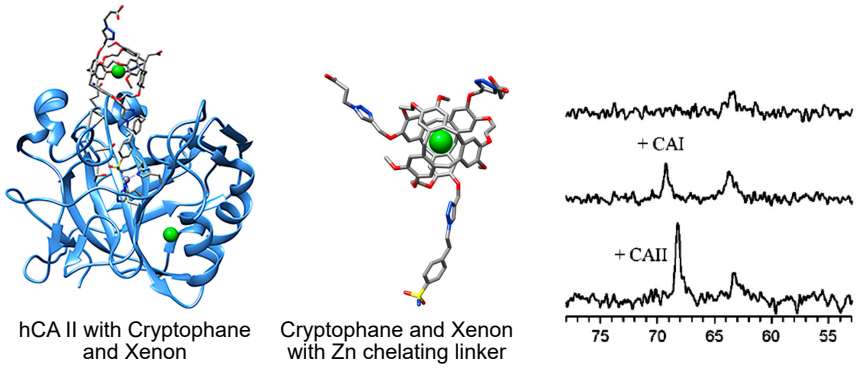

Figure 1.24: Left: PDB structure (3CYU) of human CAII co-crystallized with xenon-bearing cryptophane, Middle: xenon- bearing cryptophane with Zn^{2+} chelating tether, reprinted from Di Costanzo et al.[22] with permission. Right: chemical shift change resulting from CAI and II binding, reprinted from Chambers et al.[16] with permission.

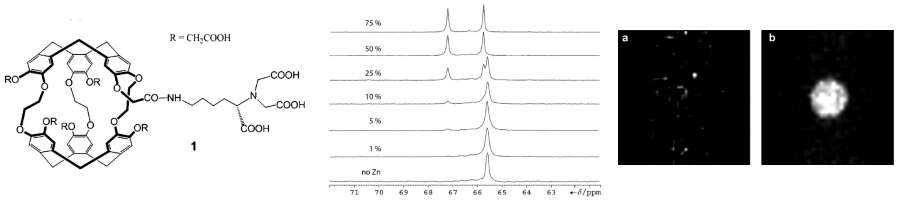

Figure 1.25: Cryptophane tethered to a chelating moiety (left) was successfully used for Zn^{2+} sensitive chemical shift imaging (middle and right). Figure adapted from Kotera et al.[42] with permission.

signal in the HP-Xe NMR spectrum was detected[16]. The signal's chemical shift is sensitive not only to whether the biosensor is bound, but also to which isoform of CA (I or II) it is bound to, as shown in the right part of Fig.1.24. At the time, this difference between bound and unbound resonance was the largest so far reported (7.5ppm).

A zinc chelating moiety was attached to cryptophane by Kotera et.al. as shown in Fig.1.25. That conferred a zinc-sensitive chemical shift change upon the cryptophane-xenon complex, which was used for chemical shift imaging as described by the authors[42].

Parallel to these developments, the complexes of cryptophane and xenon were studied in detail. Their structure, as well as encapsulation behaviour and xenon exchange dynamics are now a well studied field. As early as 1999, the structure of the cryptophane-xenon complex has been investigated. Polarization transfer between xenon and cryptophane-bound protons allows intramolecular distances to be determined, which elucidate the cryptophane conformations when xenon is

bound [54]. Brotin and colleagues revealed that xenon travels through space in the solution, rather than to be transferred by a collision of two host molecules [15]. The conformational versatility of cryptophane has been investigated by Taratula et.al. in 2010, in a detailed crystallographic study [83], revealing many aspects about the forces that drive the encapsulation of small, non-polar guest molecules. The authors reported the first crystal structure of a cryptophane without a host. They also conclude that, in terms of van der Waals forces, the CTV caps of cryptophane-A are optimal for xenon encapsulation. In an induced fit, the caps adjust around the guest molecule, reaching an energetically favorable state. However, a few barriers still remained:

1. The spectral line of xenon in the cryptophane cavity can be broadened due to motional hindrace [33], which compromises the signal/noise ratio to some extent.

2. In typical experiments with biosensors, the biosensor's concentration is very low, simply because the target molecule is usually rare. This makes the fraction of encapsulated xenon very small, and hard to detect in a direct xenon spectrum.

1.4.4 Xenon HyperCEST Sensors - A New Detection Scheme

The method of xenon hyperCEST took the detection of cryptophane-xenon complexes onto a new level, and made molecular imaging with these biosensors possible. The key to this method is making optimal use of the chemical exchange between xenon of interest (in the cryptophane cavity) and xenon everywhere else (in solution), similar to proton CEST. In 2013, Palaniappan et.al. published a cryptophane-labeled phage (shown in Fig.1.26) as a biosensor that is able to specifically track cancer cells. They were able to measure contrast in ^{129}Xe hyperCEST experiments, and confirmed binding specificity with fluorescence measurements, using flow cytometry and confocal microscopy [60].
A modular antibody-conjugated CrA-biosensor is shown in this small figure excerpt from Rose et al. [67], Fig.1.27. Cryptophane was conjugated to biotin, while the antibody was coupled to avidin. The stable biotin-avidin binding binds up to 4 cryptophane molecules to one antibody. For control measurements, one fluorescein-biotin and three cryptophane-biotin molecules were bound to each antibody, as the scheme on the left side on Fig.1.27 shows. The incorporation of 20 nM cryptophane sufficed for an adequate detection with ^{129}Xe hyperCEST. The right side of Fig.1.27 shows a xenon hyperCEST MRI with 150 nM CrA.
Khan et.al. [39] presented yet another crytophane biosensor, which was grafted to a solubilizing peptide-PEG moiety, a Cy3 moiety for the detection by fluorescence microscopy, and a folate moiety for specific targeting of folate receptor positive cells. This biosensor was shown to be internalized

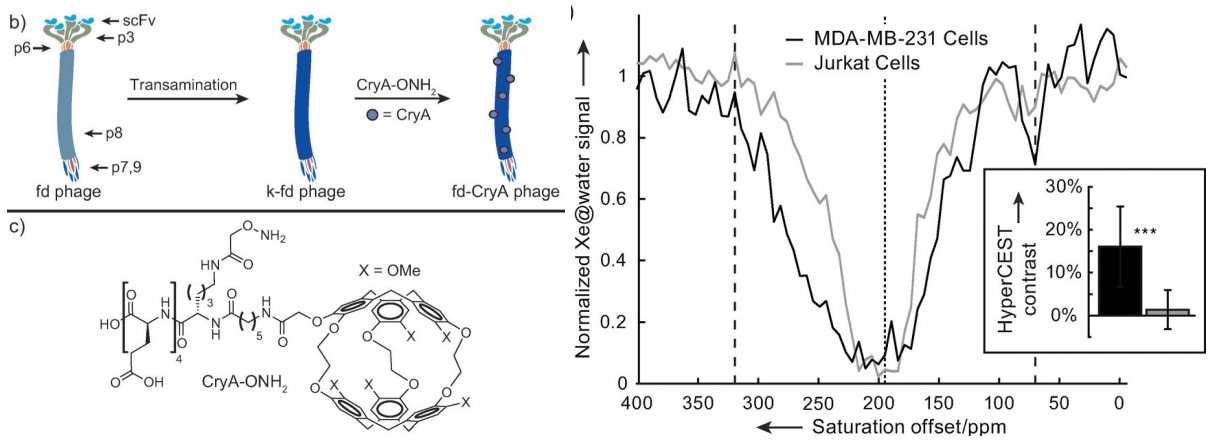

Figure 1.26: The fd-CryA phage (top left), labelled to cryptophane-A via transamination with an oligopeptide linker (bottom left). The xenon Z-spectrum on the right side shows two different cell lines that were treated with CrA-labeled phages. The Jurkat cell line (T cells) and the breast cancer cell line MDA-MB-231 have different responses when treated with the phages. The differences were quantified by the normalized Xe@water signal at a specific saturatuon pulse frequency. Figure reused with permission from Palaniappan et al. [60].

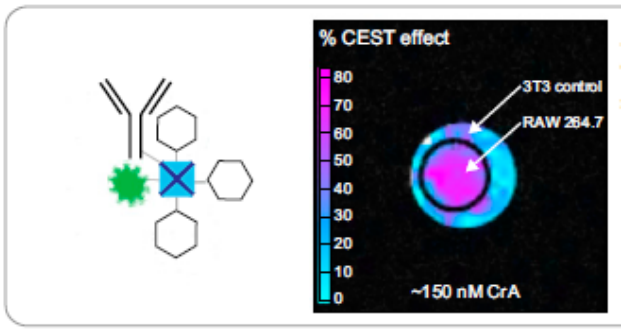

Figure 1.27: Left: Scheme of the biosensor: An antibody (Y-shaped immunoglobulin) is coupled to avidin (blue cross), which can bind up to 4 biotin units (blue triangles). Each biotin is coupled to one cryptophane (hexagon) or fluorescein (green). Here, 3 cryptophane units and one fluorescein are bound, so that the sensor can be detected by fluorescence imaging as well as by ^{129}Xe hyperCEST. Right: ^{129}Xe hyperCEST image with 150 nM of the biosensor, applied to a two-compartment phantom with antigen-positive cells in the inner compartment (RAW264.7) and cells without the compatible antigen in the outer compartment (3T3). The CEST response almost exclusively in the inner compartment, indicated in magenta, while the outer compartment in cyan indicated only a very weak CEST response.

by folate receptor positive cells. It was well detectable in direct hyperpolarized xenon spectroscopy at a concentration of 60 µM. However, a chemical shift difference between bound and free biosensor could not be confirmed. Therefore, the fraction of biosensor that was not internalized needs to be washed out, and a control assay to confirm this is detrimental for this biosensor.
All the aforementioned CrA biosensors, especially the NMR biosensors, have the potential to be sensitive and specific at once. However, in the initial steps of biosensor development, most experiments were planned in a "proof-of-concept" manner, so that there is certainly room for optimization. The true detection limits for many of these sensors may be lower than the reported concentrations. Targeting units for MR biosensors tend to be comparatively large (e.g. phages or antibodies), or lack specificity or sensitivity (e.g. SPIONs). So, either the introduction into living cells poses a challenge due to size or charge of the molecule, or the measurement of the microscopic intracellular calcium concentrations and changes is not feasible with the above mentioned sensors as they are. Further development is needed to grasp the detection of intracellular calcium with magnetic resonance. Peptides have a few very useful properties in that respect: they are small and can be synthesized with ease, they can also be incorporated into larger genetically expressible constructs. there are many peptides with the right properties to pass through cell membranes without hindrance (cell penetrating peptides, CPP), and they can function as highly specific protein or enzyme binding site. The first experiments with MR biosensors with peptides have lead to results that encourage their further development. In other fields of biosensor development, e.g. fluorescence, peptides are used successfully and frequently as targeting units.

1.4.5 Peptide-Modified Cryptophanes

Small peptides have the compelling properties of:

- a simple and straightforward synthesis
- modularity, due to freely replaceable amino acid elements
- numerous simple and straightforward options for labeling and functionalization
- the option of high targeting specificity as protein binding site or enzyme substrate

Therefore they are used in numerous biosensors[64,65,71,72,73,77]. Once linked, cryptophane-labelled peptides combine two stable, well studied molecules for targeting (peptides) and readout (cryptophane) in small, versatile sensors. The peptides used for biosensing are either substrates, binding epitopes, or reporters of structural rearrangement.

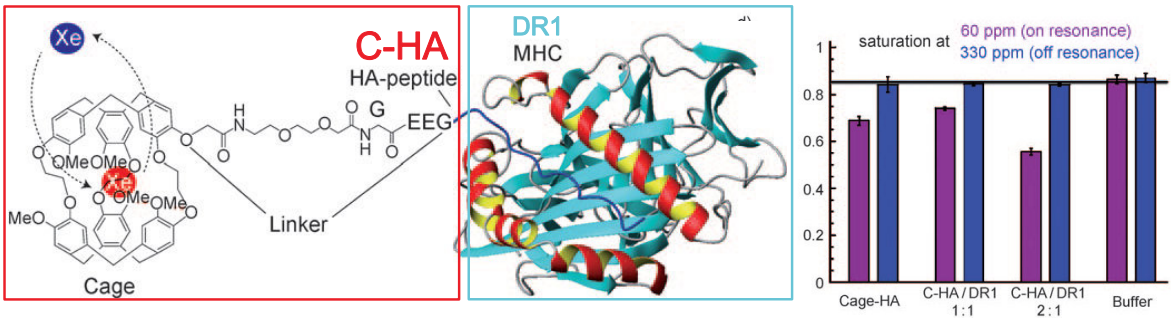

Figure 1.28: Left: Schematic view of a peptide-based biosensor's structure: C-HA (red frame) stands for cryptophane with the peptide, connected by the linker. The peptide bound to the target protein DR1 is shown in the blue frame. The right side of the figure depicts the hyperCEST effect upon target binding, which is most pronounced at a 2:1 ratio of C-HA:DR1. Figure adapted from Schlundt et al.[71], with permission.

Schlundt et.al.[71] reported the detection of a model protein for MHC2-complex binding with a cryptophane biosensor made of a small peptide chain and a terminally attached cryptophane. The biosensor and its target protein are shown schematically in Fig.1.28 on the left. In the direct ^{129}Xe spectrum, the effect of binding is a 1ppm chemical shift change. Successful hyperCEST measurements were performed with bound and free sensor compound, as shown in Fig.1.28 on the right side.

A small cyclic peptide, shown in Fig.1.29, was functionalized with cryptophane to successfully report the its specific target binding to alpha-nu-3-integrin in direct spectroscopy with hyperpolarized xenon[38].

Another modular approach was created by Witte et.al.[90], to target metabolically labelled surface glycans on live cells. Cryptophane was tethered to a peptide, which served as a scaffold, and is shown in Fig.1.30, featuring also the targeting moiety, as well as a fluorescent group for microscopical detection.

Riggle et.al. presented two "smart" CrA-biosensors, consisting of crypophane A, terminally coupled to short peptides[64,65]. One of the peptides, shown in Fig.1.31, presumably changes to an α-helical conformation at pH 5.5, while at pH 7.5, it is unordered. This change is reflected in the HyperCEST-effect.

The chemical vicinity (H^+ concentration) changes the conformational state of these peptides (from unordered to helical), and as a consequence, not only the chemical shift changes, but the xenon exchange dynamic is modulated, as shown on the right side of Fig.1.31. At certain frequencies there is a significant difference that could potentially be translated into MRI contrast. The other

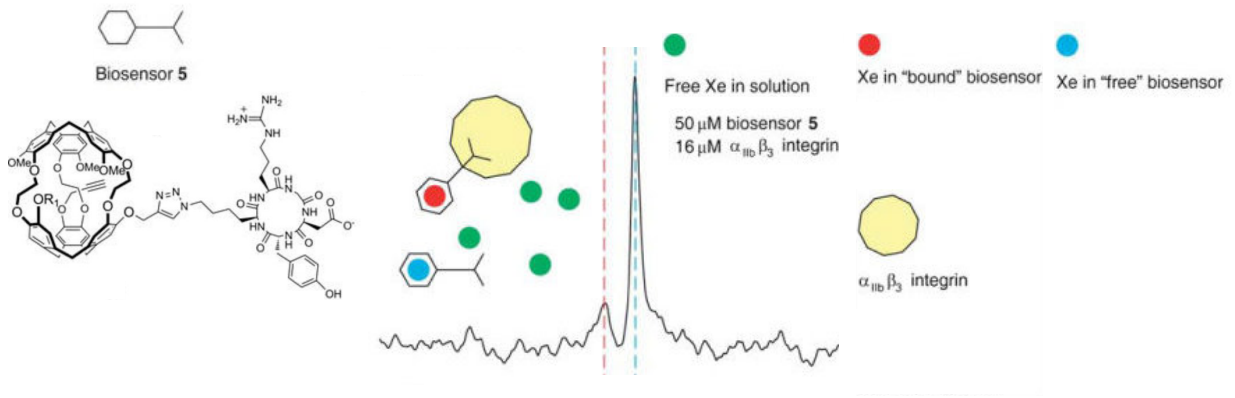

Figure 1.29: Left: Structure of the integrin - targeted cryptophane biosensor. A scheme for simplification is illustrated above the structure. Right: chemical shift change upon target binding, detected with hyperpolarized xenon. Figure is adapted from Seward et. al [38], elements from this publication have been reprinted with permission.

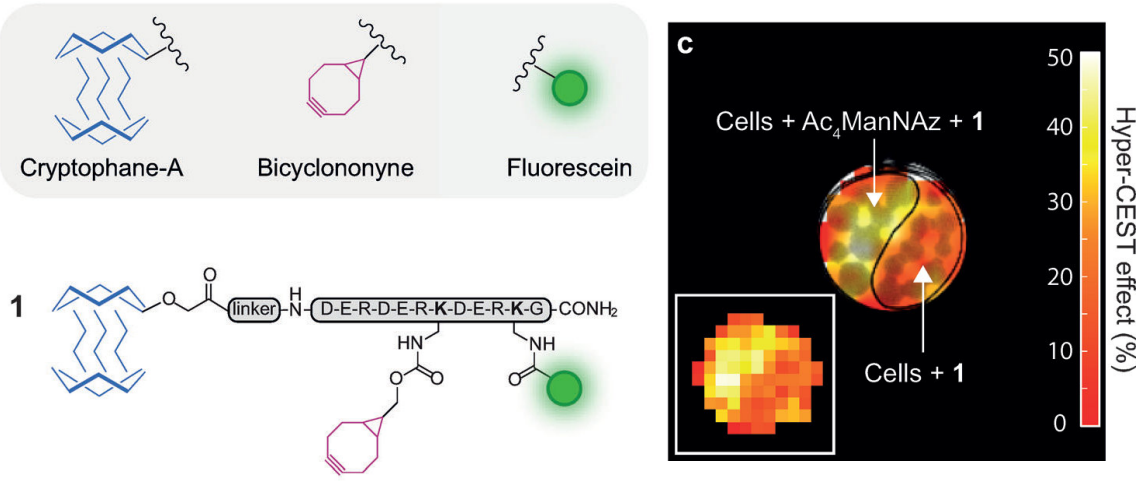

Figure 1.30: Cryptophane biosensor with peptide backbone for multiple functionalizations, schematically shown on the left. The bicyclononyne group (magenta) enables covalent binding to modified sugars, such as $Ac_4ManNAz$, via azide groups. Resulting xenon hyperCEST MRI in a two-compartment phantom on the right. Note that only cells pre-treated with $Ac_4ManNAz$ were susceptible to biosensor binding. Figure excerpts were reprinted with permission from Witte et. al [90].

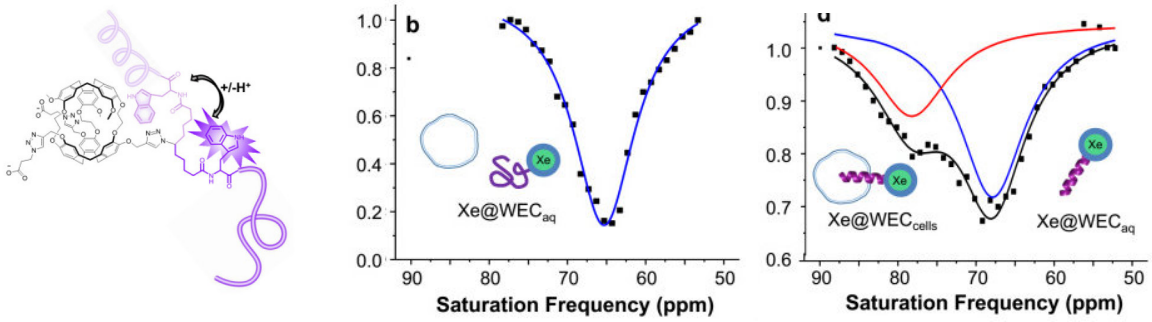

Figure 1.31: One of the "smart" xenon biosensors by Riggle et.al. [65]. The left side shows a schematic of the presumed conformational rearrangement the peptide undergoes due to pH change. The resulting pH dependent modulation of the hyperCEST effect is shown on the right side. Figure excerpts were reprinted with permission from Riggle et al. [65].

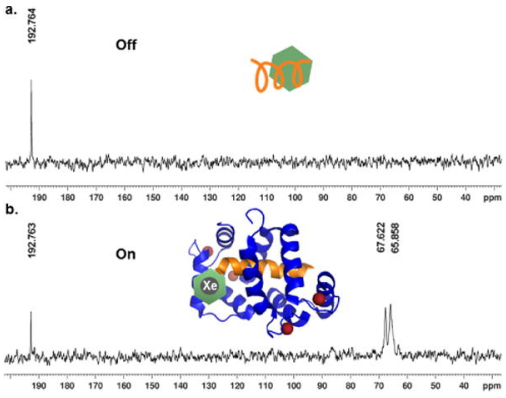

Figure 1.32: CaM-binding peptide functionalized with cryptophane in direct ^{129}Xe Spectroscopy. Top: in the absence of CaM, Bottom: in the presence of CaM. Figure reprinted with permission from Riggle et.al. [64].

one of Riggle's peptides [64] is a CaM-binding motif which silences the Xe@CrA-signal in direct spectroscopy when it's not bound to CaM. This is shown in Fig.1.32.

Peptide-cryptophane biosensors are at best responsive biosensors that can report on specific molecular events or very small changes in the chemical equilibrium (e.g. pH shift) in the cytoplasm. Generating tangible MRI contrast from these microscopic changes is the great endeavor in developing these biosensors. The current state of these developments suggests, that this is not without major challenges, but possible.

2 Aim of This Study

The objective of the project is to **develop and test a new xenon biosensor**, that fortunately has a novel function, cryptophane silencing. The Calcium-Calmodulin biosensor for Xe hyperCEST was originally designed to produce characteristic chemical shift changes for the detection of the central calcium signalling hub calmodulin. Ideally, that would make the different states of activation of this hub in dependence of the local free calcium concentration visible in MRI in very minimalistic samples. During the initial experiments, it became clear that the calmodulin - binding peptide, covalently bound to cryptophane A, has another, far more surprising effect: cryptophane silencing. There is no xenon exchange with the cryptophane cavity in aqueous samples. More notable even, the calcium dependent assembly of calmodulin and the target peptide leads to a remediation of cryptophane silencing.

This novel function is to be analyzed within the scope of this PhD project. A **dynamic and reversible response is to be shown and quantified**. Taking into account the limited accessibility of the exact reaction conditions, it is also the objective of this study to **access with alternative chemical and physical measurements what is happening in hyperCEST**, and to **confirm and expand our knowledge** of reversible cryptophane silencing. The **original design of the biosensor is to be re-evaluated** in the light of the newly gained knowledge. Furthermore, this study is in **pursuit of a mechanism causing cryptophane silencing**. In a broad perspective, this study is a **first step to defining a chemical mechanism that modulates reversible xenon binding in hemicarcerands**.

3 Results

3.1 CrA CEST Silencing and Calcium-Mediated Signal Reactivation

So far, CrA as a functional group was known to bind xenon reversibly and unambiguously. This paradigm is beginning to shift. In this chapter, a new and unprecedented way of modulating CrA-mediated xenon exchange is described.

In a sample of the CrA-labeled peptide RS20, dissolved in pure DMSO, the CrA-mediated xenon exchange is the same as by CrA monoacid. Figure 3.1 shows the CEST-effect with its chemical shift in the z spectrum at -177 ppm offset from xenon in DMSO (orange curve). In aqueous environments, the CrA-labeled peptide shows no measurable xenon exchange (light blue and light orange). Upon target recognition (peptide-CaM binding), the silenced xenon exchange and the resulting CEST effect was reconstituted (blue curve). This means:

1. Without a target, xenon exchange was inhibited.

2. The inhibition is reversed by target recognition.

This reversible inhibition is the centerpiece of this study, and this chapter contains insights for further understanding of this effect. Various facts about this CEST modulation, first indications about what mechanism might be behind it, and onto which systems it can be transferred, are collected here.

This phenomenon was further demonstrated with another calmodulin binding peptide, M13. As depicted in Fig. 3.2, both peptides were completely CEST-silent in the absence of calmodulin and responsive in its presence. The buffer provides enough free calcium in solution at all times, so that calmodulin is always at full affinity. Calmodulin/peptide ratios are 2 and 4, respectively. This amount of calmodulin triggered a CEST-effect of 40%. The same amount of unbound CrA monoacid in aqueous environment exchanges xenon faster, which is manifested in a sharper CEST-effect with 80 - 100% signal saturation, as will be shown later.

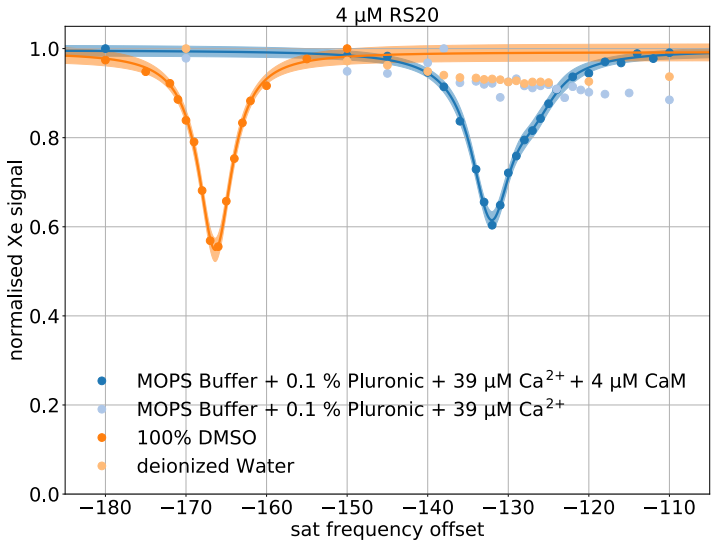

Figure 3.1: In DMSO, as shown here for CrA-RS20, the xenon exchange causes ca. 40% signal saturation around -177 ppm. In the presence of calmodulin in aqueous solution (buffer), there is a xenon exchange causing a similar level of signal saturation around -126 ppm. The large chemichal shift difference between DMSO and aqueous solution is entirely due to the solvents. This xenon exchange is not observed in aqueous solutions without calmodulin.

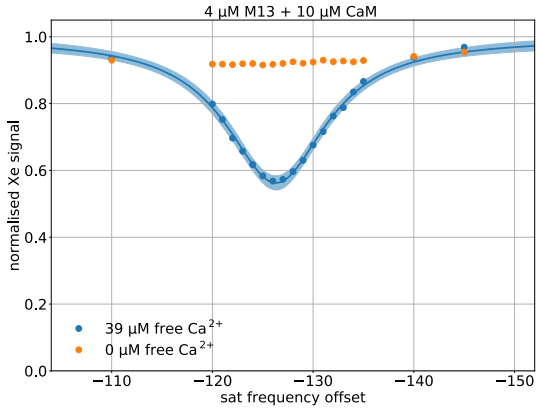

(a) M13 CrA silencing

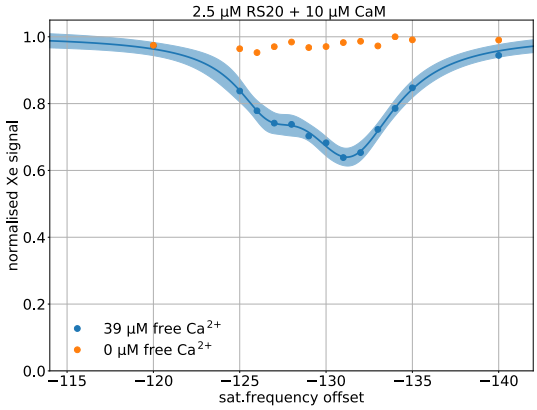

(b) RS20 CrA silencing

Figure 3.2: Z-Spectra of both CrA-functionalized peptides M13 (A) and RS20 (B). The CEST (blue curve) related to calcium mediated specific binding with calmodulin (CaM) is shown in blue, while the control measurement with CaM in a calcium depleted environment is shown in orange. M13 (A) has a CEST response centered around -128 ppm, while the response of RS20 (B) presumably has two contributions centered around -126 and -131 ppm. The responses are strictly calcium-calmodulin dependent. Each contribution was fit with an exponential lorentzian function. The fit is shown as a solid line with the corresponding error band (3 σ).

3.2 Quantification and Characterization of Cryptohane-CEST Silencing and Reactivation

3.2.1 Calmodulin Titration

Two different binding assays of CaM-peptide binding with fluorescent CrA-peptides demonstrate functioning CaM-peptide binding between the recombinant CaM expressed in this lab and the Cryptophane-fluorescein-labeled peptides: Cryptophane CEST silencing due to CaM-peptide with the peptide CrA-M13-FAM (Fig.3.3a), and a fluorescence polarization rise due to CaM-peptide binding with the peptide CrA-RS20-W-FAM (Fig.3.3a). A control experiment was analyzed with FP, to confirm that ApoCaM does not bind the peptide or lead to any measurable effect.

Titrating CaM with the CrA-peptide is highly impractical, because the measurable effects, fluorescence and CEST effect, originate from the peptide. CrA-labelled peptides are all hardly soluble in water, which is why their stock solutions are made in pure DMSO. An increase in their concentration is inseparably linked to a solvent change (addition of DMSO). Xenon solubility, CEST, and fluorescence are influenced by DMSO. It is impossible to separate the effect of DMSO addition from the effect caused by the CaM-peptide binding. Highly concentrated CaM stocks in aqueous solutions do not have that effect.
This is why an unusual declaration had to be made: the CrA-peptide was treated as receptor, and titrated with holo-CaM, which was treated as ligand, until vast excess and saturation. To be independent of calcium, calcium was supplied in excess, so that all CaM is present as holoCaM, with 4 bound calcium ions.
The CEST-effect increases with additional holo-CaM until saturation, which means that additional holo-caM does not affect the CEST effect. In the absence of CaM, there is a small CEST effect, which tells of an interaction with xenon of unclear origin, and lead to a series of further tests that will be presented later in this chapter. As the holo-CaM concentration increases, so does the CEST effect, until saturation is reached around a holo-CaM/peptide ratio of 4.

Xenon HyperCEST experiments were conducted in a much smaller CaM concentration range than FP experiments, for technical reasons, which are:

- higher protein concentrations cause a notable solution signal dampening due to excessive foaming, which cannot be controlled by antifoaming agents beyond a certain point.

- the sample volume for CEST experiments was 50x the amount needed for an FP assay. Considerably more concentrated CaM stock solution is necessary for CEST experiments in the high-CaM plateau. Up-concentrating CaM comes with the risk of unwanted protein aggregation and protein loss.

- Acquiring one Z spectrum takes a lot longer (30-45 min) than one datapoint with FP (less than 1 sec.)

With a buffered free calcium supply of 39µM, CaM is present as holo-CaM exclusively, and a first-order binding reaction between holo-CaM and the CrA-peptide-FAM, shortly named P, can be assumed:

$$\text{holo}-\text{CaM} + \text{P} \rightleftharpoons \text{holo}-\text{CaMP}$$

The few data points from this preliminary experiment were not enough to fit with a model appropriately. But the increase and saturation of the CaM-peptide based CEST-effect (Fig.3.3a) is similar to what is happening with the FP.
In the FP experiment, more titration points were attainable (Fig.3.3b). Without the need to bubble and the foaming issues, much higher CaM concentrations were measurable. Because of the detection limit of 5'FAM fluorescence is below that of the CEST effect from CrA on a peptide in aqueous solution, much lower concentrations could be measured, too. The FP measurement provides the big picture of the binding between holo-CaM and the peptide. The control experiment under calcium depletion was done with FP, and shows that the concentration of Apo-CaM is without effect on the FP, and consequently the molecular size. This is proof for no binding in the absence of free calcium.
The green areas in Fig.3.3 show the range from no occupation of peptides (which are still treated as receptors) at a holo-CaM:P ratio of 0.1, to more than full occupation at a holo-CaM:P ratio of 10. The FP Data and Xenon HyperCEST Data have the same trajectory towards saturation.
The FP data was fit to a Hill model with an offset (Fig.3.3b, grey line). The model describes a Dose-Response relationship, where the dose corresponds to the holo-CaM concentration, and the response to the measurable effect it has on the FP.

The calmodulin titration shows that the binding between holo-CaM and the peptides CrA-RS20-W-FAM and CrA-M13-FAM is not influenced by the CrA or the fluorescein at the peptides' extremities. Apo-CaM does not bind to CrA-RS20-W-FAM, and is unlikely to bind to any RS20-derived peptide

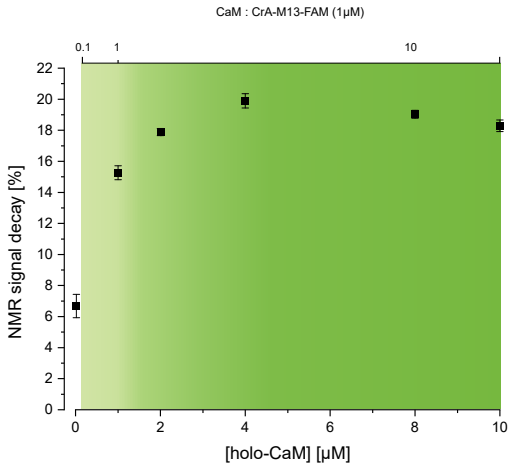

(a) Measured effect: XeHyperCEST NMR

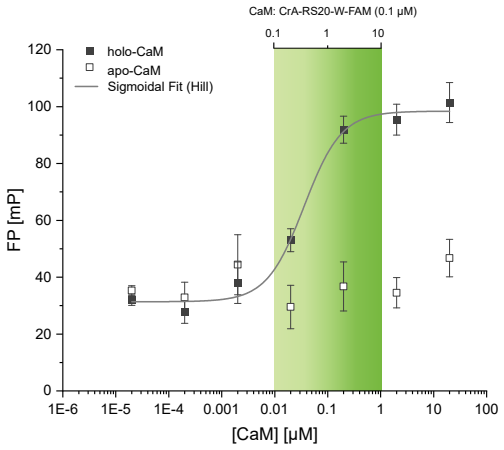

(b) Measured effect: Fluorescence Polarization (FP)

Fit function: $FP = FP_0 + \frac{(FP_{max} - FP_0)[holo\text{-}CaM]^n}{EC_{50}{}^n + [holo\text{-}CaM]^n}$

Function and fit parameters:

Parameter	Symbol	Value	Std. Error
Offset	FP_0 [mP]	31.36	1.26
Upper plateau	FP_{max} [mP]	98.405	3.63
Dose needed for half maximal response	EC_{50} [µM holo-CaM]	0.04	0.01
Hill coefficient	n	1.824	0.422
Corrected R^2	R^2	0.99	-
χ^2	-	0.61	-

Figure 3.3: Titrations of peptides CrA-M13-FAM (a) and CrA-RS20-W-FAM (b) with holo-CaM were prepared and measured in steady-state. FP was measured to complement HyperCEST NMR spectroscopy and extend the titration range, in order to capture a binding curve that can describe the entire kinetic.

under these experimental conditions. The binding can be tracked by FP and Xenon HyperCEST. FP measurements can complement Xenon HyperCEST measurements.

3.2.2 Calcium Titration

The different titration experiments (a), (b), (c) and (d) shown in Figure 3.4 share the gradually increasing CEST upon increase as the Ca^{2+} concentration increases, showing the Ca^{2+} dependence of the CEST response in every case. The CaM/peptide ratio varies slightly between the experiments. Note, that the peptide influences calcium-CaM-peptide binding substantially, inducing and undergoing conformational change and cooperating with the calcium binding sites of CaM. The Z-spectra were fit with an exponential lorentzian function in order to extract a few meaningful characteristics, in order to compare. The shape of the CEST responses varies between the experiments, as can be seen in the exponential lorentzian fit functions. Occasionally, a second contribution can be assumed from the fit, indicated by a second local minimum. This is most pronounced in titration (c)3.4c.
The development of the CEST response in the different calcium titrations appears to have similar dynamics across the experiments. To quantify this, a common measure of a CEST response is necessary. The global minimum of the lorentzian fit function, which marks the maximal signal saturation, did not suffice, as there are CEST responses with additional, calcium-responding contributions, which needed to be included. A measure that includes all newly reactivated reversible cryptophane-xenon binding in one value was necessary. This is why the exponential lorentzian function of each CEST response in each Z-spectrum was integrated, and the area under the curve was calculated. As it reflects an array of normalized xenon signals, a unit for the area under the curve (AUC) is arbitrary. The development of the CEST response was observed in a more quantitative way, using the AUC, in Fig.3.5.
The individual titrations indeed have similar dynamics. The only model that would fit the data appropriately is the offset Hill model. Titration (c) was not fit, because the data suggest linear dependence, while the dynamic is not linear. Titration (c) probably lacks data at the extreme ends, which would display the upper and lower plateau and make a sigmoidal fit possible. All other titrations were fit using the simple and widespread offset Hill model, whilst keeping in mind that this is not to determine specific kinetics with it. The offset Hill model was used to roughly quantify the relationship between CaM saturation (and implicitly, Ca^{2+} concentration) and CEST response like a pharmacological dose-response relationship. The fit statistics (χ^2 and R^2) indicate an excellent fit for (a), a mediocre fit for (b), and a sufficient fit for (d). The fit function reveals another characteristic: The sensitive range, which is the dynamic, quasi-linear part of the sigmoidal

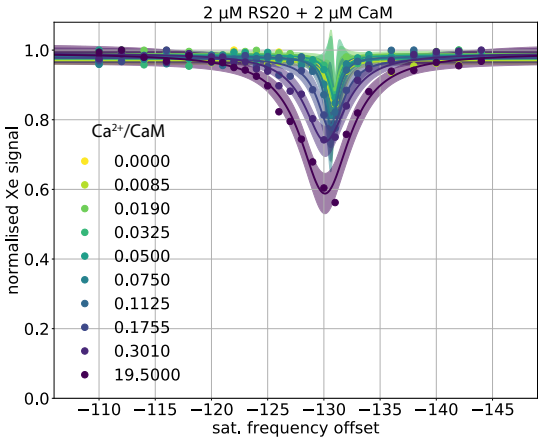

(a) peptide RS20, $B_1 = 2.58$ µT, $t_{sat} = 25$ s

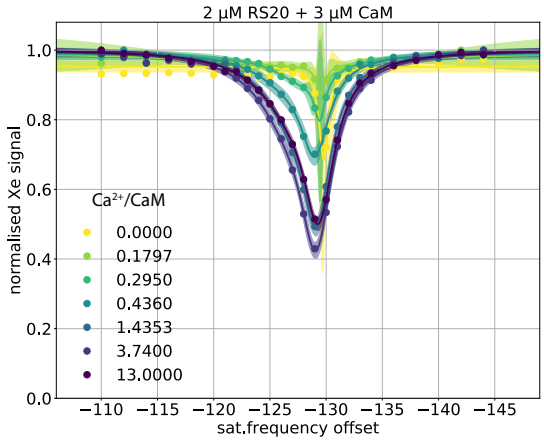

(b) peptide RS20, $B_1 = 3.53$ µT, $t_{sat} = 25$ s

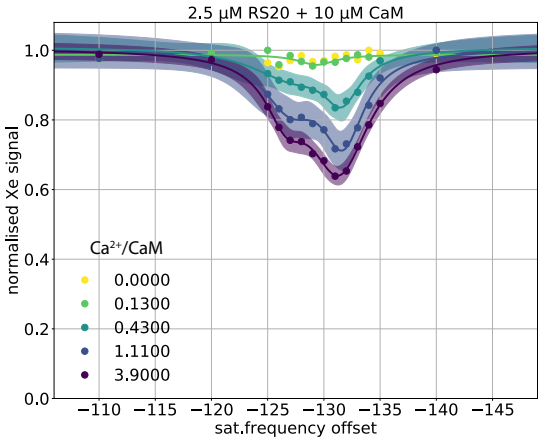

(c) peptide RS20, $B_1 = 4.07$ µT, $t_{sat} = 25$ s

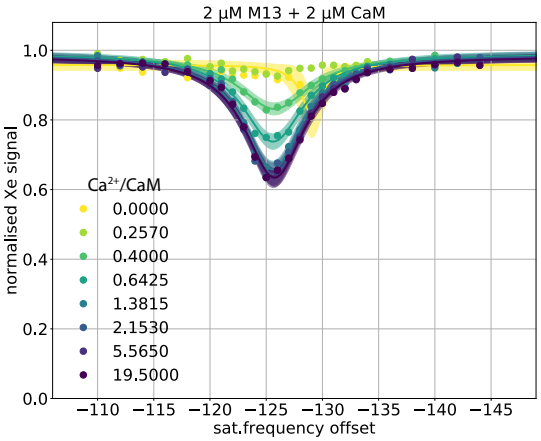

(d) peptide M13, $B_1 = 3.52$ µT, $t_{sat} = 25$ s

Figure 3.4: Calcium titrations of different CaM + peptide mixes. Z-spectra show the corresponding CEST responses, which increase with the calcium concentration, which is shown in the legend in terms of calcium/CaM ratio. The CEST responses were generated with different saturation pulses. Saturation pulse (B_1) and pulse duration (t_{sat}) are denoted below each titration. (a), (b)and (c) are responses from peptide CrA-RS20-FAM. (d) is a response from peptide CrA-M13-FAM.

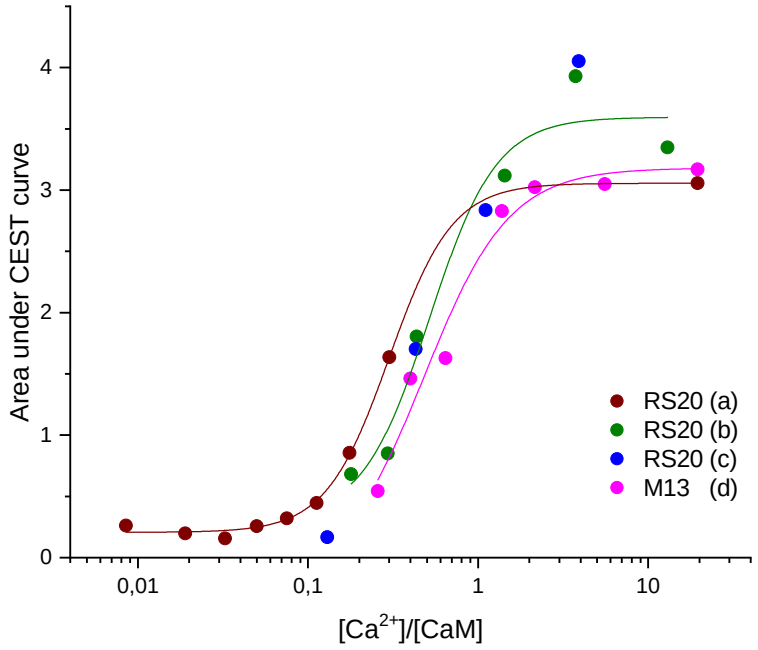

(a) Calcium titrations from 3.4, shown comparatively by the development of the CEST effect. The CEST effect is reduced to the area under the fit curve (AUC). The AUC is shown as a function of Ca^{2+}/CaM, which is an expression of CaM saturation, and shall be summarized as ratio r. The individual titrations have been fit with an offset Hill model, and the fit functions are shown as solid lines in the same color as the corresponding data. Titration (c) was impossible to fit, beause there was no data outside the linear range.

$$\text{Fit Function: } AUC = AUC_0 + \frac{(AUC_{max} - AUC_0) r^n}{{EC_{50}}^n + r^n}; r = \frac{Ca^{2+}}{CaM}$$

Function and fit parameters:

Parameter	Symbol	(a)	(b)	(d)
Offset	AUC_0	0.21 ± 0	0.31 ± 0.86	-0.21 ± 1.49
Upper plateau	AUC_{max}	3.06 ± 0	3.60 ± 0.31	3.18 ± 0.20
Half maximal CaM saturation	EC_{50}	0.30 ± 0	0.52 ± 0.18	0.48 ± 0.27
Hill coefficient	n	2.33 ± 0	2.21 ± 1.60	1.74 ± 0.93
R^2	R^2	1.0000	0.9683	0.97286
χ^2	χ^2	0.0000	0.14877	0.05728

Figure 3.5: Multiple calcium titrations and individual fits with the offset Hill model. Fit functions and parameters describe the fit ans its adequacy.

transition from zero to saturation. It can be approximated with the EC_{50}, which marks the center of the sensitive range. EC_{50} equals the ratio r, and consequently the calcium concentration, at which 50% of the maximal response is reached. For titration (a), $EC_{50} = 0.3$. So, to generate a dynamic CEST response with 2 µM of the peptide CrA-RS20-FAM and 2 µM CaM, around 0.6 µM free calcium are required. The sensitive range for CrA-M13-FAM is around 0.6 µM free calcium. The titrations (b) and (c) show that, when more CaM (b) or more CaM and more peptide (c) is present, more calcium is required to reach the sensitive range. The difference between titrations (a) and (b) is more substantial than between (b) and (c).

3.2.3 Reversibility and Range

The interaction of CaM and its peptide binding partners is a dynamic equilibrium of perpetual binding and dissociation, mostly leading to conformational changes, which temporarily modulate the activity of the target protein. The regulatory nature of these bindings demands reversibility, in order to flexibly respond quickly to new signals. Fortunately, the CEST effect is reversible as well. This is shown in two ways: During the titration with free Ca^{2+}, every sample was partly substituted in order to shift the buffer equilibrium, resulting in changes in free Ca^{2+} in solution, while everything else was kept constant. This can be done in both directions (Ca^{2+} increase and decrease), and affects the CaM-peptide binding accordingly. As this can be observed in the resulting CEST effect, the latter must be reversible. The CEST increases and decreases flexibly with the Ca^{2+} concentration, as is documented in Fig.3.6.

During the titration the sample is partly substituted, so that, strictly speaking, no internal calcium release in the exact same sample was triggered. Moreover, there is no information about the influence of an unspecific background. To account for these gaps, a cytosolic protein cocktail from HEK293 cells was used as background, and CrA-CEST silencing and its remediation with a CEST response (Fig.3.7a and 3.7b), as well as the reversibility and calcium dependence of the response (Fig.3.7c) were demonstrated in this cytosolic protein cocktail. The sample was supplemented with a volumetrically irrelevant (under 1%) amount of highly concentrated $CaCl_2$ solution, followed by an even more concentrated EGTA solution of equally small volume. The CEST increase after CaM addition was clearly visible against the background. Upon calcium chelation by EGTA, shown in Fig.3.7c) the effect went back exactly to the background level, suggesting that roughly the same amount of peptide is released from CaM and the attached, temporarily active CrA is silenced again, because calcium is missing. This shows that the CrA CEST silencing of the peptides CrA-RS20-FAM and CrA-M13-FAM is not only specific, but somewhat background resistant, and dynamically

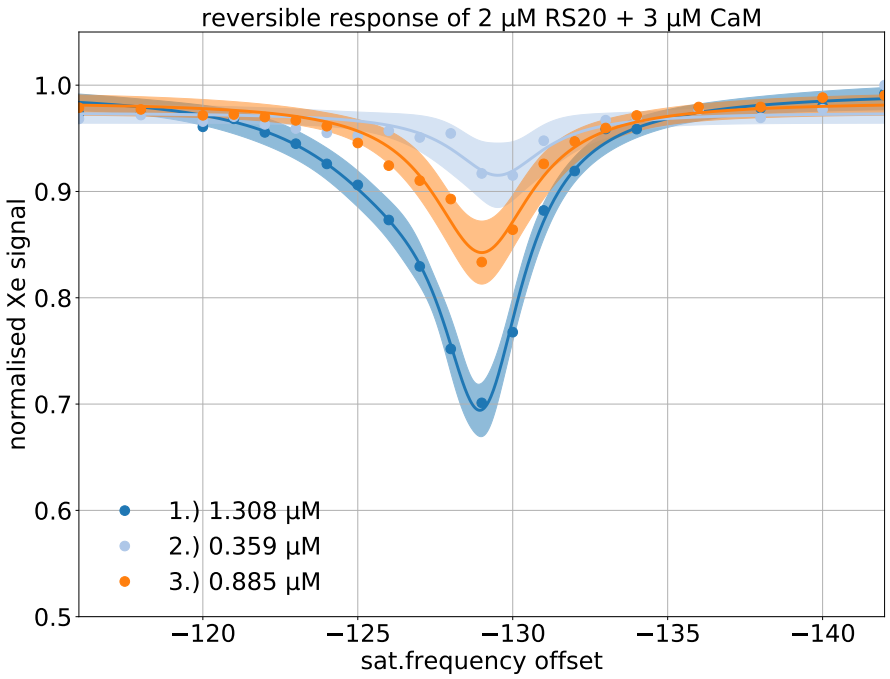

Figure 3.6: This is a small part of a Ca^{2+} titration. Here, after having been decreased (blue to light blue), the free Ca^{2+} concentration was increased. Promptly and consequently, the CEST increased as well (light blue to orange).

reversible.

3.2.4 Saturation Conditions

For the CEST response to be analyzed optimally, the saturation pulse needs to match the xenon exchange, which depends on the xenon host, the temperature and the solvent in the sample.

The strength and duration of the saturation pulse provide a frame for this: The sat pulse strength is tuned to the concentration of Xenon@host, to effectively depolarize all Xenon within host cavities within the saturation pulse duration time. Figure 3.8a shows, that equally long saturation pulses (25s) with a pulse strength B_1 of 0.204 µT, 0.409 µT and 1.155 µT generate CEST responses with ascending intensity. Stronger saturation pulses increase, but also broaden the CEST response. When the full saturation potential is reached, and all Xe@CrA is depolarized within a saturation pulse, further intensifying the pulse will only broaden the CESR response. This effect is pronounced in Fig.3.8b. This broadening still increases the AUC, but reduces the resolution of the individual contributions (peaks). A relatively weak pulse over a long period of time, such as 1.291 µT over 35 s (Fig. 3.8b), will yield a better resolved CEST response, in which individual contributions are better recognized. A stronger pulse of 4.621 µT over a shorter period of time, 25 s, will yield a broader CEST response of the same intensity, which has the larger AUC. Depending on which question shall be answered, the saturation pulse can and should be adjusted to fit the experimental objective. A compromise between resolution and acquisition time needs to be made when acquiring this CEST response in a Z-spectrum. To acquire a reliable Z-spectrum, at least 20 acquisitions are needed, including the baseline and solution signal. With a 25s saturation pulse, this takes 15-20 min at least. Using a 35s saturation pulse instead would extend this by 1:40 mins. But the longer the saturation pulse is applied, the more time there is for T_1 relaxation. T_1 relaxation reduces the Xenon@solution signal, which also reduces the signal saturation. Figure 3.8c and 3.8d illustrate this: in 3.8c, the raw xenon signal is depicted, whilst in 3.8d, the normalized xenon signal (which will appear in the Z-spectrum) is depicted. The saturation at -132 ppm is compared to the off-resonant baseline level at -200 ppm in 3.8c and 3.8d. A saturation pulse of 25s still significantly increases signal saturation, compared to 20s of saturation. But at this point, 20% of the solution signal is compromised. Considering that later on, images should be possible with the same settings, more protein might dampen the solution signal even further, and also in the interest of time, 25s saturation pulses were applied for all Z-spectra.

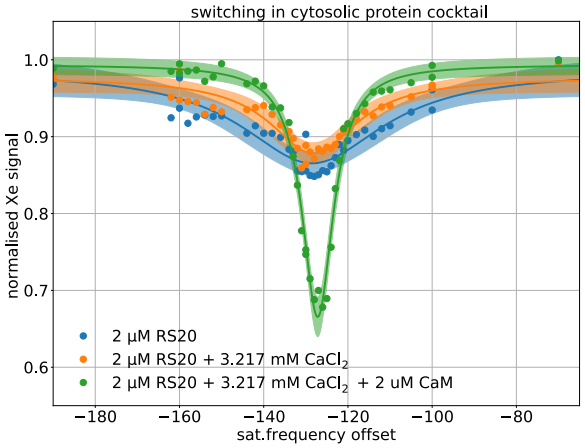

(a) Peptide RS20-CrA

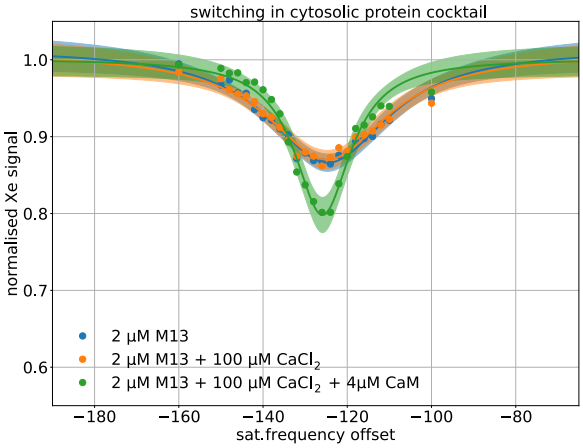

(b) Peptide M13-CrA

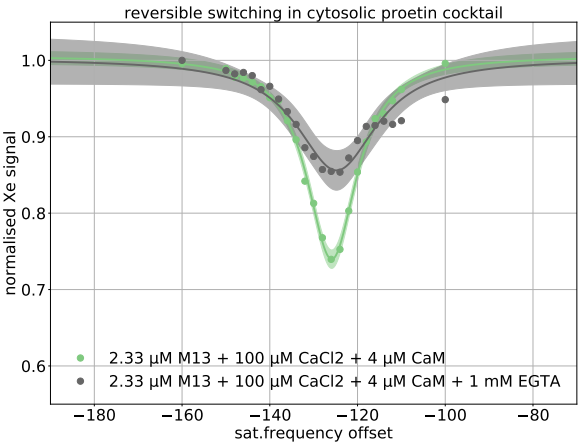

(c) Peptide M13-CrA

Figure 3.7: (a) and (b): The CrA- and fluorescein labeled peptides RS20 (a) and M13 (b) show unspecific interactions with components of a cytosolic protein cocktail, which manifest as a weak and broad CEST response, shown in blue. Calcium ($CaCl_2$) addition does not change that significantly (orange). The addition of CaM generates a sharper and more intense CEST response (green). (c): Upon EGTA addition, CaM-peptide binding is suppressed. This reduces the CEST response to background level (grey).

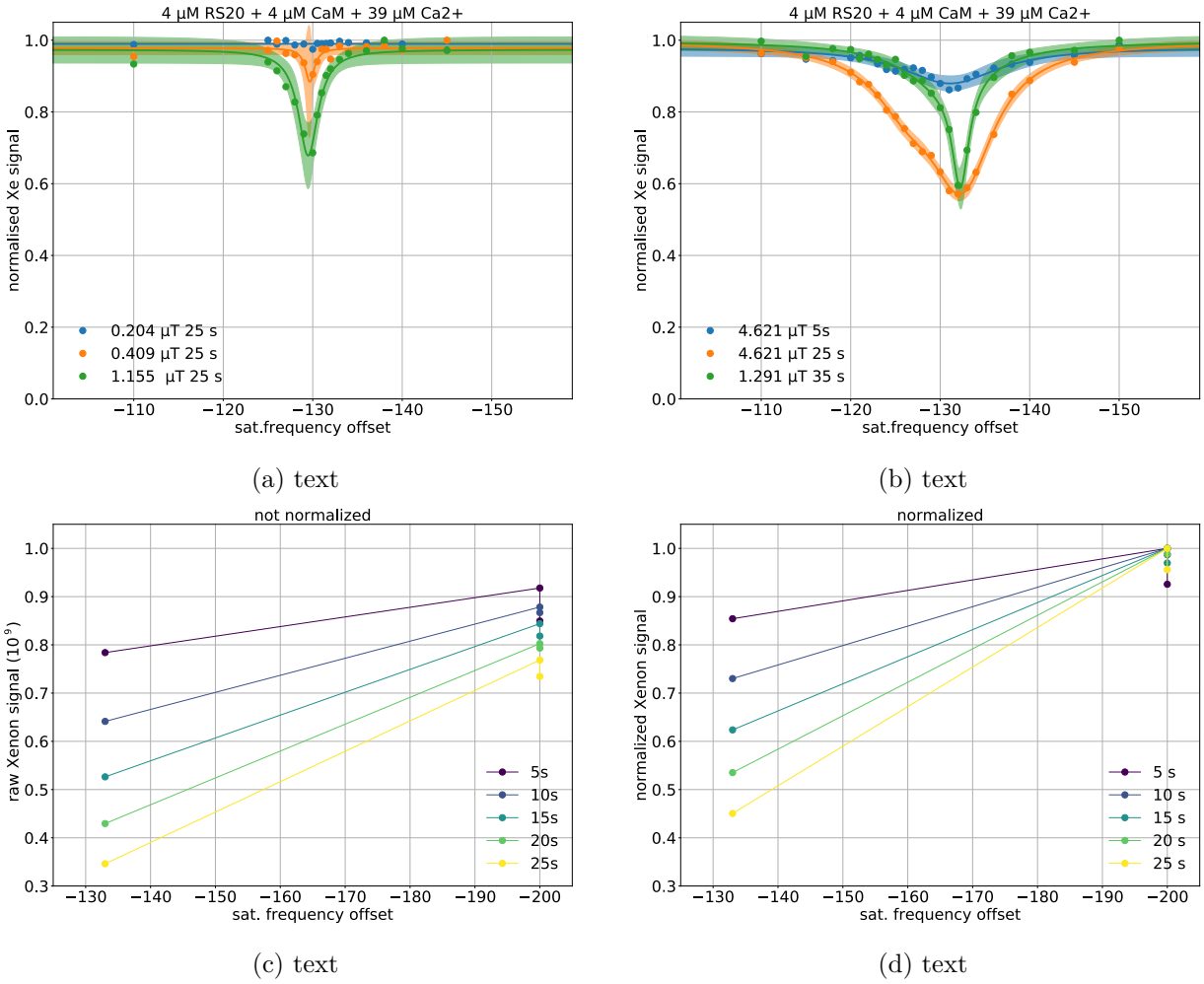

(a) text

(b) text

(c) text

(d) text

Figure 3.8: A: To reach maximum saturation, the pulse needs to be sufficiently strong. The pulse strength was scaled up until 40% saturation was reached, which is just over 1.155 µT. B: A further increase in pulse strength broadens the CEST, whilst maintaining the intensity. An increase in pulse duration mainly improves the resolution, and may also intensify the CEST to a certain extent. Longer pulses diminish the raw Xenon signal. This is shown in C and D, where raw Xenon data (C) is compared to normalized data(D).

3.2.5 Generation of MR Image Contrast

The MR images the were generated based on the xenon signal difference at the Xe@CrA frequency are shon in Fig.3.9. The on-resonant frequency for each image was derived from a previously acquired Z-spectrum. A frequency is on-resonant, if all xenon within a host cavity (e.g. Xe@CrA, or Xe@CrA-peptide) is depolarized while the saturation pulse at this specific frequency is irradiated on the sample. Off-resonant means that the polarization of the xenon in question is unaffected by a pulse at this frequency.

Images at an off-resonant and one on-resonant frequencies were acquired several times, averaged and compared. Usually, the off-resonant image is subtracted from the corresponding on-resonant one to derive the contrast. However, the more blurred and noisy images are, the more contrast is compromised, which is also the case here. So, in order to distinguish better, the images were left unprocessed and simply compared. A 2-compartment phantom was used for imaging two samples in one image. As a positive control, water samples with and without CrA-monoacid were compared. Figure 3.9A and B show how the inner compartment has full xenon signal in the off- resonant image, but much less in the on- resonant image, while the signal in the outer compartment remains on the same level. Images 3.9C and D depict a calcium-saturated sample in the inner compartment, and a calcium-depleted sample in the outer compartment. Both samples are otherwise of equal composition (4 µM sensor peptide RS20-W, 10 µM CaM). There is a signal reduction in the inner compartment, but also in the outer compartment. This could be due to the low image quality. The images 3.9A-D are noisy (the local intensity variation is quite large), as well as blurred (the central vertical part of the image appears brighter than the periphery). To improve the image quality in that respect, more averages were acquired, and concentrations were increased. For images 3.9E and F, the number of averages was raised from 4 to 25. To make sure the signal is clearer, the CrA-peptide concentration was raised as well, from 4 to 10 µM. To further ensure CaM excess, the CaM concentration was increased to 15 µM. Images 3.9E and F are much clearer and the contrast in the inner compartment is easier to grasp. The image contrast is not as strong as the contrast in the positive control (3.9A and B), but it is detectable.

3.3 Cause of Cryptophane-CEST Silencing

3.3.1 Hypothesis of Possible Explanation

The now characterized effect opens two possible paths of research:

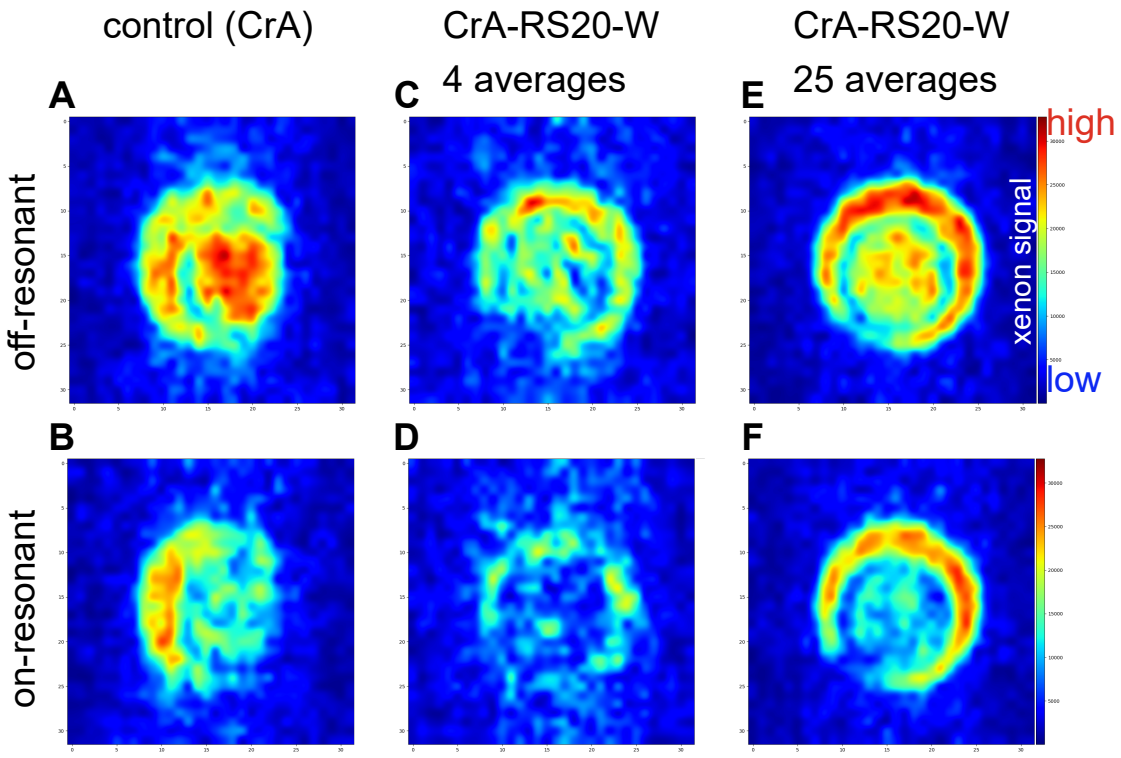

Figure 3.9: ^{129}Xe NMR Images: Top images were acquired with an off-resonant saturation pulse, bottom images were saturated on-resonant with Xe@host, such that upon xenon exchange, depolarization took place. A and B are a positive control. Inner compartment: Water with 0.8% DMSO and 4 µM CrA-monoacid, outer compartment: Water with 0.8% DMSO. C and D are an experiment with few (4) averages. Inner compartment: Ca^{2+} saturated (39 µM free Ca^{2+}) with 4 µM CrA-RS20-W-FAM and 10 µM CaM, outer compartment: zero free calcium (Ca^{2+}-depleted buffer) with 4 µM CrA-RS20-W-FAM and 10 µM CaM. Images E and F were generated with 25 averages. Samples for E and F were made with the same buffers and Ca^{2+} concentrations as C and D, but with 10 µM CrA-RS20-W-FAM and 15 µM CaM.

1. the most direct way to applications *in cellulo*, and the assessment of the sensor's performance in live cells

2. elucidation of the mechanism behind CrA silencing

The latter has been chosen as scope for this study, because understanding the mechanism is crucial for applying it, and might lead to significant improvements and more certainty about what to expect from potential applications. A clearly defined mechanism can be generalized and expanded to more applications.
Under the hypothesis of exclusive causality between CrA-CEST silencing and the biosensor, the influence of other sample components on the sensor's functionality around the CrA-CEST silencing was ruled out by a series of experiments.
To strengthen this hypothesis, I have tried to falsify it using all other sample components – without success. The samples made to characterize and quantify clacium calmodulin CrA-CEST silencing and reactivation do not contain components that influence it.

3.3.2 Ruling Out Influences of Other Sample Components

DMSO

Cryptophane-monoacid and peptides labeled with it do not dissolve well in water, therefore high concentration stock solutions are made in pure DMSO. Precipitation or aggregation upon subsequent dissolution in aqueous samples did not occur. The organic solvent DMSO can reactivate CEST silenced crytophanes, as shown initially in Fig.3.1 and in many control experiments. Every sample contains a small amount of DMSO, proportional to the CrA concentration: 0.8 vol.-%, unless otherwise stated. The DMSO content was always under 2 vol.-%. At these low concentrations, an effect on the reversible CEST silencing has not been observed. However, because DMSO influences the xenon dissolution, reversible cryptophane-xenon binding, fluorescence and optical anisotropy, the DMSO content should be the same across all samples that are compared.

Ions

Possible influences of ionic strength on the CrA-CEST silencing and reactivation were tested, and the result is shown in Fig.3.10. The CrA-CEST silencing of peptide CrA-M13-FAM remains unaffected by the 5-fold increase in the buffer concentration (and thereby ionic strength), shown in Fig.3.10 A by the blue and orange (5-fold buffer concentration) datapoints. A 3-fold dilution of

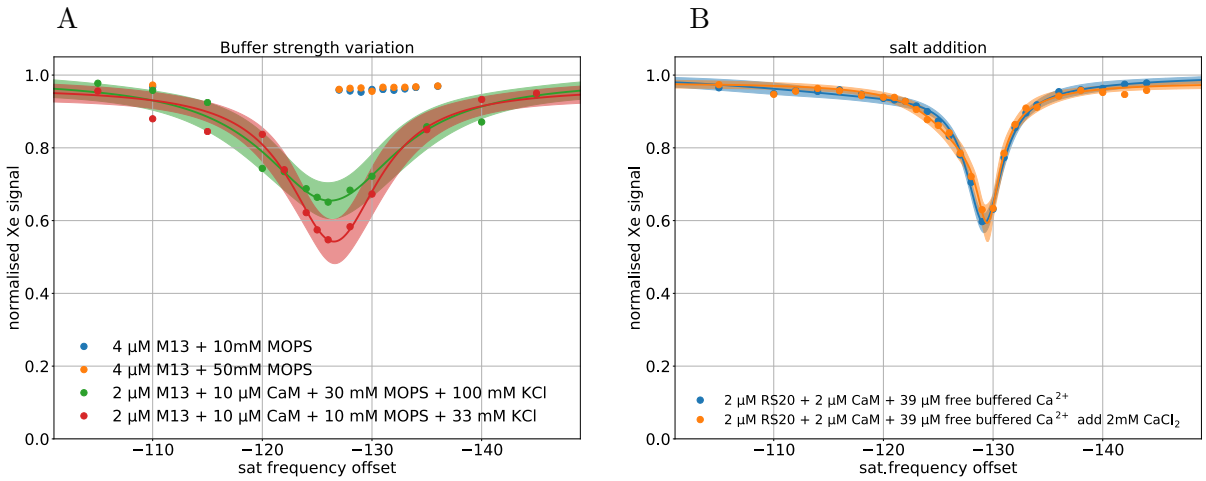

Figure 3.10: A: The peptide CrA-M13 is CEST-silent without Ca^{2+}-loaded CaM, regardless of the buffer strength (orange and blue datapoints). There is a CEST effect when Ca^{2+} loaded CaM is present (red and green curves), at either buffer strength, but the response is slightly intensified after the buffer is diluted. B: A commercially available Ca^{2+} buffer system was used for (B). The response of peptide RS20 did not change significantly after adding 2 mM $CaCl_2$ to the sample. The salt addition increased the ionic strength further.

the pH-buffer does not silence a CEST effect, reactivated by CaM-peptide binding. This is shown in Fig.3.10 A by the green and red curve, where the CEST effect that is pronounced in both cases. However, the CEST effect is slightly increased by the dilution of the pH-buffer, and the reason for this could be more than the standard deviation. This could be caused by variations in foaming, or a small increase in CrA-peptide concentration due to pipetting uncertainty for very small volumes (3-6µl), which was unavoidable when the buffer was diluted with CrA-peptide containing water. Either or both of the latter are more likely to be responsible for the increase of the CEST effect after buffer dilution than the decrease in ionic strength from the dilution.

Figure3.10 B illustrates, how the addition of 2 mM $CaCl_2$ does not influence the reactivated CEST effect. So, even larger variations in ionic strength do not affect the CEST response. Once the CaM is saturated with calcium, further calcium does not affect its stability.

Antifoam Agents and Micelles

Because protein samples foam strongly during bubbling with xenon gas mix, the antifoam agent is an absolutely necessary part of the sample. CaM does not influence the reversible xenon binding of CrA-monoacid. In Fig3.11, the Z-spectrum depicting CrA-monoacid in buffer with 4 µM CaM and 0.3 vol.-% antifoam (red) can be superimposed exactly on the Z-spectrum of an equal sample

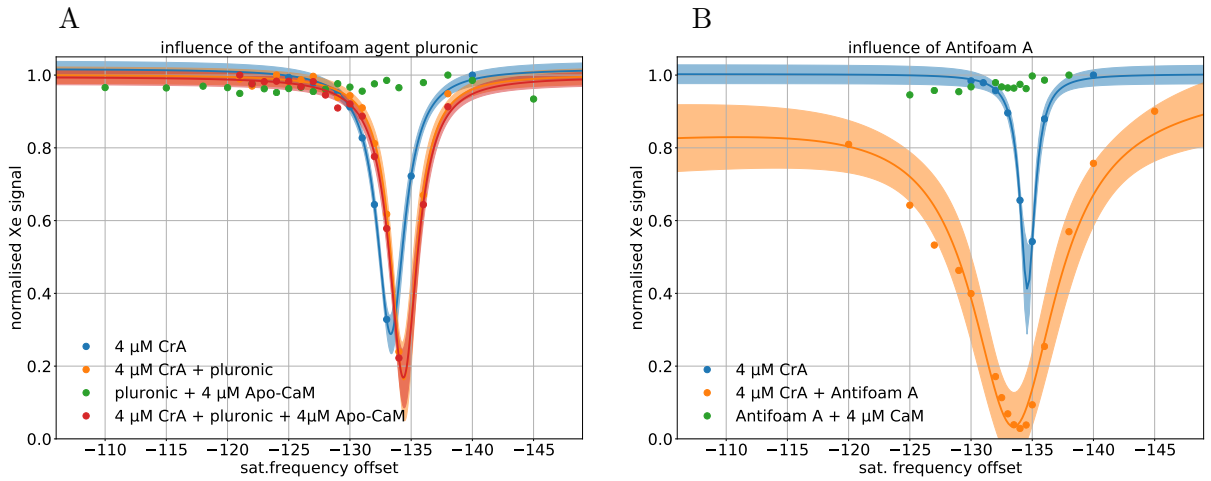

Figure 3.11: A:The CEST effect of 4 µM CrA-MA (blue) is compared to 4 µM CrA-MA with 0.3 vol.-% Pluronic (orange) and 4 µM CrA-MA with 0.3 vol.-% Pluronic and 4 µM Apo(Ca^{2+} depleted)-CaM. A small intensification and shift of the CEST separates the Pluronic-containing samples from samples without Pluronic. Lastly, the possibility of Apo-CaM and Pluronic forming any xenon exchanging aggregates is excluded, as there is no CEST (green datapoints) when the two are in solution. B: The foam reducer antifoam A interacts strongly with CrA (orange curve), as it broadens and intensifies the CEST effect, compared to just CrA-monoacid (blue). Antifoam A and Apo-CaM do not form any xenon exchanging aggregates (green). These interactions were measured in 30 mM MOPS Buffer with 100 mM KCl and 10 mM K_2EGTA at pH 7,2.

without CaM (orange). The green datapoints in Fig3.11 A show that CaM does not form xenon-exchanging aggregates with the antifoam of choice in this study, Pluronic L-81.

Usually, 0.1 vol.-% Pluronic are applied in our NMR samples. For the CaM titration with its high CaM concentration of 10 µM, and for the experiments with cytosolic protein cocktail, it was necessary to use 0.3 vol.-% Pluronic. Its high viscosity needs to be considered when pipetting small amounts of it, and when mixing the sample, and both needs to be done thoroughly and with the utmost consistency, to keep the experimental conditions constant. Being a surfactant, Pluronic forms aggregates. This is mainly why an eye needs to be kept on potential influences on the xenon exchange. Figure3.11 A illustrates that Pluronic slightly intensifies and shifts the CEST signal of CrA-monoacid in buffered aqueous solution: CrA-monoacid without Pluronic (blue) has a different and slightly less intense CEST signal than CrA-monoacid with 0.3 vol.-% Pluronic (orange). Just by the intensity, it is hard to say if the difference is significant, but there is also a small but notable CEST shift. The combination of the two speaks for a small influence of the Pluronic. However, if held this small and constant, this influence is not disturbing the reversible CrA silencing.

The dispersion behaviour of Pluronic is inconsistent, at times flakes may form, which dissolve

throughout the experiment. This is why sometimes it may take time and several rounds of bubbling and measuring to reduce foaming with Pluronic. Another antifoam agent was tested, in order to replace Pluronic: Antifoam A. The results of the experiments with antifoam A are shown in Fig.3.12. Its clearly visible micelle formation (sample looks milky, white and turbid) makes it impossible to use in the Calmodulin binding and CEST silencing experiments. But antifoam A can be used for experimenting CrA-monoacid and CrA-peptidesin the presence of micelles. CrA-monoacid is known to interact with micelles [73], which changes its xenon exchange pattern. The effect antifoam A has on CrA-monoacid is illustrated in Fig.3.11 B. The interaction intensifies CrA-mediated xenon exchange vastly (orange curve). The entire CEST signal comes from CrA-monoacid, because a control sample containing antifoam A with CaM (green datapoints) does not show any CEST signal. The enormous signal broadening that was observed when antifoam A was present, in comparison to CrA-MA in buffer (blue curve) without antifoam A suggests a much faster xenon exchange. Pluronic as a sample component can be ruled out as noteworthy influence the CrA-CEST silencing and reactivation. But the results shown in Fig.3.12 show that antifoam agents must be applied with utmost caution in CrA- CEST silencing and reactivation experimets, especially when there are cell penetrating or membrane anchoring peptides involved. The immense effect of antifoam A shown in Fig.3.12A illustrates how immensely the reversible CrA-xenon binding can be influenced by micellar structures, which antifoam agents tend to form. Considering that 0,3 vol.-% of antifoam A was plenty to reactivate CEST-silent CrA-peptides, and compared to CrA-CEST reactivation by CaM binding, the CEST effect is quite extreme. This effect was further investigated, and shown to be salt-dependent in intensity (Fig.3.12B) and chemical shift(Fig.3.12C). With increasing salt (NaCl) concentration, the CEST effect intensified in both the minimum of the lorentzian fit curve (green bars in Fig.3.12B) and the area under the curve (purple bars in Fig.3.12B). Like the CEST response, the chemical shift shift $\Delta\delta$increases with almost perfectly linear dependence on the ionic strength, shown in Fig3.12 C.

Cytosolic Proteins

As shown before in Fig3.7, cytosolic proteins generate a weak and broad CEST response. However, the calcium-CaM dependent CEST response remains unaffectedly detectable. Experiments in cells disrupted by bubbling have not been successful. As soon as the cells were disrupted by bubbling, signal could not be obtained, in spite of cooling and chemical protein protection. There were also foaming issues that could not be solved with Pluronic L-81.

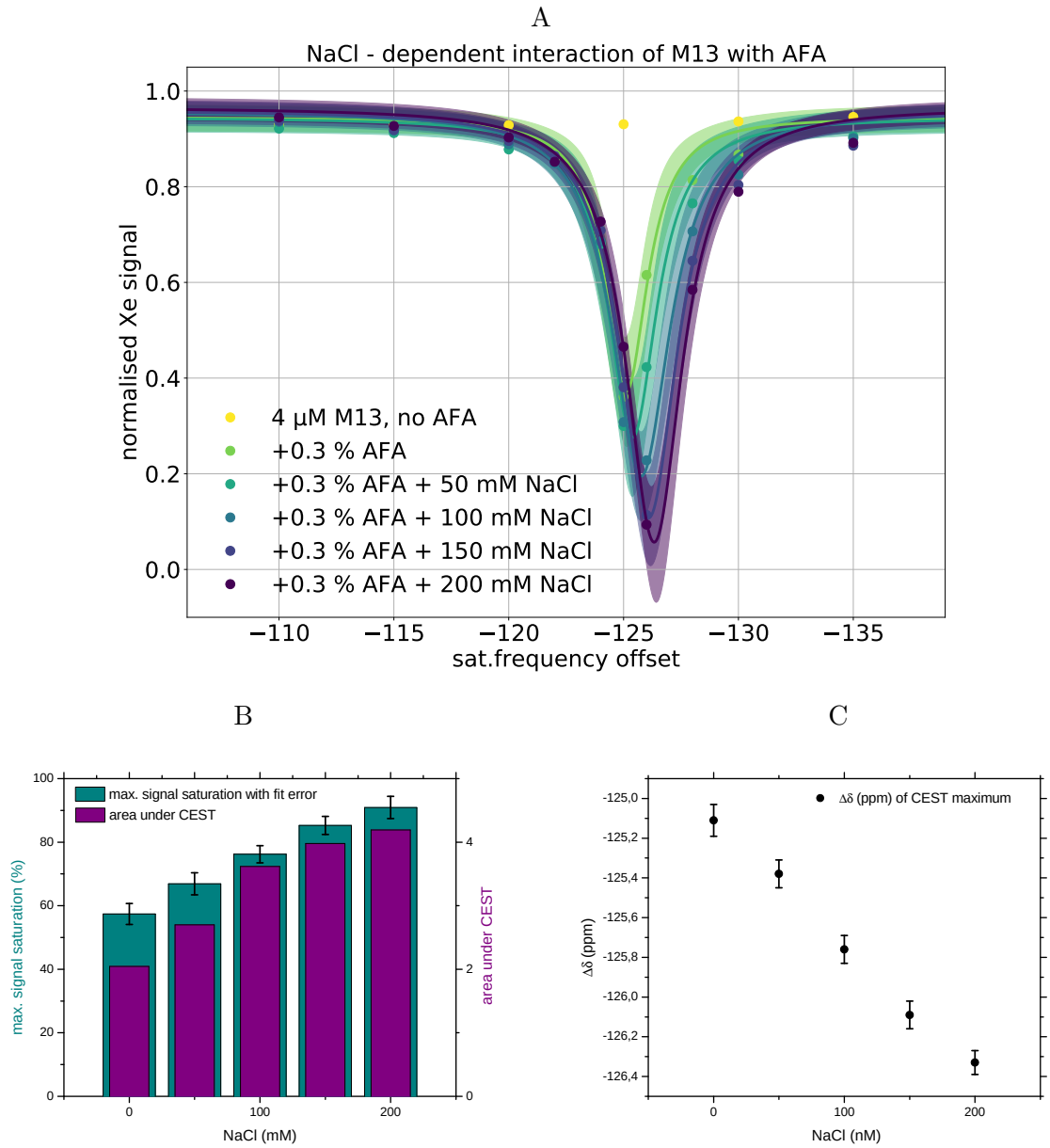

Figure 3.12: A: 0.3 vol.-% of Antifoam A reactivate the silent CrA-peptide M13, and the CEST response starts at 60% saturation. The CEST is intensified by increasing the NaCl concentration. B: The increase of the CEST response is also reflected in the area under the CEST (purple). That and the minimum of the fit function (green) show the same tendency. Both appear to be reliable measures for the CEST magnitude. C: Another effect of the salt concentration is a chemical shift change of 1ppm per 200mM NaCl. Like the CEST increase, the chemical shift change linearly depends on the NaCl concentration.

3.3.3 Ruling Out Intermolecular and Intramolecular Interactions

Self – Aggregation

Aggregation is suspected to influence CrA's xenon exchange more than anticipated and has been studied with CrA-conjugates before [95]. Indeed, their poor water solubility allows the thought that CrA and its derivates may often not be free and monomeric in solution, but clustered in aggregates. These aggregates may well have an influence on the xenon exchange dynamics, so that exchange modulations should be accompanied by the consideration of aggregation phenomena as possible cause or influence. At concentrations like 100 µM, self-aggregation is not very surprising. A dynamic light scattering (DLS) assay, shown in Fig.3.13, reveals that both CrA-M13 (3.13A) and CrA-RS20 (3.13B) aggregate at 100 µM. The aggregates are mostly between 100 and 1000 nm in diameter. The working concentration at which the CrA CEST silencing was observed with HyperCEST NMR spectroscopy in this lab (1-10 µM) is however nowehere near the detection range of DLS. A previous study [64] observed a CaM-binding cryptophane-labeled peptide at 70 µM in direct HP-^{129}Xe NMR spectroscopy, which was silenced reversibly without side effects by aggregation phenomena. To find out what is happening at the working concentration, we made use of the peptides with a fluorescent moiety and measured its fluorscence polarization (FP). The FP functions as a reporter signal for the tumbling rate and motility, and consequently, size of an aggregate or complex in solution. An FP assay has certain prerequisites and limitations. For instance, the molecule size needs to increase by at least 4-fold in molecular mass in order to be detected as an FP increase. This means, dimerizations of CrA-peptides cannot be detected by FP. Previous unpublished studies by Westmeyer et.al. have used other means to exclude dimerization as the cause for CrA silencing or reactivation. Fortunately this means:

- Any aggregates from tetramers upward can be detected
- The binding of the roughly 4kDa CrA-peptides to CaM (16.7kDa) can be detected

Self-aggregation can be shown for a model compound, as depicted in Fig.3.14, by adding more and more of a non fluorescent molecule to its fluorescent version. With the model compound in Fig.3.14, a formation of aggregates is indicated by the increase in FP from one plateau to another, correlating with an increase in molecule size. CrA-RS20 was tested for self-aggregation in the same manner. The experiment was done under Ca^{2+}-depleted and Ca^{2+}-saturated conditions, to check for the unlikely event of an influence by Ca^{2+}. The similarity of the FP (Fig.3.14, red and blue datapoints) curves does not speak for any such influence. Approaching 100x excess of the

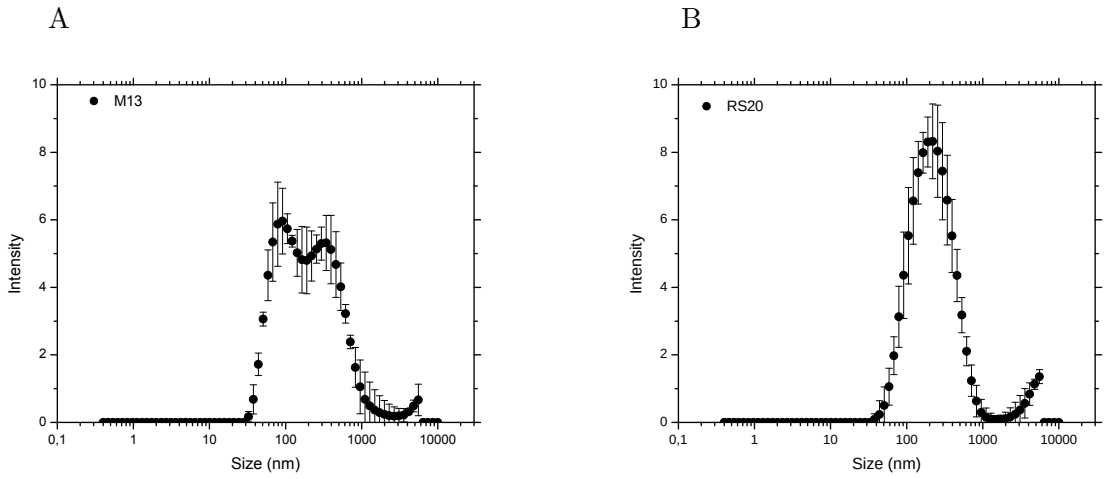

Figure 3.13: Intensity distribution of dynamic light scattering (DLS) of 100 µM of CrA-labeled peptides without fluorescein in water. The average and standard deviation of triplicates are shown. The formation of self-aggregates at a concentration of 100 µM is evident here, but does not allow conclusions about any aggregation behaviour under 10 µM. A: CrA-M13 appears to form self-aggregates of different sizes, distributed around 100 and 400 nM in diameter. B: CrA-RS20 forms self-aggregates, which are distributed around 250 nM in diameter.

non fluorescent equivalent peptides, there might be a tendency of beginning FP increase in the experiments with the CrA-peptides, see Fig.3.14 in the red and blue datapoint, but nothing like the micelle formation in the model compound (black sigmoidal curve in Fig.3.14). Going beyond 100x excess would mean a concentration of 10-100 µM, where aggregates have been observed by DLS. These concentrations are far beyond the NMR working concentration, and are accompanied by a DMSO content of roughly 10%, which dampens the fluorescence to an extent that would make FP measurements invalid. At the working concentration, which is between 1 and 10 µM, there is no notable increase in molecule size, so that within this range, self-aggregation can be excluded.

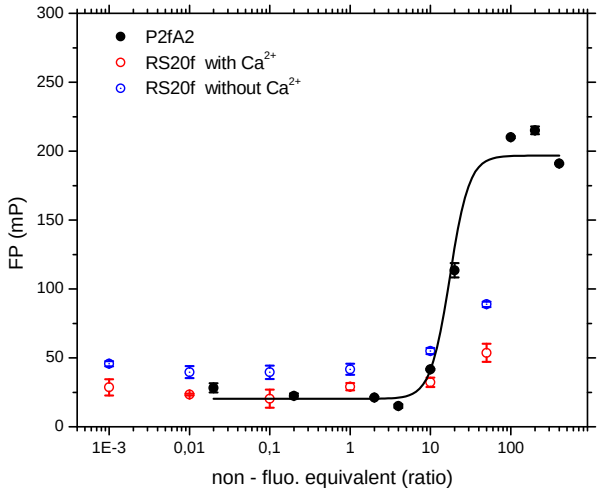

Figure 3.14: Fluorescence polarization (FP) of RS20f titrated with its non fluorescent equivalent RS20 (red and blue), compared to the peptide P2fA2 (black), which is designed and known to form micelles. P2fA2 was also titrated with its non fluorescent equivalent P2A2. While P2fA2 shows an FP transition between 10 and 100x excess, RS20f shows only slight FP increase at 50x excess, which is 5-fold the maximal working concentration. The RS20 titration was done with and without free Ca^{2+}, and in both cases, there is a similar hint of beginning aggregation at 50x excess RS20, but no sign of aggregation between 1 and 10µM.

Tryptophan

An interaction between aromatic and/or hydrophobic AA residues on the peptide and CrA has been proposed as potential influence on CrA mediated xenon exchange [65].Later, the same authors hypothesized a proximity of aromatic residues as cause for CrA silencing [64]. Because W is close to the CrA functionalization on the peptide, the hypothesis seemed reasonable. Put to the test, it turned out not to be the cause.

As shown in Fig. 3.14, the peptide with the W/L substitution responds just the way all other switching peptides do: it is CEST - silent, unless bound by CaM, which is strictly calcium dependent. A small influence on the chemical shift proposed by Riggle et.al. in 2015 [65] may still be possible, however, there is no observable influence on the CrA CEST silencing.

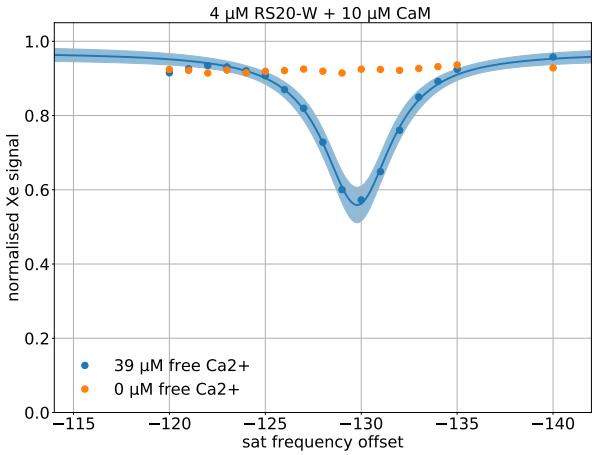

Figure 3.15: In this Z spectrum, the response of peptide RS20-W, with a tryptophan-leucine substitution, resembles the responses of all other switchable CrA-peptides: CrA is silent in calcium depletion (orange) and responsive upon CaM binding, requiring calcium saturation (blue).

Arginine

One thing all switching CrA-peptides have in common is the two arginines (RR) neighbouring the CrA-carrying K residue in C-terminal direction. Arginine features a guanidine group, which is highly positively charged. This enables it to engage in cation-pi interactions with aromatic side chains of nearby amino acids. Cation-pi interactions are strong interactions which play a key role in molecular recognition[58,61]. Aromatic AA residues (P, Y, W) provide the necessary delocalized (π) electron systems, which interact with positively charged side chains (R, K). Cryptophane contains plenty of armoatic ring sructures and consequently, πelectron systems. Therefore it might possibly engage in cation-pi interactions with the nearby R residues, with possible impact on the CrA accessibility. If cation-pi interactions are the cause for reversible CrA silencing, only the C-terminal residues of our CrA-peptides should be sufficient to inhibit xenon exchange. The short peptide GRRK-CrA, consisting only of the C-terminal AA residues and CrA, was tested in aqueous solution DMSO.

Figure 3.16 shows, that the C terminal residues alone suffice for a silent CrA on the short peptide in aqueous buffered solution (green datapoints) and pure water (strong orange datapoints). The difference to a DMSO sample with an equal amount of GRRK-CrA (strong blue curve) and a water sample with an equal amount of CrA-monoacid (light orange curve) is significant.

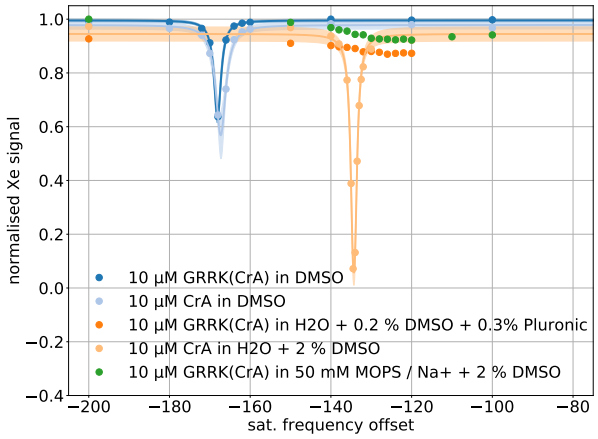

Figure 3.16: The z spectra of 10µM peptide GRRK(CrA) in DMSO, and CrA-MA in comparison (blues) show that CrA on the peptide is exchanging xenon without impediment. The peptide in water is silent, compared to an equal amount of CrA-MA (oranges). The peptide in MOPS buffer (green) is equally silent. A peptide sequence this short already inhibits xenon exchange completely.

To determine if the cation-pi interactions are the reason for this CrA CEST silencing, the RR in the entire RS20 peptide were substituted by AA, and the resulting peptide, GAA-K(CrA)-WQKTGHAVRAIGRLSSSC(5-Fluo-M)-amide, was tested. Figure 3.17 shows, how the peptides with the substitution RR/AA, and the peptide GRRK(CrA) are almost, but not entirely silent. There is a weak and probably unspecific background CEST-effect. Because it is so weak and broad, it does not show in the fine sampled Z spectra of Fig.3.16. With considerably broader sampling, the very short peptide GRRK(CrA) revealed a similar, but smaller effect. Hence, the CrA is not entirely silenced, but mostly silenced, especially when it is compared to the equal amount of CrA-monoacid.

Unfortunately, this does not allow the conclusion, that cation-pi interactions, and nothing else, inhibit xenon exchange. The fact that Alanine (A) residues do not make a difference makes cation-pi interactions, and other specific electrostatic interactions rather unlikely. But these two CrA-peptides could be silenced by two independent mechanisms. To test, whether the cation-pi interactions are one of these two hypothetical silencing mechanisms, the short peptide GAAK(CrA) has been synthesized and tested. But also this CrA-peptide ist still CEST-silent in aqueous solution, while in DMSO, it has a CEST effect, as the Z-spectra in Fig3.18 show.

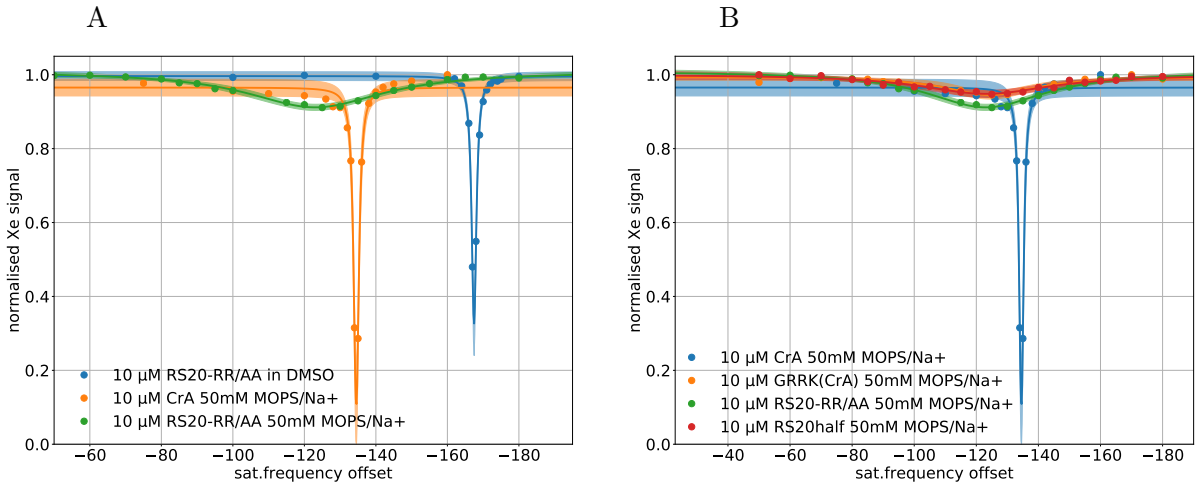

Figure 3.17: A: The Z spectra of the CrA-RS20 peptide with an RR/AA exchange in DMSO (blue) and in buffer (green), compared to the same amount of CrA in buffer (orange). a very weak and broad CEST is recognizable from CrA-RS20 RR/AA in buffer, showing that the xenon exchange is inhibited, but not completely silenced.
B: Other peptides also display the same weak and broad CEST. The short GRRK(CrA) (orange), as well as the C terminal fragment of RS20, GRRK(CrA)WQKTGHAVK (red), show a weak and broad CEST, similar to the CrA-RS20 RR/AA (green). Compared to CrA-MA in buffer (blue).

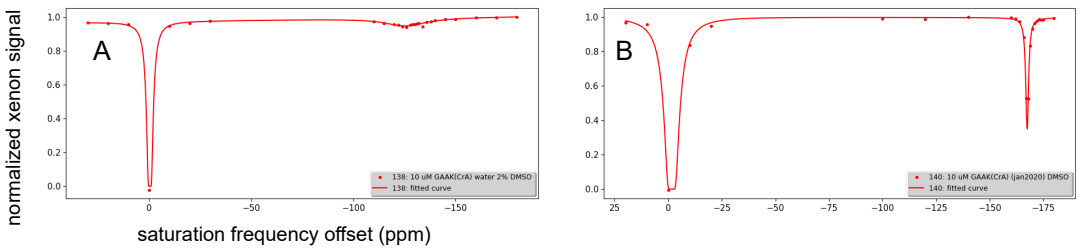

Figure 3.18: Z-spectra of GAAK-CrA peptide in water with 2% DMSO (A) and 100%DMSO (B), kindly provided by Dr. J.O.Jost.

Structural Conformation

CrA silencing could be caused by a sterical obstruction of the CrA portals by the unstructured peptide. Peptides of a length of about 20 AA are usually unstructured in aqueous solution. By assuming a rigid secondary structure, the peptide is no longer able to block any CrA portals. Wrap-around binding with CaM demands such a rigid, helical conformation. Xenon HyperCEST results combined with circular dichroism (CD) spectroscopy results allow the interpretation that a solvent change towards TFE (trifluoroethanol) leads to a more helical conformation (CD), and at the same time, to the reconstitution of the CEST response. One of the things strongly influencing the structure of a peptide in solution is solvent change. Trifluoroethanol (TFE) has the property to stabilize helix formation in peptide structures that are prone to assume helical conformation [82]. So, TFE was used to emphasize the tendency towards helical conformation in the CaM-binding peptides in the absence of their binding partner CaM. Figure3.19a shows the Z spectra of CrA-M13-FAM and CrA-RS20-FAM in different solvents: pure water, water with 20% TFE and water with 50% TFE. As a control, an equal concentration of CrA monoacid was measured in the same solvents. The CEST effect was remediated by TFE, and was most pronounced with 20% TFE. At 50% TFE, there was a smaller CEST effect.

Figure 3.19a also shows the TFE-dependent change in conformation towards a defined secondary structure of the peptide. The more TFE a sample contained, the more helical structure was recognized in the CD spectrum. The helicity was determined in % contributing residues, according to Brahms & Brahms [12]. The calculated overall helicity is moderate, but an increase in helicity is notable. Equivalent samples were tested for xenon exchange. Note, that in this experiment, xenon solubility and exchange dynamics are influenced by the solvent change and the structural rearrangement of the peptide. The ratio between the CrA-peptide and the CrA-MA has changed with the increase from 20% TFE to 50% TFE. The control experiment with CrA-monoacid in the same solvent shows the influence of the peptide on the CrA mediated xenon exchange. Comparison of the CEST effects from CrA-monoacid between the different solvents does not reveal much about the xenon exchange in general. For this, more parallel CrA- monoacid experiments would need to be done.

Comparing the solution signals, as shown in Fig. 3.19b provides an estimate of how the xenon solubility is changed by the solvent. In water, the Xe@solution signal is a bit higher than in 20% TFE. In 50% TFE, it is about twice as high as in water. More data would be necessary to clothe this in numbers, but the rough estimation, that 50% TFE substantially increase the Xe@solution signal, is the information most needed to iterpret the Z-spectra in Fig. 3.19a.

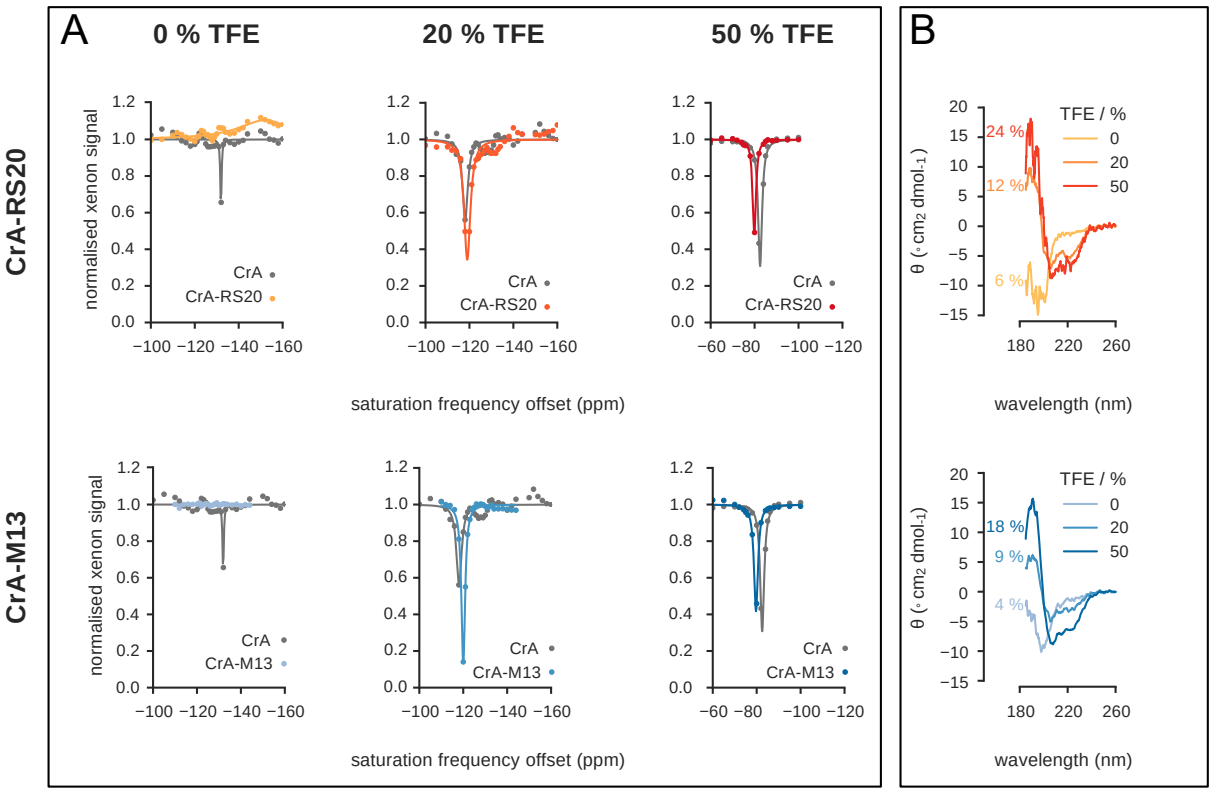

(a) A: Z-spectra of CrA-peptides RS20 and M13 in the solvents water, water with 20% TFE and water with 50% TFE. The peptides are CEST-silent in water, and CEST-activated by the solvent TFE. At 20% TFE, the CEST effect is most pronounced for both peptides. B:The enhanced manifestation of the helix propensity in both peptides, induced by TFE. This is demonstrated by CD spectroscopy, and spectra been evaluated by a deconvolution according to the method of Brahms&Brahms [12]. The % helicity calculated in the deconvolution is denoted in the graphs and relates to the contributions of AA residues.

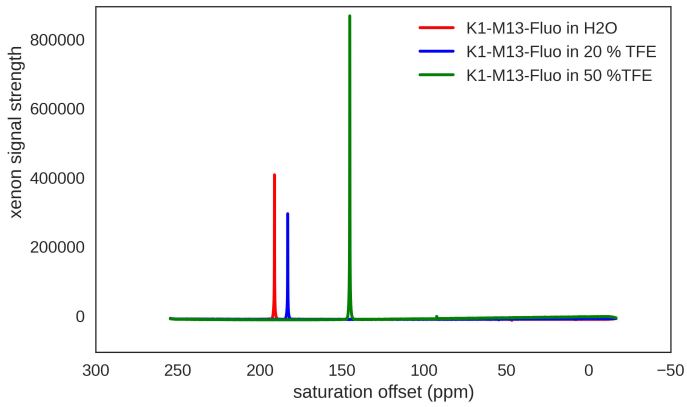

(b) Solution signal (Xe@Solution) in a direct xenon NMR spectrum of the different solvents water, water with 20% TFE and water with 50% TFE.

Figure 3.19: The effects of the organic solvent trifluoroethanol (TFE) on the cryptophane-peptides are expressed in the Z - spectra (A) and the helix propensity (B). The Xe@solution signal is affected by the solvent, too (b).

4 Discussion

4.1 The Interaction Network Around Cryptophane Silencing

The initial observation leading to this study has been investigated, and issues have been addressed from multiple directions. Cryptophane CEST can be reversibly silenced in a controlled manner, and this can be used as reporting mechanism, indicating molecular changes in concentrations in the sub-μM regime.

Figure 4.1, which is a highly simplified schematic, represents of the involved molecules and the network of interactions between them. The complex network and a more appropriate mathematical description of this particluar process are elaborated on in full complexity by Valeyev et.al. [85]. The incorporation of calcium ions into calmodulin (CaM) is an example for the hidden complexity: the 4-stage cooperative binding process, sublty indicated by the wavy line, causes the conformational rearrangement of the protein from apo-CaM into holo-CaM, as well as peptide binding. Both of the latter facilitate the progression of calcium binding, and vice versa. Even in the absence of calcium, apo-CaM and the peptide RS20 interact and bind, but this has only been observed when there are absolutely no salts around [84].

4.1.1 CaM-Peptide Binding and Calcium Sensitive Range

The binding interactions between CaM and the peptide are illustrated schematically in figure 4.2. Four different processes cooperate and contribute to this interaction:

1. The Ca^{2+} uptake of CaM
2. The conformational change from apo-CaM to holo-CaM and its cooperation with peptide binding
3. CaM-peptide binding
4. The conformational change of the peptide

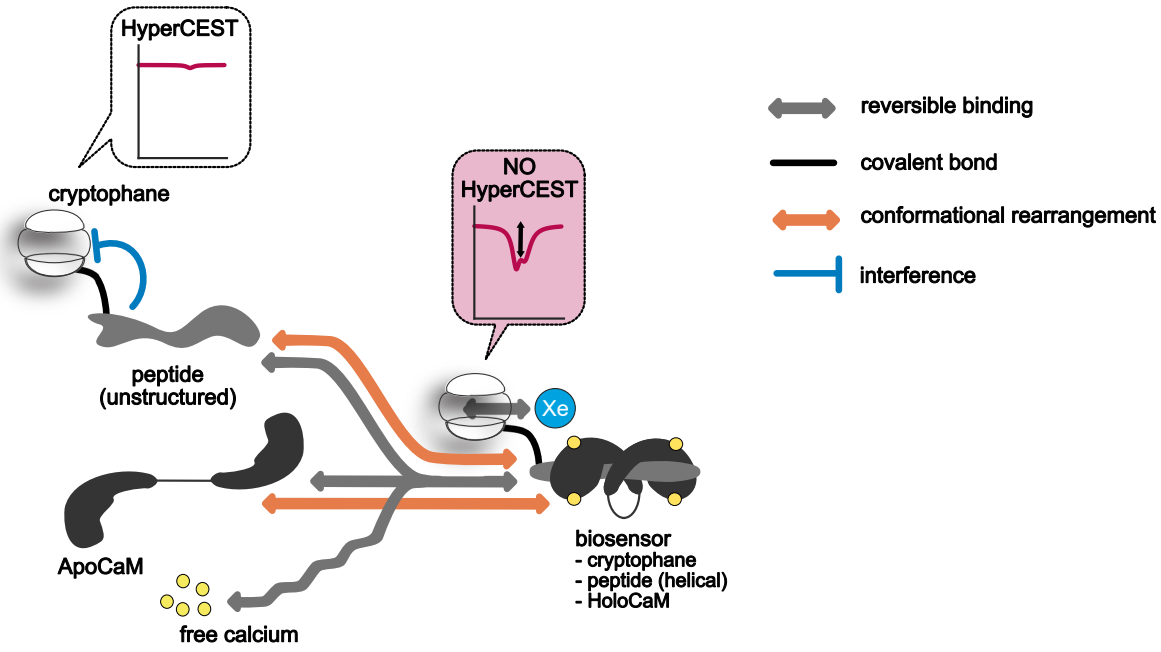

Figure 4.1: Schematic representation of the biosensor principle, showing the interactions whithin the molecular ensemble in rough categories: conformational change (orange), chemical exchange or binding (grey) and inhibition of xenon binding (blue). The molecular subunits are shown as pictograms.

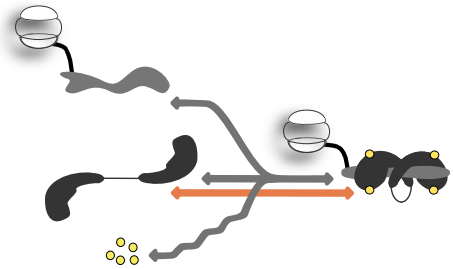

Figure 4.2: Schematic representation of the multistep peptide-calmodulin binding.

Calmodulin and its binding partners are known to bind in many different ways, of which the most relevant here is the calcium dependent wrap-around binding, because calcium signals are transmitted this way to Myosin Light Chain Kinases (MLCK), which are the origin of the peptides used in this study. In a pH buffered solution with sufficient free calcium, it should be predominant, if not exclusive.

The sensitive range described in 4.2.2. includes all the parts of this biosensor: Calcium, CaM, peptide, Cryptophane, Xenon. As it can be expressed explicitly as calcium concentration, the calcium sensitive range of this biosensor is finally determined. The CrA-RS20-FAM titrations were done with a higher CaM concentration (Fig.3.4b) , and with a higher peptide concentration, CaM concentration and CaM/peptide ratio (Fig.3.4c). In both cases, there was a barely significant shift in EC_{50}, expressed as relative CaM saturation. Considering the standard error of 0.18, a shift of 0.22 is probably not significant. But to support this claim, more experimental data is required. The calcium titration of CrA-M13-FAM has an EC_{50} close to that of the CrA-RS20-FAM titrations, but being a different peptide, it is far more likely that this titration has a truly different dynamic. That the dynamics are very similar is probably due to the functional and regulatory similarity here: RS20 and M13 are both derived from Myosin Light Chain Kinases (MLCK): M13 is from skeletal muscle MLCK, while RS20 is from smooth muscle MLCK. A calcium signal *in vivo* would lead to activation of the MLCK enzyme, light chain prosphorylation, and ultimately, muscle contraction. Differences and uncertainties included, a signal and decent contrast can probably be acquired with this biosensor between 0.5 and 1 µM free calcium.

The AUC development in the different calcium titrations appears to have similar dynamics across the experiments. I use this careful expression, because the AUC from a xenon Z-spectrum as a measure for a physical or chemical process has not been used before and cannot be termed a direct indicator of it. This may be the case after a few more research projects are completed in this field,

but currently, this is not confirmed. Every CEST response shown in Fig3.4 is a superposition of several processes, of which the initial one, calcium-CaM binding, enables CaM-peptide binding. As mentioned in the introduction and the previously presented results, those are two sigmoidal processes, which under the given conditions are inseparable and take place in superposition. Two more chemical processes are leading to a CEST response: the mechanism remediating cryptophane CEST silencing, and the reversible cryptophane-xenon binding. These processes also contribute their own dynamics to the development of the CEST response and its AUC. It is quite likely that they are on the same time scale as calcium-CaM-peptide binding, and their contributions, whatever their nature, cannot be neglected, until it is ensured that these processes are in equilibrium.

4.1.2 Conformational Rearrangement of the Peptide

The conformational rearrangement of the peptide is illustrated schematically in figure 4.3.

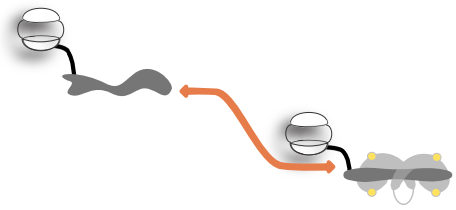

Figure 4.3: The orange arrow is a schematic representation of the peptide's conformational rearrangement.The peptide with the terminally attached cryptophane is represented by the grey body in two different conformations, Calmodulin wrapping around it is shown in light grey.

The CD spectra reveal that, with increasing TFE content, the peptides have an increasingly helical CD profile. In Xenon HyperCEST NMR, an increasng TFE content is correlated with reactivation of silenced cryptophane.

The xenon solution signal in 50% TFE is around twice the solution signal, compared to xenon in water, due to the better solubility of xenon in TFE. This reflects the solvent change quite well. Apparently, TFE enhances the dissolution of xenon. This should lead to a smaller CEST effect, as the exchanging pool of xenon is relatively smaller against a larger solution pool. To the contrary, the CEST effect is larger, which can be caused by a much faster exchange of Xenon. The CEST effect in 50% TFE is also substantially borader than in water, which speaks for a faster exchange.

The ratio between the CEST responses of CrA/peptide-CrA has changed because the xenon solubility is enhanced by TFE. That also matches the increased (doubled) solution signal. With more TFE in the solvent, the Xenon@solution pool enlarges, and consequently, the fraction of Xe@CrA decreases (because the concentration of CrA is constant). So, if the Xe@CrA fraction is smaller, the CEST response, which is normalized to the solution signal, is also smaller. That explains the CEST responses from the CrA-peptides, but not the responses from CrA-monoacid. The CrA-peptide would, by this theory, keep exchanging xenon at a similar rate, despite the solvent change. But the CrA-monoacid appears to exchange Xenon faster as the TFE content increases, eventually surpassing the CrA-peptide's exchange rate somewhere between 20 and 50% TFE. Under the hypothesis, that the peptide prevents the solvent-dependent increase of the xenon exchange rate, this data can be explained. But without more experimental data to support this hypothesis, it is only speculation.

As both aforementioned effects are independent of cryptophane silencing, and the remediation of cryptophane silencing also happens without TFE, the induced helicity of the peptide remains the main contributor to the remediation of cryptophane silencing. The magnitude of the response resulting thereof is most likely a result of the solvent change. The reactivation of the CEST response, however, is most likely caused via proxy by a change in the secondary structure of the peptide.

The unstructured conformation of the peptide was long thought to be identical with the cryptophane silencing mechanism, and this might still be the case for peptides long enough to ba able to alternate between structured and unstructured conformations. However, the final results (that show reversible cryptophane silencing without the possibility of any secondary structure) in this study suggest that the conformational change (like target binding and calcium incorporation) is just one of many influences on the actual silencing mechanism.

4.1.3 Influence of the Peptide on the Cryptophane

The interaction, which is essential for cryptophane silencing is the unknown inhibitory influence of the peptide on the cryptophane. It is illustrated by the blue inhibition sign in figure 4.4.

The efforts in determining the molecular mechanism causing cryptophane silencing lead to the exclusion of several possible reasons:

- Aromatic interactions between the W1 residue and cryptophane are not the reason for cryptophane silencing. The authors of[65,95] propose it, calling it on/off switching, without further details about the mechanism. Their hypothesis is based on the correlation of the effects W1

Figure 4.4: The blue inhibition sign is a schematic representation of cryptophane silencing. The grey body again represents the peptide.

and cryptophane have on the fluorescence of one another. In this study, the W1 residue was replaced by an A residue, and the otherwise equal peptide was still silenced, which puts the W residue out of the question.

- Interactions with specific residues, especially the ones anchoring the calmodulin binding, were generally quite plausible as the cause for cryptophane silencing. However, none of the remaining anchor residues of both peptides have an influence on the CEST effect or its modulation. Phenylalanine (F) or Leucine (L), 14 residues away from W1, have no influence on the CEST and its modulation. In a HyperCEST experiment, the peptide GRRK(CrA)WQKTGHAVK, which is an N-terminally truncated RS20, silences cryptophane just as the entire peptide does, as figure 3.17 in the results chapter, section 3.3.3, subsection: Arginine. shows. There is some xenon exchange, but the CEST is extremely weak and broad, and therefore highly unlikely to originate from one specific exchange site.

- The anchoring Phenylalanine (F) 5 residues away from W1 is only present in M13, which excludes it from having a general influence on cryptophane silencing.

- Albeit Arginine (R) is not an anchoring residue, interactions between calmodulin and arginine residues relevant to binding have been documented in the cases of Calcineurin [35] and skMLCK (which contains the M13 sequence) [55]. Smooth muscle and other MLCK calmodulin binding regions with a sequence similar to RS20 contain R residues that are essential for calmodulin binding, too [6,27]. R is a positively charged residue, which is known to engange in cation-pi residues, contributing significantly to protein-protein-interactions. The high likelihood of cation-pi interactions between R residues and cryptophane gave the incentive to experimentally investigate their role. But a substitution of the two R residues neighboring

the cryptophane-bearing K residue by A did not reactivate the silenced CrA. Stunningly, even a radically truncated version of the peptide without R residues is still able to silence the cryptophane. This is the smallest peptide that still silences cryptophane. It is depicted in Figure 4.5. As there were no other charged or aromatic residues in cryptophane's vicinity, polar and non-polar interactions with one specific residue in cryptophane's vicinity can be excluded as the cause for cryptophane silencing.

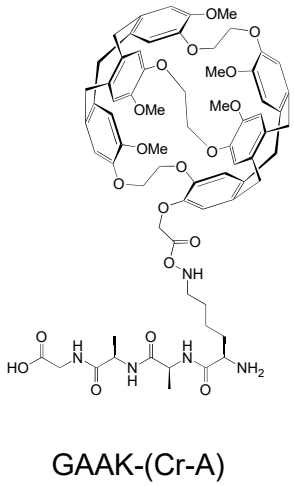

Figure 4.5: smallest cryptophane-silencing peptide, GAAK(CrA).

In conclusion, neither the total length of the peptide nor any of the investigated residues play a key role in cryptophane silencing. Presumably, it takes just an attachment of a few rather arbitrary amino acids to silence cryptophane. A molecule this small can be subjected to more different spectroscopical analysis tools, as well as molecular dynamics simulation studies, than the full-length peptide.

4.1.4 Possibilities of Cryptophane Silencing

Cryptophane silencing is, essentially, preventing xenon access or exchange. To prevent xenon exchange, one needs to either prevent xenon from entering the cryptophane cavity or prevent xenon from exiting the cavity again. The first can be accomplished by an imploded cryptophane conformer, a superior competing guest, or self-encapsulation, which is a moiety within the same

molecule acting as a superior competing guest. Another scenario might be a blockage of the portals, upon which the cavity is empty, which forces it to implode. The second can be accomplished by any disruption of the "sliding door" gating mechanism after xenon has entered the cavity. Such a disruption could be the outcome of slow intramolecular interactions that compromise the flexibility of the linkers, or block the access to the portals.

Self-encapsulation, as described in [9], has been observed in cryptophanes with linkers of different length (asymmetric linkers). Given sufficient length, the longest linker can fold and insert in the cavity, preventing it from imploding. This has only been observed for the linkers in unconjugated cryptophanes, but might as well be a possibility for other, functional moieties on the cryptophane. As the inserting moiety is within the moelcule, it can be considered a rather strongly competing guest.

Cryptophane, its conformers and their abundance have been introduced in section 1.1.7 in the introduction. Here, the likelihood of an imploded conformer of a CrA covalently bound to a peptide, and its possible role in cryptophane silencing, shall be discussed. The conformational ensemble of cryptophane primarily depends on the molecular architecture of the respective cryptophane. It is desribed in [24], how an imploded conformer is always the result of an inherently reversible energetical state. The imploded conformation is hardly stable and will change as soon as there is an energetically more favourable state available. The longer and more flexible the linkers between the CTV caps are, the greater is the energetic gap between the imploded and expanded states. CrA is a comparatively small host with short linkers, therefore it is conformationally quite rigid [24]. An imploded CrA conformer is energetically more favourable than sustaining a cavity without a host. For exapmle, a water filled cavity with a hydrophobic interior is energetically less favourable than an imploded conformer [24]. This is why even small cryptophanes with rigid structures have been observed to implode when there is nothing to fill their cavity.

The tendency to implode depends also on solvent and cryptophane concentration, which change the enthalpic conditions for the cryptophane, but they do not vary significantly throughout the experiments with calcium and CaM. These experiments were all conducted in aq. buffer solutions with an ionic strength of 100-200 mM, 0.8% DMSO, and CrA concentrations of 2-10 µM. The samples were bubbled repeatedly with 2% xenon gas mix. Under these conditions, CrA is highly unlikely to implode. However, in the expermients with TFE and controls in pure DMSO, fundamental solvent changes are made. The CrA cavity, which has a van-der-Waals volume between 84 $Å^3$ and 95 $Å^3$, as reported by Taratula el.al. [83], could accomodate DMSO comfortably (68.75 $Å^3$, as reported in [75]). The high polarity of DMSO is probably repulsive to the hydrophobic interior of CrA, so

that DMSO probably behaves like water in this aspect.

Due to years of solid-state storage and dissolution in highly polar solvents (DMSO and water), imploded conformers of CrA may have been a possibility, but only until the sample is supplied with xenon. A structural analysis of CrA monoacid concerning that aspect was done with NMR, but there was no sign of any imploded conformer. A similar structural analysis on the high concentration CrA-peptide stocks was not done, because the minimally required concentration is at least 50µM, which most likely changes the structure significantly due to aggregation, so that the sample no longer resembles the silenced CrA-peptides at 2-10µM.

Considering that the imploded conformer for CrA was most likely not present in any experiments of this study, because the incorporation of almost any other molecule is energetically more favourable than sustaining an empty cavity, a partial incorporation of part of the attached peptide seems possible. A complete blockage of the CrA portals from outside by a small peptide chain, such as GAAK, seems rather unlikely in terms of molecule size. For the same reason, I find an initial but permanent trapping of one xenon molecule within the cavity highly unlikely. A partial incorporation of the aliphatic peptide chain on one side can be influenced and reversed by solvent changes, competing itermolecular interactions, and conformational rearrangements. On the other side, it bears the unresolved issue of how a simple aliphatic peptide chain competes with the primary guest molecule xenon. Being covalently bound within one molecule changes the dynamics in favor of the hypothesis of partial incorporation. But so many other peptides did not have that effect on CrA, albeit they were bound to it. Preliminary work before this study has shown, that an excerpt from the CaM-binding protein calcineurin does not silence the CrA attached to it. That peptide was shown to be much more helical than M13 or RS20 with CD spectroscopy. This is why I would promote partial incorporation of the peptide chain as hypothesis for future research.

4.2 Molecular Biology of the Sensor in a Hypothetical *in cellulo* Context

Introducing the cryptophane-peptide into a live cell should be straightforward, because it is a cell penetrating peptide (CPP). Its overall positive charge and secondary structure facilitate the passage through the cell membrane. The permeation of exactly these CrA and fluorescein labeled peptides into intact cells after 30 minutes of incubation has been demonstrated by Westmeyer et.al. Peptides, ubiquitously distributed in the cytoplasm of living cultured cells, were observed with fluorescence microscopy by Westmeyer et.al.

In the cytoplasm, the cryptophane-peptide competes with numerous CaM binding proteins for a few µM CaM; of which less than 1% are free and available for binding. The cytosolic protein cocktail of this study does not take into account the myriads of immobilized proteins in the organelles and on the membrane of an intact cell. Other ions, which might compete with calcium-CaM and CaM-peptide binding, like Mg^{2+}, have not been assessed here. The cytoplasmic protein cocktail of this study is a test for soluble protein based background interaction only. Fortunately, the introduction of additional binding partners for CaM into intact cells has been shown to not have an effect on the CaM motility and availability[70]. This means, in spite of harsh competition, binding to CaM should be possible for the CrA-peptide.

The combination of a small synthetic ligand with a ubiquitous cellular protein to a molecular reporter ensemble is a frequently used design for molecular reporter systems, especially for imaging contrast agents. This is why it has been chosen in this study. The basis for this sensor desgin was the very successful fluorescence biosensor GCaMP, from which the peptide was adapted. The reporting moieties (GFP and cryptophane) both report upon their structural rearrangement, which is, via proxy, caused by changes in the free calcium ion concentration.

Beyond that, however, the two biosensors are quite different: In GCaMP, all the components of the biosensor are on one molecule, which is genetically expressed by the cell. The cryptophane-peptide cannot be expressed or encoded genetically, which is why the molecule needs to be synthesized and introduced into the cell. The former is not straightforward, and the latter can become a challenge as soon as *in cellulo* studies need to go beyond the the cultured cell monolayer.

This study has shown that cryptophane has the potential to interact with membranes and micelles and reactivate xenon exchange independently of the peptide, CaM and calcium. When micelles are provided (for instance by Antifoam A), the cryptophane silencing is remediated instantly and fully; even more than by CaM-peptide binding. This suggests that interactions with the micelles must be stronger or energetically more favourable than the "silent conformation" of the cryptophane-peptide. The question if and in which intensity these interactions are relevant in living cells can only be answered experimentally.

The foreign cryptophane-peptide may encounter cellular defense mechanisms, and probably has a limited lifetime in the cytosol before it is degraded or expulsed. Eventually, the pharmacokinetics and potential toxicity of the peptides to cultured cells need to be analyzed.

In a nutshell, the molecular biology challenges for the biosensor *in cellulo* are:

- cell permeation and peptide delivery in cell cultures other than a monolayer or suspension

- competition by other calmodulin binding proteins
- lipid-rich and hydrophoic compartments, organelles or micelles.
- cellular defense and peptide degradation/expulsion
- feedback loops of calcium signalling, which the biosensor might be involved in
- toxicity and pharmacokinetics of the peptide

Most of the above mentioned limitations can be overcome once the silencing mechanism has been found out, by using a smaller and CaM-independent molecule that can alternate between conformations to either sense calcium or silence cryptophane CEST. Designing such a molecule would mean to entirely redesign the biosensor, which is beyond scope of this study.

4.3 Technical Limitations in This Study

Several physical and chemical analysis methods have been employed to complement ^{129}Xe HyperCEST NMR spectroscopy and help to elucidate the structural mechanism at the core of cryptophane CEST silencing. In particular, these are:

- Structural ^{1}H NMR
- ECD spectroscopy
- ITC
- Fluorescence Polarization

Each of these methods can only access parts of the mechanistic network, which cryptophane CEST silencing is embedded in. The differences in experimental conditions between those methods make comparisons less reliable and more complicated. All HyperCEST experiments are done under 3,5 bar overpressure and an atmosphere of 2%Xe, 88%He and 10%N2. For many aspects, this may be irrelevant, but molecular xenon incorporation, and anything else that depends on the dissolved gas, might be affected by that. Gas-tight apparatures are not available for most of these methods, and measurements are performed under air at atmospheric pressure.
The low concentration of cryptophane-peptide is a key advantage of this biosensor, but it makes the mechanism hardly accessible for other measuring techniques. The fact that the peptide is

unstructured under these conditions provides little information. Observing CrA and CrA-peptides at higher concentrations, where this untsructured conformation might be roughly characterized, can lead to aggregation phenomena, which have their own influence on the structure. Except for FP, all the methods mentioned above require concentrations over 50µM, which is already well in the aggregation range. Fluorescence Polarization provides reliable information about binding events and reactions, but not about molecular structure in this case. The molecular structure may have an influence on the autofluorescence of CrA, but this can only be measured without fluorescent moieties.

The application of the entire biosensor would be in the analysis of intracellular calcium signals, primarily for research. This can be done *in cellulo*, with cultured cells, or *in situ*, with tissue preparations.

As intracellular calcium signalling is spacially and temporally encoded, a Xenon HyperCEST MRI would need to be done with a temporal resolution between seconds and single minutes, to be able to decode any i.c. (intracellular) calcium signalling. The acquisition would need to be spatially resolved to a certain extent as well. A spatial resolution of individual cells is not attainable, but also not necessary, because tissue-wide calcium imaging has been shown to be a very useful application[2]. However, for a tissue-wide calcium analysis, a tissue simulation with cultured cells or a tissue preparation would need to be implemented. The individual cells need to be supplied with polarized xenon, nutrients, necessary ions for homeostasis, and the paramagnetic oxygen.

CrA-peptide integrates into micelles, or any compartment similar to a micelle, reactivating the cryptophane. Many such compartments are sincluded in a live cell, or even on the way to a cell in blood (which is also an emulsion). Because the integration into micelles can be mediated by cryptophane, it may not be possible to determine whether a cryptophane reactivation comes from an intracellular calcium signal or a micellar compartment. This problem may not even be solvable by molecular redesign. However, calcium signalling is temporally encoded, while the intagration into micelles is not. Given any temporal resolution, calcium signalling perhaps may be separated by its transient nature.

Xenon dissolves in blood and water only to a certain extent under normal atmospheric pressure. Xenon polarization has a certain lifespan, which depends largely on the surrounding solvent and magnetic properties. As the best way to administer xenon to a living organism is by breathing, and in any case xenon will travel in the bloodstream, it is always combined with the paramagnetic oxygen, which enhances nuclear relaxation, which leads to a shorter polarization lifetime. In such a case, the lifespan of xenon polarization is restricted to these conditions, and consequently,

so is the time that xenon has to reach the cryptophane at the target site AND experience the saturation pulse. Whenever *in vivo* experiments are planned, the xenon solubility in blood/water at atmospheric pressure and the lifespan of xenon polarization in the given bloodstream are hard limitations that must be considered. The callenge of any *in vivo* xenon MRI is to get the xenon to the target site before the polarization is lost. The speed of this transport is ultimately limited to the blood flow of the specimen or patient.
As a summary, the technical limitations in application of the biosensor and cryptophane silencing are:

- a necessary temporal resolution of seconds to minutes
- the xenon solubility in blood and tissue
- the polarization lifetime in blood and tissue
- fixed-bed solutions for tissue simulation, or tissue preparations , which need to be implemented for hyperCEST to conduct *in-situ* experiments

For *in situ* and *in vivo* calcium sensing with xenon HyperCEST NMR, further development of xenon biosensors, and the delivery of xenon and biosensor molecules, as well as signal acquisition techniques is necessary.

5 Summary, Conclusion and Outlook

5.1 Summary

This study began in pursuit of the development of a calcium-CaM sensitive biosensor for xenon HyperCEST NMR. It was focused on the characterization of reversible cryptophane CEST silencing mediated by short peptides. Several possible causes for cryptophane CEST were excluded experimentally, and the search for the mechanism is now more constrained. The limitations of the calcium-CaM-peptide biosensor were discussed, and future investigations can be done on much smaller molecules in simpler samples. The main findings of this study are:

1. The ability of cryptophane to exchange xenon can be silenced selectively by an attached peptide.

2. Cryptophane CEST silencing can be reversed by allowing the peptide to bind Holo-CaM. Modulations of CaM or calcium concentration directly affect cryptophane silencing.

3. The CaM-mediated silencing is a dynamic response, meaning it changes instantly and flexibly with the concentration of Holo-CaM, in both directions.

4. A quantification of the response's sensitive range to between 0.2 and 1.0 equivalents of calcium per CaM was possible. Equivalent concentrations of CrA-peptide and CaM were sufficient to remediate cryptophane CEST silencing. A peptide concentration of 2 µM was the lowest concentration, with which the response was recorded. This corresponds to a sensitive range of 0.4 - 2 µM calcium This reflects the concentration range of intracellular calcium signaling, and the sensitivity of current calcium imaging techniques.

5. Cryptophane CEST silencing can also be reversed by a change of solvent to TFE or DMSO, or by the presence of micelles.

After the phenomenon of cryptophane silencing has been confirmed and initially quantified, cryptophane silencing has been analyzed from a few possible angles. An investigation by HyperCEST

is almost without alternative, because of the very limited accessibility of the mechanism at micromolar concentrations. Several mechanisms have been excluded as cause, some previously published concepts[64,95] could not be confirmed, but the one mechanism that causes chryptophane silencing could not be determined yet. However, this study has shown that all it takes to silence cryptophane at such low concentrations is four rather arbitrary amino acids. Additionally it was shown, that no specific secondary structure is needed for that, and that the ability to silence cryptophane is neither a question of length or sequence of the peptide. This makes the search for a defined mechanism more concise, and guides it into a direction of small-molecule structural analysis and spectroscopy.

5.2 Conclusion and Outlook

The elucidation of cryptophane silencing has become the final and central aspect of this study and is the objective for future investigations on this topic. Using the smallest possible molecule for the elucidation of the mechanism comes with the advantage of being able to avoid aggregation at higher concentrations, and thereby being able to use more structure analysis methods. A concise mechanism within this molecule might be applicable with larger molecules, or even different molecular systems, but this is not necessarily the case. Applications probably require a well planned modification and simplification of the biosensor for biocompatibility and efficiency, for which an exact knowledge of the mechanism is essential. Any generalization or translation onto other molecular host/guest systems also requires a well defined mechanism. After this study, the scientific goal of selectively silencing chemical exchange in host/guest systems has become more palpable, but the challenge of elucidating the exact mechanism remains.

Future studies are required to pursue the elucidation of the chemical mechanism behind cryptophane silencing. A partial encapsulation of the molecule itself, much like the self-insertion described by Baydoun in[9], becomes more likely than initially proposed. A molecular dynamics modeling approach might reveal unknown experimental paths to follow for future analysis. Cryptophane - xenon interactions in water have been modeled and are described in[40] and[53]. An MD simulation of a 20-residue peptide has become quite feasible over the last seven years. The development of a new generation of force fields, an increase in computational power by hardware development, a move from local to cloud computing, and an increased number of projects dedicated to peptide and polypeptide structure simulation raise hope for that field[21]. However, the MD simulation of cryptophane-bearing peptides is still a project beyond the scope and the discipline of this study.

The latest and rather surprising result was that even the shortest peptide in this study, K(CrA)GAA,

is able to silence cryptophane. An MD simulation thereof appears tempting at first. However, in this scenario, the re-activation of the CEST response by CaM or Antifoam A is not accessible, simply because the interaction of the tripeptide with calmodulin or antifoam A is completely unknown. It cannot be expected to resemble the longer peptides, so deductions from the experiments with longer peptides cannot be made. That said, an MD simulation of a longer, CaM binding CrA bearing peptide is presumably the better starting project for future investigations.

Experiments with cells have been considered, but not pursued in this project, because a redesign of the biosensor was considered as necessary, to avoid interactions with lipid-rich structures and micelles. However, a few investigations may be of advantage without an elucidation of the mechanism. To enhance the biosensor's visibility, overexpressing CaM seems compelling. However, overexpression of solvated, active CaM is limited by how much extra signal transduction the cell can handle before initiating apoptosis. This also depends on the cell type. Incubating lysed cell material with immobilized cryptophane-peptide immobilized on a column, and a subsequent elution, also seems compelling. It could be useful to detect how much CaM is in the cell to bind the sensor peptide. Furthermore it could be useful to see if anything else from the cell binds the sensor peptide, and competes against CaM. But in an intact live cell, the peptide would have a certain mobility, which cannot be considered when it's fixed onto a column. Moreover, lysed cell material lacks the cytosolic structure and orgaization, which may engage in unforeseen interactions (or prevent them), and needs additional protease inactivation agents. Lastly, experiments with immobilized live cells would be the most desireable perspective.

In [45], Kunth et. al. describe a method to determine exchange rates from realxivity measurements. This could be used on the fully assembled and active biosensor. The surface of CaM needs to be taken into account, because xenon may adhere to it, albeit this does not visibly or directly influence HyperCEST measurements. However, that does not mean xenon does not interact with calmodulin at all. There might be interactions with the protein surface, which may modulate the relaxivity of xenon in the solution pool. Kunth's method of determining an exchange rate using the temperature-related relaxivity, described in [45], could be used to analyze this. This includes that the surface of calmodulin, in each of its different conformations, must be considered as potential interaction partner for xenon and measured individually. The peptide, especially in its unstructured state in solution, does not provide a concise surface for xenon to adhere to and experience significant changes in relaxivity or chemical shift.

Knowing that cryptophane silencing is possible with a much smaller and simpler molecule than anticipated at the beginning of this study, future projects have the opportunity of using higher

concentrations of the smallest cryptophane silencing molecule and different spectroscopy methods for structure elucidation of the silenced complex. The structure can reveal key facts about the silencing mechanism, which has the potential to change the use of cryptophanes substantially.

6 Materials and Methods

6.1 Calmodulin

6.1.1 Calmodulin from External Sources

CaM was at first purchased at Medicago BV, and Sigma, as lyophilized powder. It was extracted from bovine testes and purified using LC. Its molecular size and purity was confirmed by the manufacturers by gel chromatography and LC. However, the folding and binding activity have not been verified and may have been deteriorated by lyophilization. The suppliers state an enzymatic activity of the re-dissolved CaM between 1 week (sigma- aldrich) and several months (medicago), depending on the supplier. After different observations of CaM activity loss over time, a continuous quality of CaM, independent of purchase and delivery times, was pursued. Cloning and heterologous expression of CaM was done, and solubility and binding to the target of this study was verified.

6.1.2 Cloning

The plasmid pKK233-hCaM, carrying the hCaM1 gene, was purchased from Addgene. Plasmid pKK233-hCaM is shown below, in fig.6.1. Plasmid maps were generated with Benchling.
The plasmid pKK233-hCaM was delivered as a bacterial stab culture, from which it was streaked on LB (Lysogeny Broth)-Agar with 100µg/ml Ampicillin for selection of single colonies. The LB recipe can be found in the Manual for the pET system, pg.16.
200ml LB + 100µg/ml was inoculated with a single colony and shaken at 180 rpm and 37℃over night. Glycerol stocks were produced from this culture by putting 500µl of the overnight culture in a screw cap tube and adding 500µl 50% Glycerol, mixing thoroughly, and placing the stock at -80℃.
The insert for the expression vector carrying the hCaM gene was amplified from the plasmid pKK233-hCaM1 by PCR, using the KOD hot start polymerase (novagen).
The PCR product was verified by agarose gel electrophoresis with EtBr (Supplies were purchased from BioRad, and BioRad Protocols were used), and purified from the semi-preprative gel and the

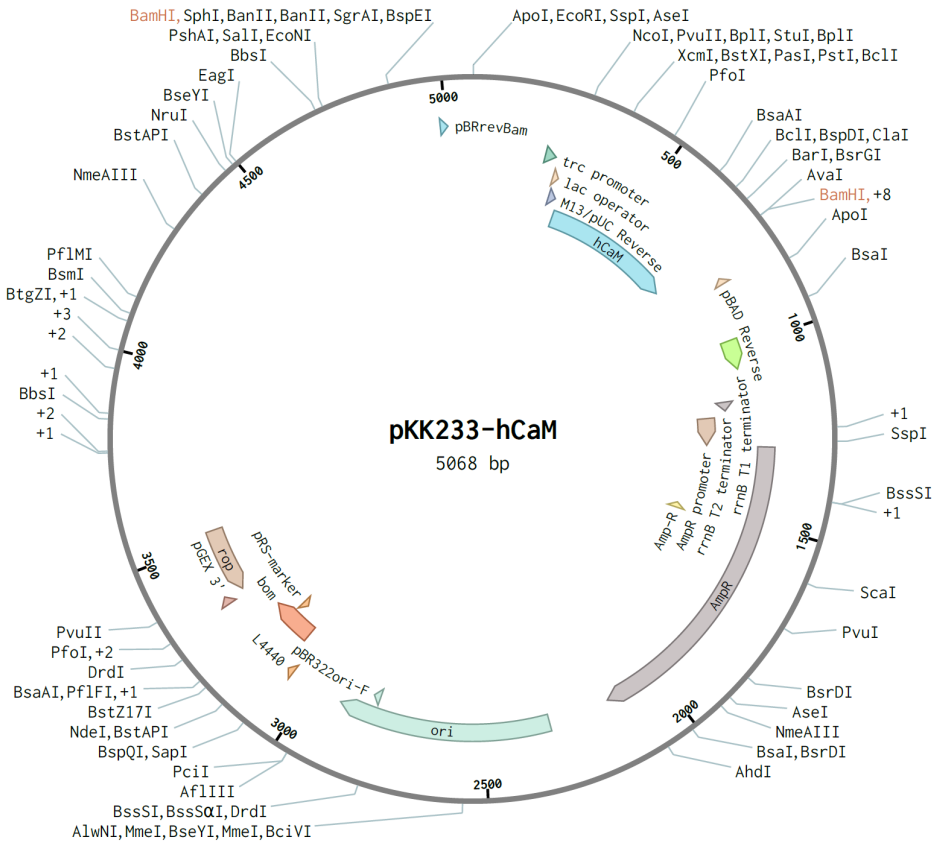

Figure 6.1: The Plasmid pkk233hCaM.

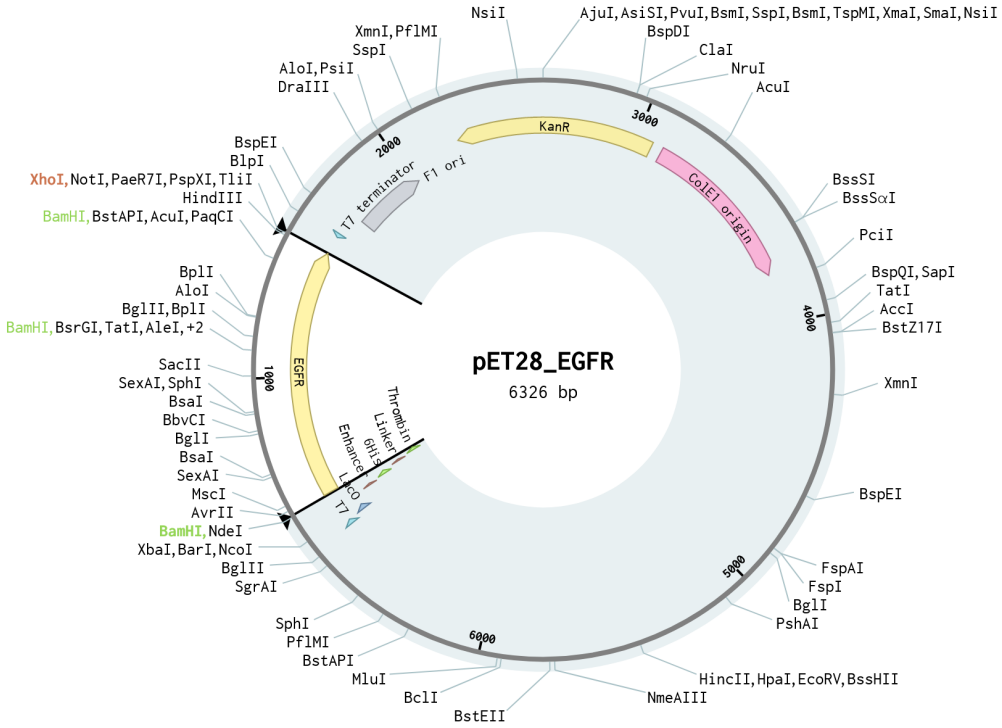

Figure 6.2: The Plasmid pET28a-EGFR.

remaining PCR mix, using the HiYield miniprep Kit (Südlabor), according to the manufacturer's protocol.

Plasmid pET28a-EGFR was modified by enzymatic restriction with enzymes BamH1 and XhoI, as indicated in the plasmid map (fig. 6.2). The region highlighted in the map , mainly comprised of the pET28a plasmid vector, was used as expression vector for the hCaM1 gene. The enzymatic digestion was conducted on both the vector and the insert, to produce the compatible sticky ends. The manufacturer's protocol for 50 µl total reaction volume was used for this: 1 µg DNA to be cut, 2µl of each enzyme, 5µl cutSmart Buffer, fill up with DNAse free MilliQ Water to 50µl, 1h at 37°C, inactivation at 65°C for 5 min.

Name	Length	sequence (5'-3')	$T_{m\text{-initial}}$ °C	$T_{m\text{-final}}$°C
pKK-CaM-for	24	aggaaaggatccatggctgaccag	38.0	66.9
pKK-CaM-rev	24	cccgggctcgagtcactttgcagt	34.0	70.4
T7 promotor	20	TAATACGACTCACTATAGGG	-	46.8
T7 terminator	19	GCTAGTTATTGCTCAGCGG	-	52.9

Table 6.1: Primers used for cloning

Name	restriction site
BamH1	5'-G'GATCC-3'
Xho1	5'-C'TCGAG-3'

Table 6.2: Restriction enzymes used in this study, with binding site. The enzymes were purchased from New England Biolabs.

List of primers:

List of restriction enzymes:

The restrictions were verified on a 2% agarose gel with EtBr, along with the controls. The DNA fragments to be ligated were cut and purified from the gel, using the HiYield Kit (südlabor), according to protocol. The purified DNA unfortunately was of low concentration and the insert additionally had a high salt content. Yet it was ligated using T4 Ligase (NEB), according to the supplier's protocol for the reaction volume of 20 µl:

The ligation resulted in the new expression plasmid pET28a-hCaM (fig. 6.3). After ligation, the plasmid was resalted, using a MicroBioSpin P-30 Tris Cromatography column (BioRad), to aid the transfection by electroporation. The *recA*$^-$ non-expression host strain E.coli XL1Blue was transfected with pET28a-hCaM for decent transfection efficiency, as the pET manual recommends for initial cloning.

The colonies were rescued in SOB (Super-Optimal Broth) medium after electroporation and selected on LB-Agar with 35µg/ml Kanamycin. The correct ligation was verified by colony PCR (primers: T7 promotor, T7 terminator, see table 6.1), according to the pET vector manual, section III.C, pg. 22. The size of the PCR product from the correct insertion/ligation is 701bp. It was verified on a 2% agarose gel with EtBr. Because of the sticky ends, a reversed insertion was highly unlikely. Also, as the next step was a preliminary expression, there was no interest in a check for the right orientation of the insert.

Single colonies with the correct plasmid were inoculated and cultivated, each single colony in 50ml LB with 35 µg/ml Kanamycin and 100µg/ml Ampicillin, in 250ml flasks in an shaker incubator (infors HT), at 37°C and 180 rpm, until OD reached 0.6-0.8. The plasmid was extracted and

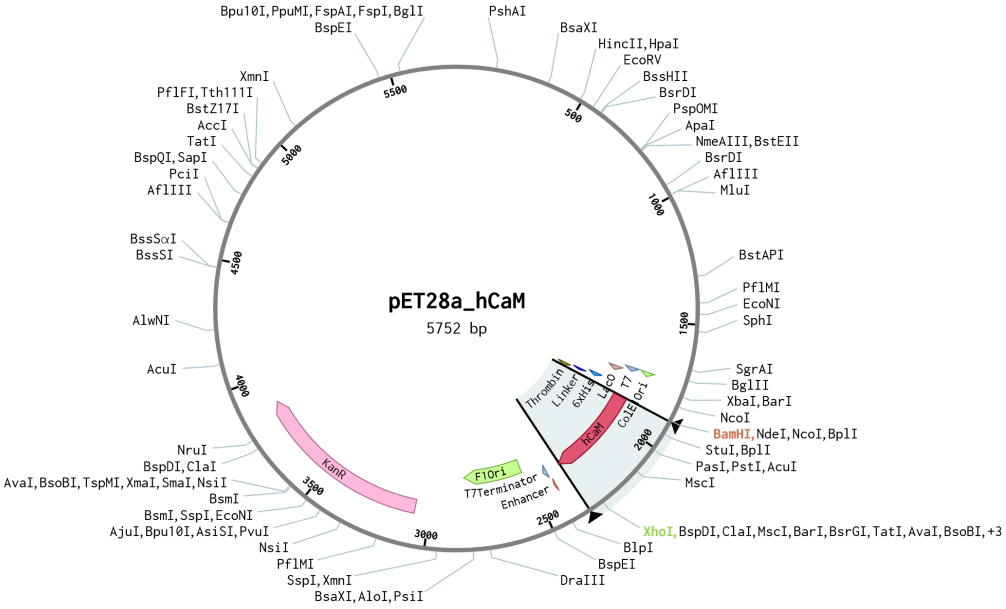

Figure 6.3: The Plasmid pET28a-hCaM.

purified by chromatography, using the GeneJet Midiprep spin column kit (thermofisher) according to the supplier's protocol. It was strored at -20°C, and a small amount transformed into the E.coli expression strain BL21 by electroporation, as previously described.
Cloning advice and Background information is provided in the pET Vector manual.

6.1.3 Protein Expression and Purification

Figure 6.4 provides an overview of the expression and purification.
The strain BL21(DE3) was used as expression strain. The strain is resistant against T1 phages. It contains the necessary genes for the widely used IPTG induction and T7 expression. The Lon and OmpT proteases are deficient in this strain, to prevent instant protein degradation.
The cultivation was conducted as follows:

1. Preculture: - Inoculation: 1ml (2%) Glycerol Stock in 50ml LB + 35µg/ml Kanamycin (50µl -> 1:1000 from Stock)
   - Preculture 37°C over night.

2. Growth: -Inoculation: 50ml (10%) preculture in 450ml LB+ 105µg/ml Kanamycin (1,5ml -> 1:333,33 from Stock)
   - Cultivate at 37°C until optical density (OD) between 0.5 and 1 (5h:30min)

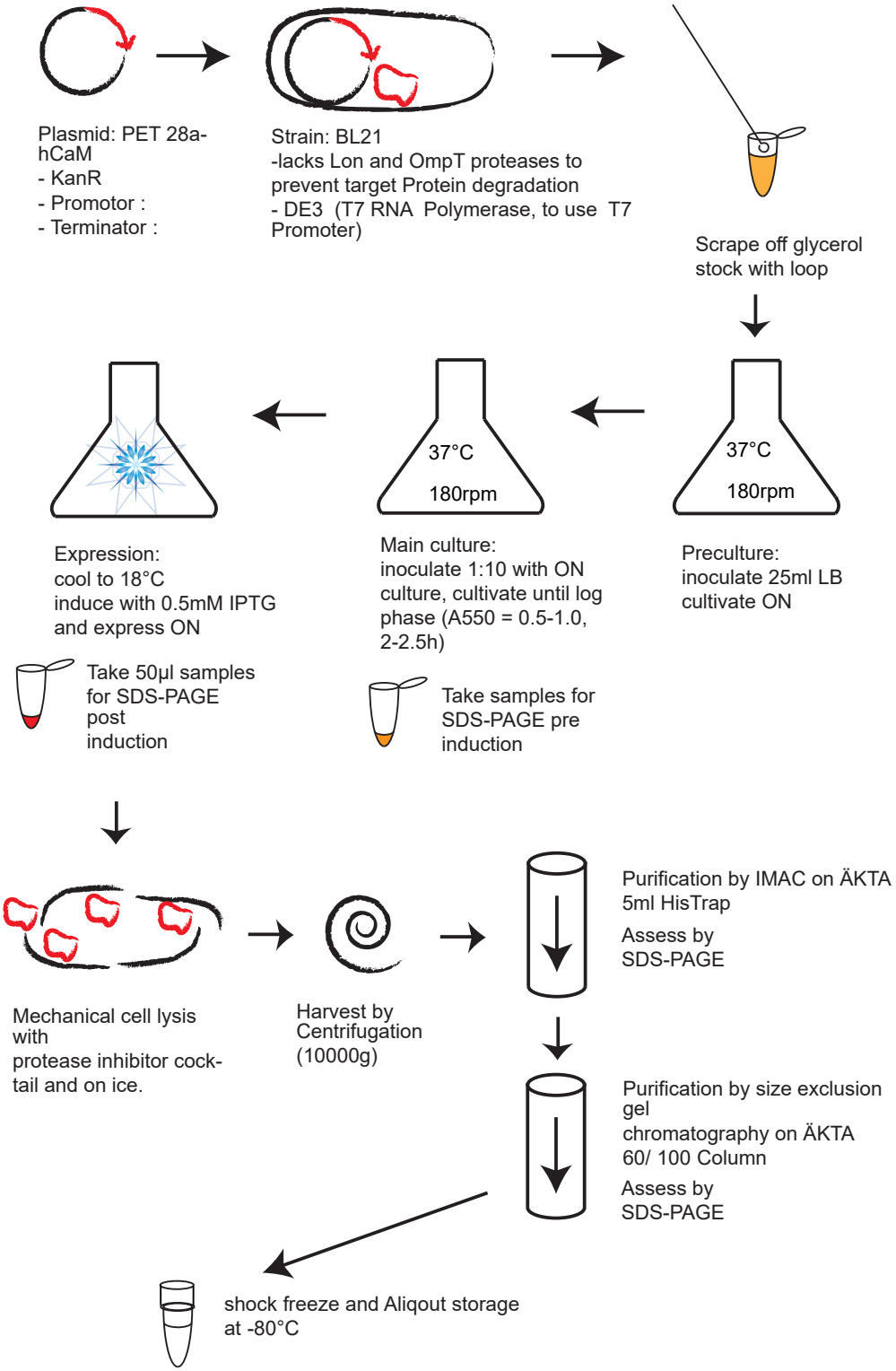

Figure 6.4: Overview of the expression and purification workflow of hCaM from the expression.

- Take Samples for OD monitoring and SDS gel (pre- induction and post induction, supernatant and pellet of 1 ml each)
- SDS Buffer (BioRad website): 25mM Tris, 192mM Glycerol, 0.1%SDS, pH 8.3

3. Induction: - Cool culture on ice and cool down incubator to 18°C
   - Add IPTG: 500µl (to 500ml culture) of 1M Stock –> 1mM

4. Expression: Cultivate over night (16h) at 18°C.

The cultivation was stopped by cooling on ice. All subsequent steps were done on ice or with equivalent cooling. Cells were disrupted with ultrasound and sheer forces, as previously mentioned. The cell disruption was performed in a pH buffered protease inhibitor cocktail. The cell debris was removed by centrifugation at 10000g. The purification was done according to this protocol:

1. Harvest: Centrifuge at 4000g for 15min at 4°C , keep on ice, resuspend in ice cold Lysis Buffer.
   Lysis Buffer:
   0.02 M PBS + 5mM DTT + 1 Tablet cOMplete EDTA free
   PBS (Phosphate Buffered Saline): 0.5 M Na2HPO4 and 0.5M NaH2PO4 are titrated to yield pH 7.4, diluted 1:5 in water, and 0.5M (29,22g/L) NaCl is added before use.

2. Lysis: Pretreatment with ultrasound probe, then mechanical lysis with microfluidizer, 5-6 cycles, 1 additional wash with PBS.

3. Purification:
   Pretreatment:
   The cell lysate was centrifuged at 10000g to remove cell debris. The supernatant was rescued carefully and filtrated, using vivaspin columns (GE healthcare, now cytiva), to remove smaller compounds, especially proteins and peptides.
   Affinity chromatography:
   Fast pressurized liquid chromatography (FPLC) using an ÄKTA System, with a HiTrap Ni-NTA 5ml column (GE healthcare, now Cytiva). The clear and filtrated cell lysate was loaded onto the column by the ÄKTA, and given time for protein binding. The buffer for all following steps was PBS with 0.01M imidazole. The column was washed several times before elution.

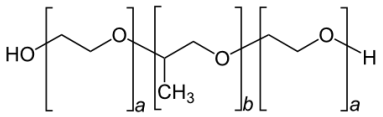

Figure 6.5: The generic form of a block copolymer, or poloxamer, of which pluronic L-81 is one. The properties of block copolymers depend largely on the chain length and branching.

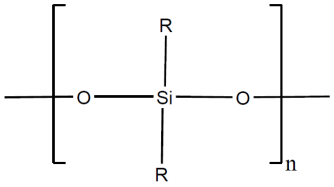

Figure 6.6: The basic structural unit of a polysiloxane (also known as silicone). Antifoam is such an active silicone polymer. The properties of silicone polymers depend almost entirely on their length and branching.

Elution was done with imidazole, running a gradient from 0.01M to 0.5M imidazole.

Size exclusion chromatography (SEC):

Equilibrated previously with MOPS Buffer (30mM MOPS, 100mM KCl, 1.3 mM $CaCl_2$, pH 7.2)

The products of most steps were verified by SDS-PAGE. The final purified hCaM was assessed by extinction measurement and Bradford's assay with an external standard (Bovine Serum Albumin). The final product was shock frozen and stored at -80°Cas stocks with a volume of and a concentration of 250 µM. These stocks were used for the preparation of samples.

6.2 Antifoam

As protein containing aqueous solutions tend to foam strongly, when bubbled with gas, an antifoam agent is essential for Xenon NMR with CaM. The surface tension reducing block copolymer Pluronic L-81 (Sigma-Aldrich) has been used in Xenon NMR before, without notable interference. An amount of 0.3 vol.-% Pluronic was used in each sample that contained Calmodulin. The basic structure of the block copolymer that pluronic consists of is shown in fig.**??**. The idea was to change the antifoam agent in order to rule out any interference of pluronic with the cryptophane silencing. Pluronic was replaced by Antifoam A (Sigma-Aldrich), a polysiloxane. The basic structure of a polysiloxane is shown in fig. **??**. As shown in the results, antifoam A surprisingly remediated cryptophane silencing. An amount of 0.3 vol.-% of antifoam A was used for each sample. Each one

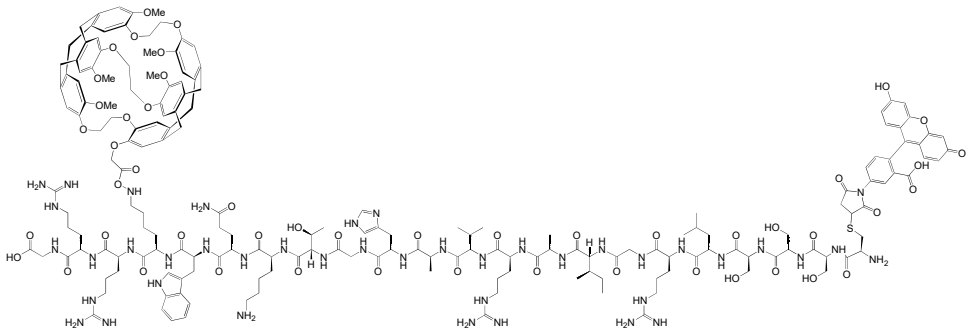

RS20

GRRK-(Cr-A)-WQKTGHAVRAIGRLSSS-C(5-Fluo-M)-amid

Figure 6.7: The peptide RS20 in full length, with Cryptophane and Fluorescein-5-Maleimide functional groups.

of these two antifoaming agents was added to the buffer, and the sample was mixed vigorously, to distribute the high viscosity fluids well and benefit from their effect.

6.3 Cryptophane - Peptides

The cryptophane used in this study was exclusively cryptophane-A monoacid, as described in the introduction. The cryptophane was weighed and redissolved from lyophilized powder in DMSO at a concentration of 500µM. Weighing cryptophane powder must be done with care, as it is electrostatic. The concentration was later confirmed by HPLC. The DMSO stock solution was stored at -20℃. The cryptophane peptides for this study are schematically depicted below, to have a view of the sequence and functional groups and their positions in the molecule. The peptide RS20 (fig.6.7) is a representation of the autoinhibitory and CaM binding region of smooth muscle myosin light chain kinase.

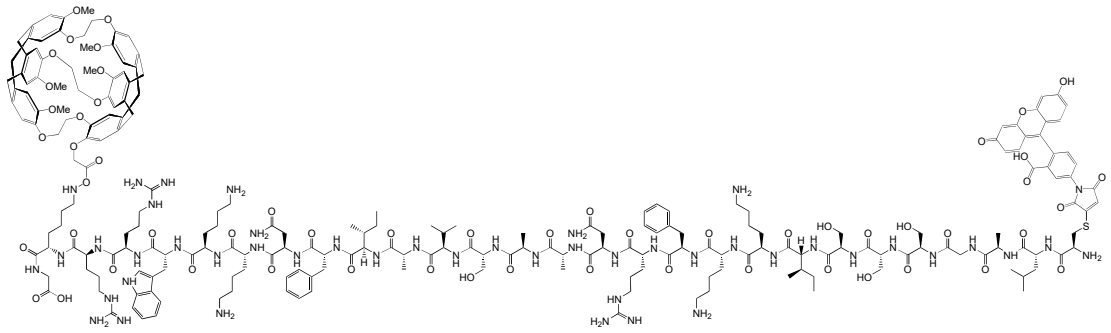

M13

G-K(Cr-A)-RRWKKNFIA-VSAANRFKKISSSGAL-C(5-Fluo-M)-amid

Figure 6.8: The peptide M13 in full length, with Cryptophane and Fluorescein-5-Maleimide functional groups.

The peptide M13 (fig.6.8) is another CaM binding site, derived from skeletal muscle myosin light chain kinase. M13 is also an autoihibitory region, which suppresses the CaM-stimulated myosin light chain kinase activity and so prevents muscle contraction.

To address the questions discussed earlier about interactions between cryptophane A and certain amino acid residues, the residues in question were exchanged by alanine (A) residues. First, the tryptophan (W) residue nearest to the cryptophane was exchanged, as shown in fig.6.9.

Then, the arginine (R) residues in cryptophane's close vicinity were substituted by alanine (A), as shown in fig. 6.10.

To rule out the N-terminal part of the peptide as cause for cryptophane silencing, RS20 was truncated in the middle, see fig.6.11. Note that the shorter peptides from hereon were made without a fluorescent tag, because they were not meant for any binding or microscopy assays, and only for analysis with (Xenon) NMR.

All of the aforementioned peptides were synthesized by biosyntan GmbH. The smallest peptides,

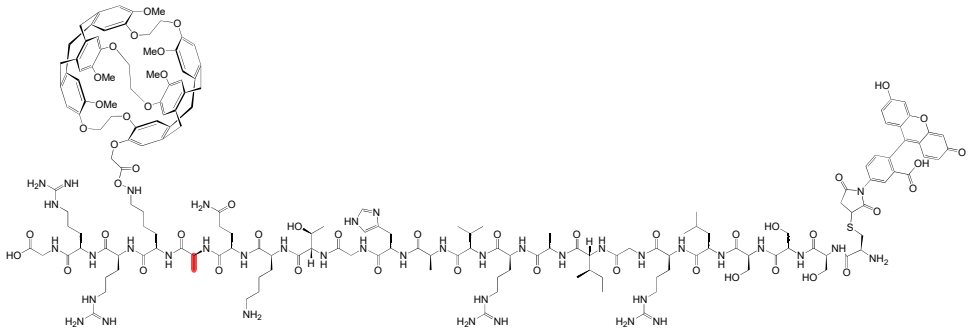

RS20-W

GRRK-(Cr-A)-AQKTGHAVRAIGRLSSS-C(5-Fluo-M)-amid

Figure 6.9: The peptide RS20 in full length, with Cryptophane and Fluorescein-5-Maleimide functional groups, with an alanine substitution at W5.

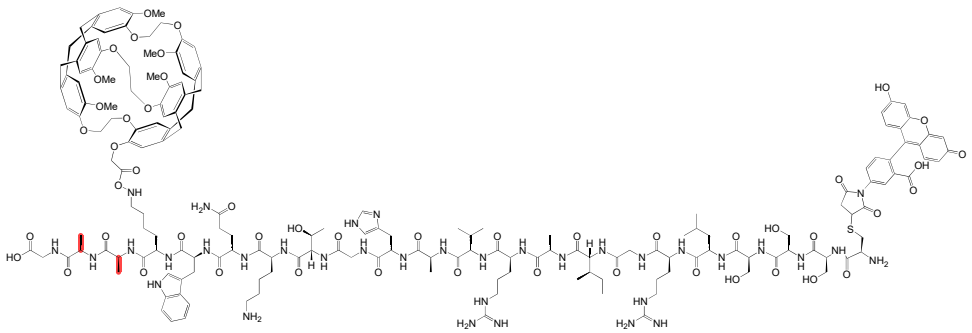

RS20-RR

GAAK-(Cr-A)-WQKTGHAVRAIGRLSSS-C(5-Fluo-M)-amid

Figure 6.10: The peptide RS20 in full length, with Cryptophane and Fluorescein-5-Maleimide functional groups, with two alanine substitutions at R2 and R3.

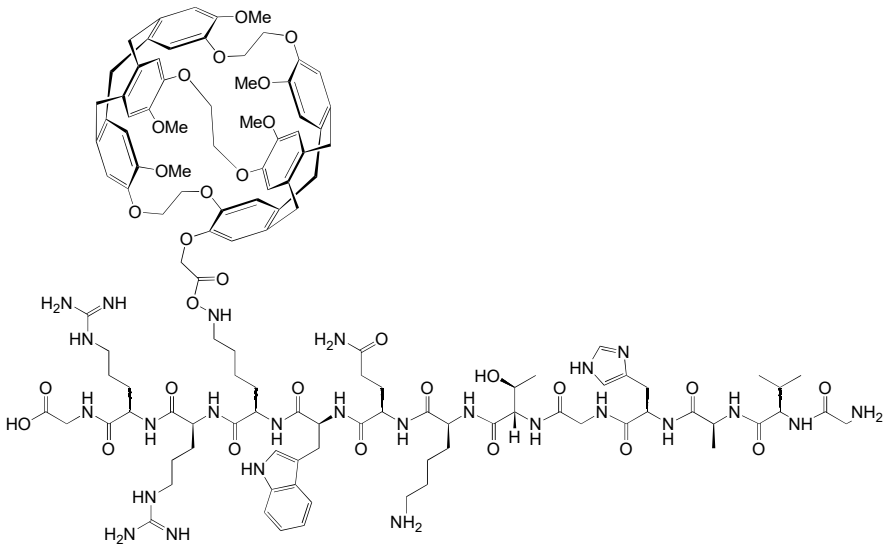

Figure 6.11: The C-terminal half of peptide RS20, with Cryptophane as functional group.

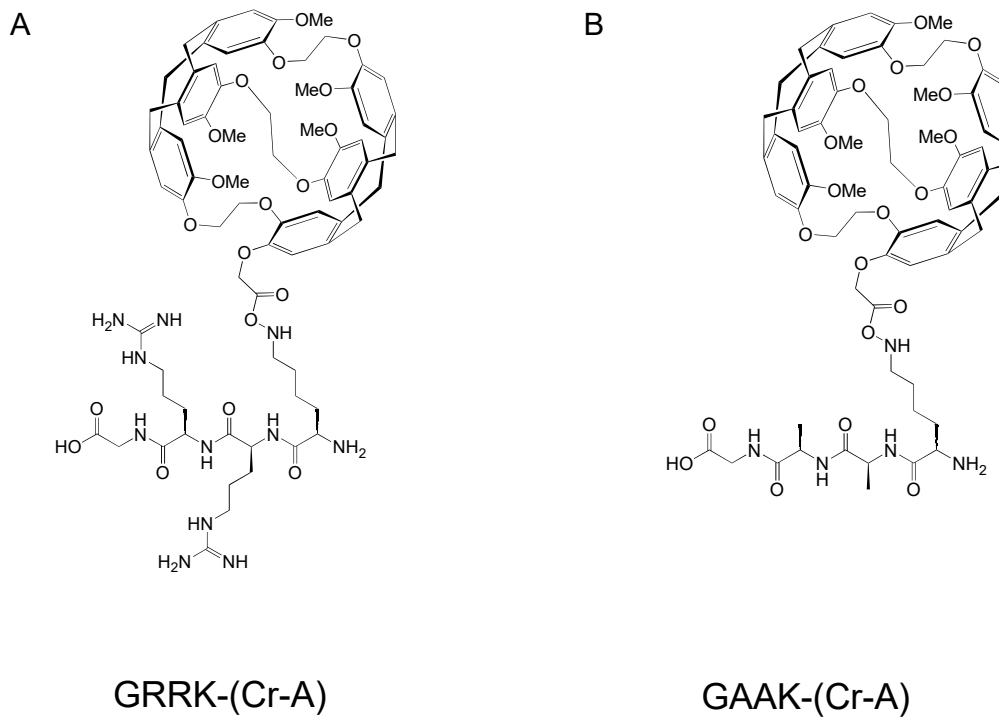

Figure 6.12: The peptides GRRK-CrA and GAAK-CrA.

shown below in fig.6.12, were synthesized in our lab, by Dr. J.O.Jost, and the correct synthesis and purification was confirmed with HPLC.

The peptide containing just the C-terminal side with the cryptophane of the original RS20 was sythesized in two versions: with two arginines (fig.6.12A) and with two alanines (fig.6.12B) instead.

6.4 Calcium Buffering

To provide exactly the desired amount of calcium ions in solution at all times during the experiment, calcium buffering was used. The Calcium Calibration Buffer Kit Nr. 1 (ThermoFisher) was used for this. The buffering system in this kit is based on an triangular equilibrium between calcium, its chelator, and an inferior competitor ion (K^+). The exact function and preparation of an equal calcium buffering system is described in [11]. The purchased buffer Kit used here consists of two solutions: 10mM Ca EGTA and 10mM K_2 EGTA. The two solutions were mixed in different ratios to yield the desired concentration of free calcium ions. This concentration can be set between zero and 39 µM free calcium, using the calculation example from the Kit's Manual, or the calcu-

lations described by Bers et.al[11]. The calculations need be adjusted to the working conditions, in this order: temperature, ionic strength, pH. This is essential to obtain the desired free calcium concentration.

6.5 Xenon HyperCEST NMR

6.5.1 NMR Equipment and Hyperpolarization Apparatus

Pressurized liquid gases (He, N_2 and ^{129}Xe) in Bottles are purchased from Air Liquide and Linde. He serves a s filling gas, N_2 serves as buffer for heat dissipation in the polarization process. The gas mix used in this study was: 10% He, 88%N_2 and 2%^{129}Xe. The gas bottles were connected to the gas mixing station with pressure regulators and stainless steel tubing. The custom built gas mixing station consists of steel tubing and connectors, the latter serve as mixing chambers. Pressure regulators at the entrance regulate the gas influx. The pressure regulators are operated with a user interface, which is based on DASYLab13. The gas composition that leaves the mixing station can be set via the incoming gas flows. The tubing, connectors, fittings and valves are purchased from swagelok(NL).The gas mix is transported to the polarizer through stainless steel piping (swagelok). Quarter-turn valves (swagelok) mark the entrance to the polarizer. The Leipnix polarizer was built by Schroeder et.al. and is described in[74]. It is a network of perfluoroalkoxy (PFA) and stainless steel tubing and connectors (Swagelok), through which the gas is guided by pressure and flow regulators. The gas mix is transported through the polarization chamber and ultimately to the sample. The polarizer also operates the chamber, sustaining the right conditions for stable and continuous xenon polarization. Xenon is hyperpolarized in the chamber by spin exchange optical pumping (SEOP). figure 6.13 B , reprinted from ref.[74], outlines the basic process of SEOP: In the initial step, circularly polarized light is produced, in order to deliver the appropriate photons to a cloud of alkali metal vapour. In the Leipnix polarizer, rubidium is the alkali metal of choice. Maintaining the right conditions around this cloud is essential for the polarization efficiency, but not quite straightforward. These conditions and the technical details for maintaining them are explained briefly and concisely in ref[74], and in detail in ref.[86]. The second step is achieving rubidium electron polarization with LASER irradiation in the rubidium cloud, whilst maintaining the aforementioned conditions. In the third and final step, the electron polarization is transferred from rubidium onto xenon as nuclear spin polarization by flip-flop processes during collisions of rubidium and xenon atoms. The gas mix with the polarized xenon is continuously transported to the sample in the phantom through PFA tubing. The entire system is under 3.5 bar overpressure.

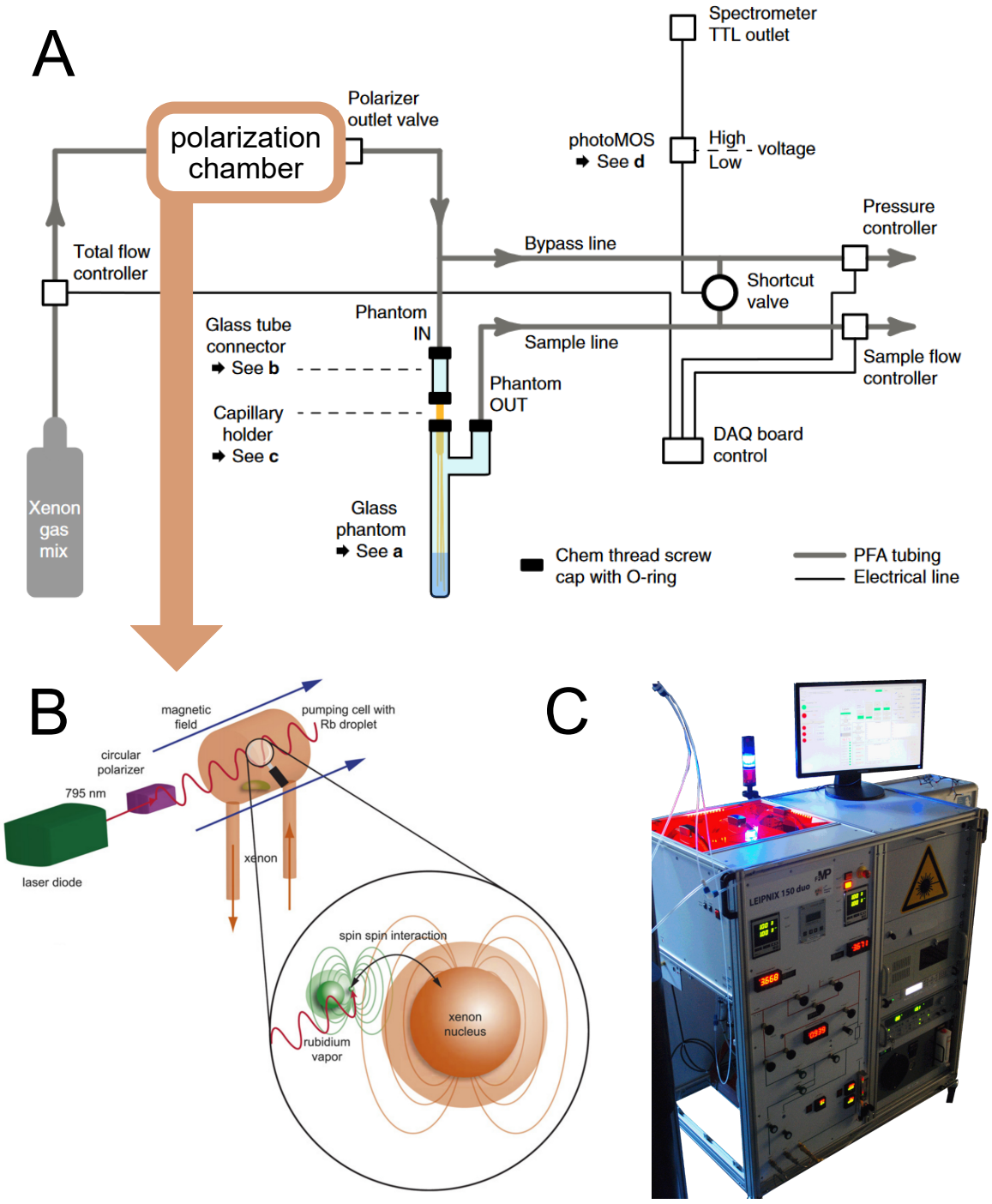

Figure 6.13: A: Polarizer flow scheme and structure, reprinted with permission from ref. [49].
B: Scheme of SEOP, adapted from ref. [74].
C: Photograph of the Leipnix polarizer.

The sample is provided semi-continuously with HP-^{129}Xe by bubbling through glass capillaries (polymicro). To sample the Xe@solution signal correctly and without artifacts from gas bubbles, it must be acquired in intervals between xenon deliveries. Those intervals and the deliveries are set with the DASYLAB13 based user interface. As the polarization is destroyed with every saturation pulse, new HP-^{129}Xe is administered after each saturation pulse, so that the Xe@solution signal is reconstituted. The phantom is a 10mm NMR tube with a bypass fused to its upper shaft. Both ends can be closed air tight with screw caps. The bypass functions as an exit for the gas, while the top of the tube is an entrance for gas. Five fused silica glass capillaries (diameter 0.25 mm, polymicro) transport the gas through the septum and into the liquid sample on the bottom of the tube. From there, gas bubbles travel up through the sample, exchanging with the liquid sample across the bubble surface. Depending on the sample, foam may form in the head-space of the tube and deteriorate the Xe@solution signal or generate a gaseous Xe signal, or both. After bubbling, the sample is enriched with dissolved gas xenon. As soon as all bubbles are collapsed (a time delay is set in the user interface), this can be measured. The Spectrometer is an AV-400 from Bruker, with a magnetic field strength of 9.4T, and a center frequency of 400MHz, respectively. The strong magnetic field is provided by a superconducting coil, which is cooled by vessels of liquid Helium and Nitrogen, concentrically surrounding it. It has a 25 mm bore, into which a 10mm RF coil is inserted for the experiments of this study. The coil is a dual-channel coil, with one channel for proton and another for xenon measurements. The coil emits radio frequency (RF) pulses and measures free induction decay (FID). A typical measurement of a Z -spectrum in this study is set up as follows: The sample is connected to the PFA tubing, placed inside the magnet bore and pressurized carefully. Polarizer boot-up is done carefully, stable temperatures in the polarization chamber are ensured. The temperature in the center needs to be highest, and the temperature in the front needs to be lowest to ensure the right position of the Rb cloud. Meanwhile, the coils are adjusted, using a predefined standard shim procedure in topspin or Paravision. The Xe coil is tuned, which is called wobbling. The Xe@solution signal is measured with direct Xe spectroscopy, using topspin (for details, see the topspin manual). This initial signal is documented for maintenance. Occasionally, the position of the phantom is observed by acquiring an ^{1}H MR image, using ParaVision (for details, see the ParaVision manual). In case of foaming or positioning issues, the sample needs to be removed from the magnet and re-positioned. Shimming and wobbling need to be repeated. The temperature of the sample should be constant throughout the measurement. The Xe@solution signal is set as center frequency for the Z spectrum. The frequency list is set, as well as the receiver gain, number of averages per acquisition, bubbling times and intervals, saturation pulse length and

duration. All these parameters are set using the ParaVision interface. After setting the parameters, the Z spectrum can be acquired, frequency by frequency.

6.5.2 Software

- The polarizer was run using DASYLab13 with a code written by several members of the group. This script also coordinates the spectrometer activities, e.g. saturation pulse, with the polarizer activities, e.g. bubbling times and intervals.
- The spectrometer is operated using topspin and ParaVision 6.1 and 4 (Bruker). The Data acquisition was done with topspin.
- The visualization of the data was done with a python code written using Ipython notebook/JuPyter. Later, a comprehensive GUI (graphical user interface) was built based on this code by Dr.P.Schünke, which was used for all later data visualizations, also HP-Xe MR images.
- For all biophysical analyses, the pre-installed software of the device manufacturer was used for data acquisition. Data was visualized using OriginLab and Excel.

6.5.3 Sample Preparation Material for Xenon Hyper CEST NMR

The Samples for Xenon NMR were prepared of the components described earlier and listed below, in 2.0 mL eppendorf tubes.

- Buffer Solution
- Calmodulin from concentrated stock solution (250 µM)
- Cryptophane-peptide from concentrated stock solution (500 µM)
- Pluronic (antifoaming agent, 0.1 vol.-%)

After thorough mixing of all components, 1.5 mL were transferred into the glass phantom for NMR. The phantom (fig. 6.14) is made of thick-walled NMR glass tubes (Wilmad) with 10mm outer diameter, fused to two screw capped ends: a supply and a bypass, as shown in fig. 6.14.
The screw caps conntect the glass construction with the PFA tubing, through which the gas mix is supplied. The top screw cap has inside a capillary holder, which is a plastic piece pierced with five coated fused silica glass capillaries (Polymicro/molex), through which the xenon gas mix is

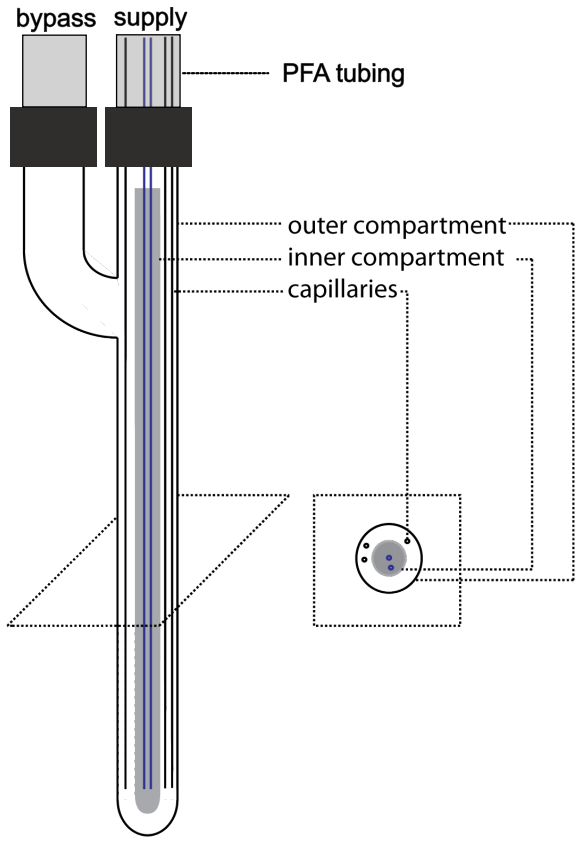

Figure 6.14: The modified NMR tube called the phantom. With an 5mm NMR tube inserted, it is a 2-compartment phantom.

supplied. As the entire polarizer is under 3.5 bar overpressure, the phantom also must be gas tight, and able to withstand this pressure, including occasional sudden pressure drops and surges.

To extend the construction to a two-compartment phantom, a smaller (0.5cm outer diameter) NMR glass tube (Wilmad) is inserted into the phantom, as shown in grey in fig. 6.14. Two capillaries are inserted in the inner compartment.

The setup is also described by Kunth and Doepfert[44] in the supplementary figure S2, and in the dissertation of Kunth[43], in Figure 4.2 on pg. 77. A very similar setup is also neatly described by lakshmanan[49].

6.6 Biophysical Measurements

6.6.1 Dynamic Light Scattering

Dynamic Light Scattering (DLS) is used to measure the size of molecules via the influence of their motion on their light scattering pattern across time. This analysis is also known as Photon Correlation Spectroscopy(PCS). When a monodisperse (with only one kind of molecule or nanoparticle) sample is illuminated, light is scattered. All particles in the sample refract light in all directions. The scattered light forms a pattern of dark (destructive interference) and light (constructive interference) speckles. The intensity of each speckle over time reveals information about the molecular movement by way the light is scattered. The correlation between the initial state and the state after a time delay depends on the molecular (predominantly brownian) movement, whose close relation to the molecular size is described by the Stokes-Einstein equation. Dynamic light scattering spectra were measured with a Zetasizer nano ZS device (Malvern). Data was collected and processed with the manufacturer's software, uses inbuilt algorithms to extract an intensity distribution from the correlation data. Samples were prepared in aqueous solution, and homogenized previous to measurement. The sample contained 100µM of each fluorescent peptide (M13-CrA and RS20-CrA) in deionized water, 2 vol.-% DMSO. It was made in an 1,5mL eppendorf tube and the small amount needed was transferred directly into a low volume glass cuvette (hellma), which was placed in the Zetasizer with the appropriate spacers, into a fixed position. Expecting micelle formation, a pre-established standard operating protocol(SOP) for micelle forming molecules was used: SOP Mizellen kleine Kuevette 1x5 wdh.sop. Blank measurements were conducted with pure water. The measurements on the Zetasizer were carried out following the Zetasizer Manual, pg. 4-2.

6.6.2 Cirular Dichroism

To measure circular dichroism, a substance needs to be optically active. Optical activity is the ability of a substance to rotate the plane of plane polarized light. This property can be used to deduce many properties and structural features of a molecule. Light as an electromagnetic wave contains electrical and magnetic field components, that vibrate perpendicularly to the propagation of the light beam [36]. When light is plane polarized, the vibrations are restricted to a plane. When it is circularly polarized, the vibrational plane is rotating, and the rotation can proceed in either direction. There is a difference between the extinction (expressed by the molar extinction coefficient ϵ) of left-rotating and right-rotating circularly polarized light in an optically active sample, which transforms circularly polarized light into elliptically polarized light, when it passes through the sample. The difference in extinction, $\delta\epsilon$ and the ellipticity θ express this difference, and can be easily interconverted: $\theta = 3.298\delta\epsilon$. When either of these expressions is graphically plotted over the wavelength, a CD spectrum is obtained.
Circular dichroism spectroscopy was performed using a J-720 Spectrometer (Jasco). Samples were prepared in clear polypropylene cuvettes with 1cm path length. The following parameters were preset using the Software Spectra Manager 1.54H (Jasco):

- wavelength range: 185-260 nm
- scanning mode: continuous
- scanning speed: 100 nm/min
- response time: 1 s
- bandwidth: 1 nm
- accumulations: 25

The peptide concentration was 50µM, and the samples were made in different solvent mixes: water with 20% Trifluoroethanol (TFE, Sigma-Aldrich), water with 50% TFE and pure water. The use of a buffer is arbitrary here, because this experiment is about one aspect of the peptide secondary structure, which is not influenced by the buffer. This one aspect is the overall helicity.
The deconvolution of the CD spectrum and the helicity were calculated using an Excel sheet by Dr. S. Klippel with macros after the method of Brahms & Brahms [12].

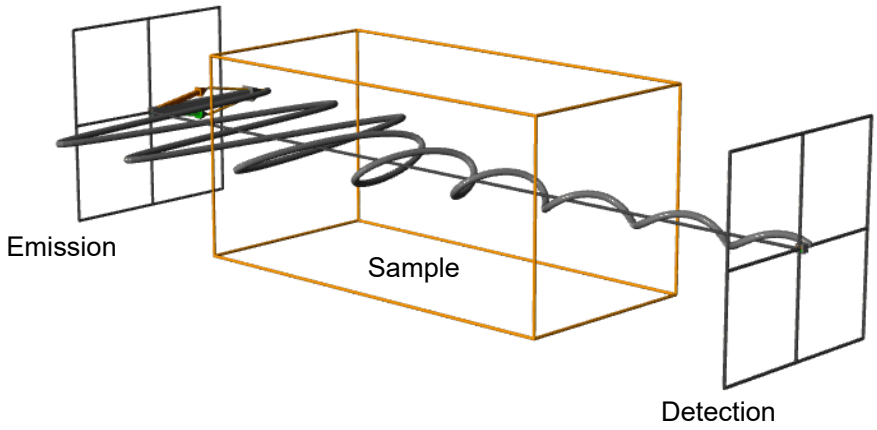

Figure 6.15: The superposition of circularly polarized light in left and right rotation is plane polarized light. Because of the difference in extinction between left and right rotation, this is transformed into elliptically polarized light across the sample. This effect is used as CD (circular dichroism) to measure molecule size.

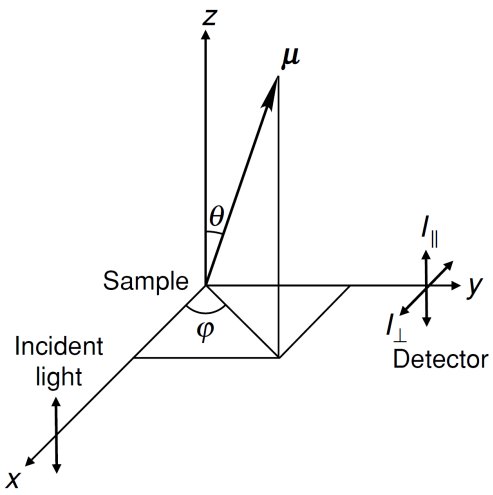

Figure 6.16: The incident plane polarized light, which excites the fluorophore, travels along the x-axis and is spolarized along the z-axis. In the sample, the excited fluorophore undergoes a rotation, so that at the time of emission, the emitting transition dipole μ will differ from the absorbing one by the angles θ and ϕ. The emission behind the sample is measured by the detector in two components: $I_{\parallel}$ and $I_{\perp}$, with respect to the incident beam. Figure reprinted with permission from Serdyuk et al.[76]. Copyright: Cambridge University Press.

6.6.3 Fluorescence Polarization

Fluorescence polarization (FP) was used to detect the molecular weight difference between two molecules: a fluorescent probe and a non-fluorescent macromolecule bound to the probe. The fluorophore in the probe can be excited by a photon at the excitation wavelength. The temporary rearrangement of its electrons (excitation) is reversed by the emission of a photon. Note, that polarization is, as always, a ratio, and thus dimensionless. When polarized light is used for the excitation, the polarization is partly transmitted onto the emitted photon. How much polarization is transmitted onto the photon, depends on how much rotation the fluorophore undergoes during the fluorescence lifetime. When the sample is illuminated with a beam of plane-polarized exciting light, it travels along the x-axis, polarised with the electric vector along the z-axis. The emitted light is measured by two detectors in two components: $I_{\parallel}$ and $I_{\perp}$. The setup is depicted in fig. 6.16.

The measured polarization is calculated from the two components $I_{\parallel}$ and $I_{\perp}$:

$$P = \frac{I_{\parallel} - I_{\perp}}{I_{\parallel} + I_{\perp}}$$

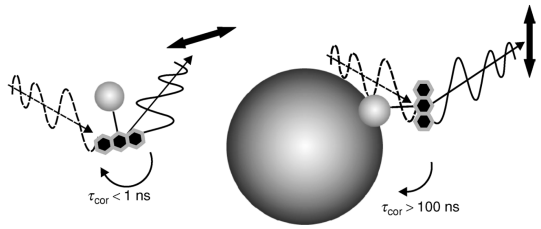

Figure 6.17: A free fluorescent probe (left) rotates much faster (at a sub-nanosecond frequency) than when it is bound to a macromolecule (right). The measure for this is the rotational correlation time τ_{cor}. The τ_{cor} of the free probe is so small, the polarization of light is averaged and compensated by the rotation and lost. A large enough macromolecule, firmly bound to the probe, slows down the rotation, so that polarization can be retained. Figure reprinted with permission from Serdyuk et al. [76]. Copyright: Cambridge University Press.

Polarization is another expression of anisotropy, and thus a dimensionless ratio. It is often given in mP, even by the devices and software used in this project, but the unit is arbitrary. In practice, a correction factor G is introduced during measurement, to account for the sensitivity differences in the detector system between the two different directions.

$$P = \frac{I_{\parallel} - GI_{\perp}}{I_{\parallel} + GI_{\perp}}$$

The correction factor G should be close to 1.

The polarization of the emitted photon depends on the angle (θ) between the absorbing and emitting transition dipoles of the fluorophore [68]. The angle θ, which is depicted in fig. 6.16 depends on the fluorophore's molecular motion. Small molecules are constantly in rapid brownian motion, while larger molecules experience slower molecular tumbling. Molecular movement can be approximated by describing it as a kind of averaged rotation, schematically shown in 6.17. The measure for this is the rotational correlation time τ_{cor}. For very small τ_{cor}, the polarization is lost, because the molecule's orientation is completely random at the time of fluorescence emission due to so many rotations. For very large τ_{cor}, the molecule will not experience any notable rotation within the fluorescence lifetime. Most biologically relevant molecules are between these extremes [76]. So, firmly bound to a biological macromolecule, the probe will experience a much smaller rotation on average, so that polarization can be retained.

The connection between the measured polarization and the molecular movement is made using the Perrin equation, which shows the dependence of the anisotropy $r(\tau_F)$ on the fluorescence lifetime τ_F and the rotational correlation time τ_{cor}:

$$r(\tau_F) = \frac{r_0}{1+\frac{\tau_F}{\tau_{cor}}}$$

The dependence on the orientation of the molecule via θ is within r_0, the intrinsic anisotropy of the molecule without movement:

$$r_0 = \frac{3cos^2\theta-1}{5}$$

Fluorescence polarization and anisotropy describe the same phenomenon, and can be easily interconverted , as described in [48]. The fluorescence polarization for rigid molecules is:

$$P_0 = \frac{3cos^2\theta-1}{cos^2\theta+3}$$

Steady state polarization, which is the assay used in this project, requires constant Illumination with exciting light. When the rotational correlation time τ_{cor} is practically infinite, because the system is rigid, P equals P_0. For molecules that are actually moving, the steady state polarization, derived from the Perrin equations, is:

$$P = \frac{3}{1+10(1+\frac{\tau_F}{\tau_{cor}})(3cos^2\theta-1)^{-1}}$$

In this study, the FP measurements were conducted with a Tecan GENiosPro microplate reader, and data was collected with the magellan software. 120µl of each sample were prepared in 1,5ml Eppendorf tubes and then distributed into triplicates of 30µl each in black, round-bottom 348-microwell plates (Corning, type 4514) with non-binding surface. All measurements were conducted at ambient temperature. A fluorophore concentration of 100nM was used for all experiments. This optimal concentration was determined before. The G factor was recalibrated for each measurement. The fluorescence detector gain was set to 60 for all experiments. The sample compositions of the different experiments are listed below:

1. Titration with CaM:

   The buffer was 30mM MOPS, 100mM KCl, pH 7.2, and either 10mM EGTA or 10mM $CaCl_2$. Both buffers were supplemented with 100nM fluorescein-5-A- maleimide- labelled RS20-CrA. A dilution row from a CaM stock solution (250µM) was made once in each buffer. The following CaM concentrations were used for FP samples: 10000, 1000, 100, 10, 1, 0.1, 0.01nM. Controls without fluorophore and without CaM were made as well. Each sample was mixed thoroughly by vortexing and distributed into triplicates of 30 µl on the microwell plate.

2. Titration with Calcium:

The buffer was from the calcium calibration kit No.1 (ThermoFisher,C3008MP), with the components: 30mM MOPS, 100mM KCl, pH 7.2, and 10mM either CaEGTA (calcium saturated) or K_2EGTA (calcium depleted). Ample supply of the two components for all samples were supplemented with 100nM fluorescein-5-A- maleimide- labelled RS20-CrA and 100nM (0.1 µM) CaM. The two buffer components were used as extreme ends of the titration. Mixtures of the two components were made to yield the following buffered free calcium concentrations: 0.1, 0.226, 0.602, 1.355, 1.731, 2.358, 3.612, 4.866, 7.375, 14.9, and 39 µM (calcium saturated buffer).

Controls were: calcium saturated buffer with fluorophore only and without fluorophore, calcium depleted buffer with fluorophore only and without fluorophore. Each sample was mixed thoroughly by vortexing and distributed into triplicates on the microwell plate.

3. Test for aggregation: Samples were made in specially treated eppendorf tubes, with a non binding surface, because the compounds are micelle-forming. It was observed via fluorescence that all petides, es pecially the micelle forming ones, adhere to the walls of the tubes, and less adhesion is observed for non binding surfaces. The concentrations were: 100nM fluorescent p2fa2, and 10000, 5000, 2000, 1000, 100, 10, 1, 0.1 nM p2a2. Controls were: buffer only, buffer with 100nM p2fa2.

Excel and Origin 2020 were used for further Data processing and visualization. The measured FP

$$P = \frac{I_{\parallel} - GI_{\perp}}{I_{\parallel} + GI_{\perp}}$$

Was plotted over

1. the peptide/CaM ratio
2. the Ca/CaM ratio
3. the ratio between fluorescent and non-fluorescent molecules

on a logarithmic (base 10) scale. A sigmoidal function was fitted to the Data wherever possible. The sigmoidal transition is indicative for binding. The point of inflection marks the ratio of binding partners, at which the binding reaction is the fastest. The amount and quality of the Data did not allow any further or more concise deductions.

Bibliography

[1] Julie A. Aaron, Jennifer M. Chambers, Kevin M. Jude, Luigi Di Costanzo, Ivan J. Dmochowski, and David W. Christianson. Structure of a ^{129}Xe-Cryptophane Biosensor Complexed with Human Carbonic Anhydrase II. *Journal of the American Chemical Society*, 130(22):6942–6943, June 2008.

[2] Misha B. Ahrens, Michael B. Orger, Drew N. Robson, Jennifer M. Li, and Philipp J. Keller. Whole-brain functional imaging at cellular resolution using light-sheet microscopy. *Nat Meth*, 10(5):413–420, May 2013.

[3] Jasper Akerboom, Jonathan D. Vélez Rivera, María M. Rodríguez Guilbe, Elisa C. Alfaro Malavé, Hector H. Hernandez, Lin Tian, S. Andrew Hires, Jonathan S. Marvin, Loren L. Looger, and Eric R. Schreiter. Crystal structures of the GCaMP calcium sensor reveal the mechanism of fluorescence signal change and aid rational design. *J. Biol. Chem.*, 284(10):6455–6464, March 2009.

[4] Tatjana Atanasijevic, Maxim Shusteff, Peter Fam, and Alan Jasanoff. Calcium-sensitive MRI contrast agents based on superparamagnetic iron oxide nanoparticles and calmodulin. 103(40):14707–14712, October 2006.

[5] Y. S. Babu, C. E. Bugg, and W. J. Cook. Structure of calmodulin refined at 2.2 A resolution. *J Mol Biol*, 204(1):191–204, November 1988.

[6] I. C. Bagchi, B. E. Kemp, and A. R. Means. Myosin light chain kinase structure function analysis using bacterial expression. *J. Biol. Chem.*, 264(27):15843–15849, September 1989. Publisher: American Society for Biochemistry and Molecular Biology.

[7] Kristin Bartik, Michel Luhmer, Jean-Pierre Dutasta, André Collet, and Jacques Reisse. ^{129}Xe and ^{1}H NMR Study of the Reversible Trapping of Xenon by Cryptophane-A in Organic Solution. *Journal of the American Chemical Society*, 120(4):784–791, February 1998.

[8] Kristin Bartik, Michel Luhmer, Stephen J. Heyes, Robert Ottinger, and Jacques Reisse. Probing Molecular Cavities in α-Cyclodextrin Solutions by Xenon NMR. *Journal of Magnetic Resonance, Series B*, 109(2):164–168, November 1995.

[9] Orsola Baydoun. *Dually Functionalized Cryptophane-[223] Derivatives : Elaboration of Hydrosoluble 129-Xe Biosensors and Chiroptical Aspects*. These de doctorat, Lyon, November 2019.

[10] Manu Ben-Johny and David T. Yue. Calmodulin regulation (calmodulation) of voltage-gated calcium channels. *J Gen Physiol*, 143(6):679–692, June 2014.

[11] Donald M Bers, Chris W Patton, and Richard Nuccitelli. A practical guide to the preparation of Ca(2+) buffers. *Methods Cell Biol*, 99:1–26, January 2010.

[12] S. Brahms and J. Brahms. Determination of protein secondary structure in solution by vacuum ultraviolet circular dichroism. *Journal of Molecular Biology*, 138(2):149–178, April 1980.

[13] Marisa Brini, Tito Calì, Denis Ottolini, and Ernesto Carafoli. Intracellular Calcium Homeostasis and Signaling. In Lucia Banci, editor, *Metallomics and the Cell*, Metal Ions in Life Sciences, pages 119–168. Springer Netherlands, Dordrecht, 2013.

[14] Thierry Brotin and Jean-Pierre Dutasta. Cryptophanes and Their Complexes - Present and Future. *Chemical Reviews*, 109(1):88–130, January 2009.

[15] Thierry Brotin, Anne Lesage, Lyndon Emsley, and André Collet. ^{129}Xe NMR Spectroscopy of Deuterium-Labeled Cryptophane-A Xenon Complexes: Investigation of Host-Guest Complexation Dynamics. *Journal of the American Chemical Society*, 122(6):1171–1174, February 2000.

[16] Jennifer M. Chambers, P. Aru Hill, Julie A. Aaron, Zhaohui Han, David W. Christianson, Nicholas N. Kuzma, and Ivan J. Dmochowski. Cryptophane Xenon-129 Nuclear Magnetic Resonance Biosensors Targeting Human Carbonic Anhydrase. *Journal of the American Chemical Society*, 131(2):563–569, January 2009.

[17] Xiao-Jie Cheng, Li-Li Liang, Kai Chen, Ning-Ning Ji, Xin Xiao, Jian-Xin Zhang, Yun-Qian Zhang, Sai-Feng Xue, Qian-Jiang Zhu, Xin-Long Ni, and Zhu Tao. Twisted Cucurbit[14]uril. *Angewandte Chemie*, 125(28):7393–7396, 2013. _eprint: https://onlinelibrary.wiley.com/doi/pdf/10.1002/ange.201210267.

[18] André Collet. Cyclotriveratrylenes and cryptophanes. *Tetrahedron*, 43(24):5725–5759, January 1987.

[19] Robert Allen Copeland. *Enzymes: a practical introduction to structure, mechanism, and data analysis*. Wiley-VCH, Chichester (UK), 2002. OCLC: 819159531.

[20] Magali Darzac, Thierry Brotin, Denis Bouchu, and Jean-Pierre Dutasta. Cryptophanols, new versatile compounds for the synthesis of functionalized cryptophanes and polycryptophanes. *Chemical Communications*, 0(1):48–49, 2002.

[21] Xavier Daura. Molecular Dynamics Simulation of Peptide Folding. *Theor Chem Acc*, 116(1):297–306, August 2006.

[22] Luigi Di Costanzo and Silvano Geremia. Atomic Details of Carbon-Based Nanomolecules Interacting with Proteins. *Molecules*, 25(15):3555, January 2020. Number: 15 Publisher: Multidisciplinary Digital Publishing Institute.

[23] Petra Ehling, Stefan Bittner, Thomas Budde, Heinz Wiendl, and Sven G. Meuth. Ion channels in autoimmune neurodegeneration. *FEBS Letters*, 585(23):3836–3842, December 2011.

[24] G. El-Ayle and K. Travis Holman. Cryptophanes. In *Comprehensive Supramolecular Chemistry II*, pages 199–249. Elsevier, 2017.

[25] Joel A. Finbloom, Clancy C. Slack, Carson J. Bruns, Keunhong Jeong, David E. Wemmer, Alexander Pines, and Matthew B. Francis. Rotaxane-mediated suppression and activation of cucurbit[6]uril for molecular detection by ^{129}Xe hyperCEST NMR. *Chemical Communications*, 52(15):3119–3122, February 2016.

[26] G. Fiorin, A. Pastore, P. Carloni, and M. Parrinello. Using Metadynamics to Understand the Mechanism of Calmodulin/Target Recognition at Atomic Detail. *Biophysical Journal*, 91(8):2768–2777, October 2006. Publisher: Elsevier.

[27] D. P. Fitzsimons, B. P. Herring, J. T. Stull, and P. J. Gallagher. Identification of basic residues involved in activation and calmodulin binding of rabbit smooth muscle myosin light chain kinase. *J. Biol. Chem.*, 267(33):23903–23909, November 1992. Publisher: American Society for Biochemistry and Molecular Biology.

[28] Giuseppe Gambino, Tanja Gambino, Rolf Pohmann, and Goran Angelovski. A ratiometric 19F MR-based method for the quantification of Ca2+ using responsive paramagnetic probes. *Chem. Commun.*, 56(24):3492–3495, March 2020. Publisher: The Royal Society of Chemistry.

[29] Serhat Gündüz, Nobuhiro Nitta, Sandip Vibhute, Sayaka Shibata, Martin E. Mayer, Nikos K. Logothetis, Ichio Aoki, and Goran Angelovski. Dendrimeric calcium-responsive MRI contrast agents with slow in vivo diffusion. *Chem. Commun.*, 51(14):2782–2785, 2015.

[30] Jacques Haiech, Emilie Audran, Marie Fève, Raoul Ranjeva, and Marie-Claude Kilhoffer. Revisiting intracellular calcium signaling semantics. *Biochimie*, 93(12):2029–2037, December 2011.

[31] Archibald Hill. PROCEEDINGS OF THE PHYSIOLOGICAL SOCIETY: January 22, 1910. *The Journal of Physiology*, 40(suppl):i–vii, 1910. _eprint: https://onlinelibrary.wiley.com/doi/pdf/10.1113/jphysiol.1910.sp001386.

[32] P. Aru Hill, Qian Wei, Roderic G. Eckenhoff, and Ivan J. Dmochowski. Thermodynamics of Xenon Binding to Cryptophane in Water and Human Plasma. *Journal of the American Chemical Society*, 129(30):9262–9263, August 2007.

[33] Christian Hilty, Thomas J. Lowery, David E. Wemmer, and Alexander Pines. Spectrally Resolved Magnetic Resonance Imaging of a Xenon Biosensor. *Angewandte Chemie International Edition*, 45(1):70–73, 2006.

[34] Mitsuhiko Ikura, G. Marius Clore, Angela M. Gronenborn, Guang Zhu, Claude B. Klee, and Ad Bax. Solution Structure of a Calmodulin-Target Peptide Complex by Multidimensional NMR. *Science*, 256(5057):632–638, 1992.

[35] J. M. Imparl, T. Senshu, and D. J. Graves. Studies of calcineurin-calmodulin interaction: probing the role of arginine residues using peptidylarginine deiminase. *Arch Biochem Biophys*, 318(2):370–377, April 1995.

[36] Jasco. Principles of CD/ORD (1): Principles of Circular Dichroism and Optical Rotatory Dispersion | JASCO Global, February 2022.

[37] Jabadurai Jayapaul and Leif Schröder. Molecular Sensing with Host Systems for Hyperpolarized 129Xe. *Molecules*, 25(20):4627, January 2020. Number: 20 Publisher: Multidisciplinary Digital Publishing Institute.

[38] Garry K. Seward, Yubin Bai, Najat S. Khan, and Ivan J. Dmochowski. Cell -compatible, integrin-targeted cryptophane-129Xe NMR biosensors. *Chemical Science*, 2(6):1103–1110, 2011.

[39] Najat S. Khan, Brittany A. Riggle, Garry K. Seward, Yubin Bai, and Ivan J. Dmochowski. Cryptophane-Folate Biosensor for ^{129} Xe NMR. *Bioconjugate Chemistry*, 26(1):101–109, January 2015.

[40] Paul D. Kirchhoff, Jean-Pierre Dutasta, André Collet, and J. Andrew McCammon. Dynamic and Rotational Analysis of Cryptophane Host - Guest Systems: Challenges of Describing Molecular Recognition. *Journal of the American Chemical Society*, 121(2):381–390, January 1999.

[41] Stefan Klippel, Christian Freund, and Leif Schröder. Multichannel MRI Labeling of Mammalian Cells by Switchable Nanocarriers for Hyperpolarized Xenon. *Nano Lett.*, 14(10):5721–5726, October 2014. Publisher: American Chemical Society.

[42] Naoko Kotera, Nawal Tassali, Estelle Léonce, Céline Boutin, Patrick Berthault, Thierry Brotin, Jean-Pierre Dutasta, Léa Delacour, Ténin Traoré, David-Alexandre Buisson, Frédéric Taran, Sylvie Coudert, and Bernard Rousseau. A Sensitive Zinc-Activated ^{129}Xe MRI Probe. *Angewandte Chemie International Edition*, 51(17):4100–4103, April 2012.

[43] Martin Kunth. *Characterization and Optimization of Saturation Transfer NMR with Exchanging Xenon in Different Host-Guest Systems.* PhD thesis, 2016. Accepted: 2018-06-07T21:08:02Z.

[44] Martin Kunth, Jörg Döpfert, Christopher Witte, Federica Rossella, and Leif Schröder. Optimized Use of Reversible Binding for Fast and Selective NMR Localization of Caged Xenon. *Angewandte Chemie International Edition*, 51(33):8217–8220, 2012. _eprint: https://onlinelibrary.wiley.com/doi/pdf/10.1002/anie.201202481.

[45] Martin Kunth and Leif Schröder. Binding site exchange kinetics revealed through efficient spin–spin dephasing of hyperpolarized ^{129} Xe. *Chemical Science*, 2021.

[46] Ilya Kuprov. Undergraduate Magnetic Resonance, June 2020.

[47] M.P. Kurnellas, K.C. Donahue, and S. Elkabes. Mechanisms of neuronal damage in multiple sclerosis and its animal models: role of calcium pumps and exchangers. *Biochem Soc Trans*, 35(Pt 5):923–926, November 2007.

[48] Joseph R. Lakowicz. *Principles of Fluorescence Spectroscopy [electronic resource] / by Joseph R. Lakowicz.* Springer US, New York, NY, 3rd ed. 2006. edition, 2006.

[49] Anupama Lakshmanan, George J. Lu, Arash Farhadi, Suchita P. Nety, Martin Kunth, Audrey Lee-Gosselin, David Maresca, Raymond W. Bourdeau, Melissa Yin, Judy Yan, Christopher Witte, Dina Malounda, F. Stuart Foster, Leif Schröder, and Mikhail G. Shapiro. Preparation of biogenic gas vesicle nanostructures for use as contrast agents for ultrasound and MRI. *Nat Protoc*, 12(10):2050–2080, October 2017. Bandiera_abtest: a Cg_type: Nature Research Journals Number: 10 Primary_atype: Protocols Publisher: Nature Publishing Group Subject_term: Genetic engineering;Magnetic resonance imaging;Nanoparticle synthesis;Nanostructures;Ultrasound Subject_term_id: genetic-engineering;magnetic-resonance-imaging;nanoparticle-synthesis;nanostructures;ultrasound.

[50] Jae Wook Lee, S. Samal, N. Selvapalam, Hee-Joon Kim, and Kimoon Kim. Cucurbituril homologues and derivatives: new opportunities in supramolecular chemistry. *Acc Chem Res*, 36(8):621–630, August 2003.

[51] Wen-hong Li, Scott E. Fraser, and Thomas J. Meade. A Calcium-Sensitive Magnetic Resonance Imaging Contrast Agent. *J. Am. Chem. Soc.*, 121(6):1413–1414, February 1999. Publisher: American Chemical Society.

[52] Alisa Litan and Sigrid A. Langhans. Cancer as a channelopathy: ion channels and pumps in tumor development and progression. *Front Cell Neurosci*, 9, March 2015.

[53] Wenhao Liu. Molecular Dynamics Simulation Study of Water-Soluble Cryptophane Binding a Variety Guest Objects. *Dissertations available from ProQuest*, pages 1–115, January 2017.

[54] Michel Luhmer, Boyd M. Goodson, Yi-Qiao Song, David D. Laws, Lana Kaiser, Michelle C. Cyrier, and Alexander Pines. Study of Xenon Binding in Cryptophane-A Using Laser-Induced NMR Polarization Enhancement. *Journal of the American Chemical Society*, 121(14):3502–3512, April 1999.

[55] W. E. Meador, A. R. Means, and F. A. Quiocho. Target enzyme recognition by calmodulin: 2.4 A structure of a calmodulin-peptide complex. *Science*, 257(5074):1251–1255, August 1992.

[56] Thomas Meersmann and Eike Brunner. *Hyperpolarized Xenon-129 Magnetic Resonance: Concepts, Production, Techniques and Applications.* Royal Society of Chemistry, April 2015.

[57] Tyler Meldrum, Kristen L. Seim, Vikram S. Bajaj, Krishnan K. Palaniappan, Wesley Wu, Matthew B. Francis, David E. Wemmer, and Alexander Pines. A Xenon-Based Molecular Sensor Assembled on an MS2 Viral Capsid Scaffold. *J. Am. Chem. Soc.*, 132(17):5936–5937, May 2010.

[58] Hervé Minoux and Christophe Chipot. Cation - π Interactions in Proteins: Can Simple Models Provide an Accurate Description? *Journal of the American Chemical Society*, 121(44):10366–10372, November 1999.

[59] Anurag Mishra, Giorgio Pariani, Thomas Oerther, Markus Schwaiger, and Gil G. Westmeyer. Hyperpolarized Multi-Metal 13C-Sensors for Magnetic Resonance Imaging. *Anal. Chem.*, 88(22):10790–10794, November 2016.

[60] Krishnan K. Palaniappan, R. Matthew Ramirez, Vikram S. Bajaj, David E. Wemmer, Alexander Pines, and Matthew B. Francis. Molecular Imaging of Cancer Cells Using a Bacteriophage-Based ^{129}Xe NMR Biosensor. *Angewandte Chemie International Edition*, 52(18):4849–4853, April 2013.

[61] Frederic N. R. Petersen, Morten Ø. Jensen, and Claus H. Nielsen. Interfacial Tryptophan Residues: A Role for the Cation-π Effect? *Biophysical Journal*, 89(6):3985–3996, December 2005.

[62] Reinhard Renneberg, Dorothea Pfeiffer, Fred Lisdat, George Wilson, Ulla Wollenberger, Frances Ligler, and Anthony P. F. Turner. Frieder Scheller and the Short History of Biosensors. *Advances in Biochemical Engineering/Biotechnology*, pages 1–18, 2008.

[63] Bill Retherford. The Machine that Can Read Your Mind. *Columbia Magazine*, 2019.

[64] Brittany A. Riggle, Mara L. Greenberg, Yanfei Wang, Rebecca F. Wissner, Serge D. Zemerov, E. James Petersson, and Ivan J. Dmochowski. A cryptophane-based turn-on ^{129}Xe NMR biosensor for monitoring calmodulin. *Organic & biomolecular chemistry*, 15(42):8883–8887, October 2017.

[65] Brittany A. Riggle, Yanfei Wang, and Ivan J. Dmochowski. A "Smart" ^{129}Xe NMR Biosensor for pH-Dependent Cell Labeling. *Journal of the American Chemical Society*, 137(16):5542–5548, April 2015.

[66] Benjamin W. Roose, Serge D. Zemerov, Yanfei Wang, Marina A. Kasimova, Vincenzo Carnevale, and Ivan J. Dmochowski. A Structural Basis for 129Xe Hyper-CEST Signal in

TEM-1 β-Lactamase. *ChemPhysChem*, 20(2):260–267, 2019. _eprint: https://chemistry-europe.onlinelibrary.wiley.com/doi/pdf/10.1002/cphc.201800624.

[67] Honor M. Rose, Christopher Witte, Federica Rossella, Stefan Klippel, Christian Freund, and Leif Schröder. Development of an antibody-based, modular biosensor for ^{129}Xe NMR molecular imaging of cells at nanomolar concentrations. *Proceedings of the National Academy of Sciences of the United States of America*, 111(32):11697–11702, August 2014.

[68] Ana M. Rossi and Colin W. Taylor. Analysis of protein-ligand interactions by fluorescence polarization. *Nat Protoc*, 6(3):365–387, March 2011.

[69] Vincent Roy, Thierry Brotin, Jean-Pierre Dutasta, Marie-Hélène Charles, Thierry Delair, François Mallet, Gaspard Huber, Hervé Desvaux, Yves Boulard, and Patrick Berthault. A Cryptophane Biosensor for the Detection of Specific Nucleotide Targets through Xenon NMR Spectroscopy. *ChemPhysChem*, 8(14):2082–2085, 2007.

[70] Hugo Sanabria, Michelle A. Digman, Enrico Gratton, and M. Neal Waxham. Spatial Diffusivity and Availability of Intracellular Calmodulin. *Biophysical Journal*, 95(12):6002–6015, December 2008.

[71] Andreas Schlundt, Wolfgang Kilian, Michael Beyermann, Jana Sticht, Sebastian Günther, Sabine Höpner, Kirsten Falk, Olaf Roetzschke, Lorenz Mitschang, and Christian Freund. A Xenon-129 Biosensor for Monitoring MHC–Peptide Interactions. *Angewandte Chemie*, 121(23):4206–4209, 2009.

[72] Matthias Schnurr, Karl Sydow, Honor May Rose, Margitta Dathe, and Leif Schröder. Brain Endothelial Cell Targeting Via a Peptide-Functionalized Liposomal Carrier for Xenon Hyper-CEST MRI. *Adv. Healthcare Mater.*, 4(1):40–45, January 2015.

[73] Matthias Schnurr, Ines Volk, Heike Nikolenko, Lars Winkler, Margitta Dathe, and Leif Schröder. Functionalized Lipopeptide Micelles as Highly Efficient NMR Depolarization Seed Points for Targeted Cell Labelling in Xenon MRI. *Advanced Biosystems*, 4(3):1900251, 2020. _eprint: https://onlinelibrary.wiley.com/doi/pdf/10.1002/adbi.201900251.

[74] Leif Schröder. Xenon for NMR biosensing – Inert but alert. *Physica Medica*, 29(1):3–16, January 2013.

[75] Benjamin M. Schulze, Davita L. Watkins, Jing Zhang, Ion Ghiviriga, and Ronald K. Castellano. Estimating the shape and size of supramolecular assemblies by variable temperature diffusion ordered spectroscopy. *Org. Biomol. Chem.*, 12(40):7932–7936, 2014.

[76] Igor N. Serdyuk, Nathan R. Zaccai, and Joseph Zaccai. *Methods in Molecular Biophysics: Structure, Dynamics, Function*. University Press, Cambridge, 2007. Book Title: Methods in Molecular Biophysics.

[77] Garry K. Seward, Qian Wei, and Ivan J. Dmochowski. Peptide-Mediated Cellular Uptake of Cryptophane. *Bioconjugate Chemistry*, 19(11):2129–2135, November 2008.

[78] Mikhail G. Shapiro, R. Matthew Ramirez, Lindsay J. Sperling, George Sun, Jinny Sun, Alexander Pines, David V. Schaffer, and Vikram S. Bajaj. Genetically encoded reporters for hyperpolarized xenon magnetic resonance imaging. *Nature Chemistry*, 6(7):629–634, July 2014. Number: 7 Publisher: Nature Publishing Group.

[79] Najeeb A Shirwany, Daniel Payette, Jun Xie, and Qing Guo. The amyloid beta ion channel hypothesis of Alzheimer's disease. *Neuropsychiatr Dis Treat*, 3(5):597–612, October 2007.

[80] Megan M. Spence, Seth M. Rubin, Ivan E. Dimitrov, E. Janette Ruiz, David E. Wemmer, Alexander Pines, Shao Qin Yao, Feng Tian, and Peter G. Schultz. Functionalized xenon as a biosensor. *Proceedings of the National Academy of Sciences*, 98(19):10654–10657, September 2001.

[81] Masatsugu Suzuki and Itsuko Suzuki. Lecture Note on Senior Laboratory Spin echo method in pulsed nuclear magnetic resonance (NMR). March 2011.

[82] F. D. Sönnichsen, J. E. Van Eyk, R. S. Hodges, and B. D. Sykes. Effect of trifluoroethanol on protein secondary structure: an NMR and CD study using a synthetic actin peptide. *Biochemistry*, 31(37):8790–8798, September 1992.

[83] Olena Taratula, P. Aru Hill, Najat S. Khan, Patrick J. Carroll, and Ivan J. Dmochowski. Crystallographic observation of 'induced fit' in a cryptophane host–guest model system. *Nature Communications*, 1(1):148, December 2010.

[84] Philipp O. Tsvetkov, Irina I. Protasevich, Robert Gilli, Daniel Lafitte, Vladimir M. Lobachov, Jacques Haiech, Claudette Briand, and Alexander A. Makarov. Apocalmodulin Binds to the Myosin Light Chain Kinase Calmodulin Target Site. *J. Biol. Chem.*, 274(26):18161–18164, June 1999.

[85] Najl V. Valeyev, Declan G. Bates, Pat Heslop-Harrison, Ian Postlethwaite, and Nikolay V. Kotov. Elucidating the mechanisms of cooperative calcium-calmodulin interactions: a structural systems biology approach. *BMC Systems Biology*, 2:48, 2008.

[86] Thad G. Walker and William Happer. Spin-exchange optical pumping of noble-gas nuclei. *Rev. Mod. Phys.*, 69(2):629–642, April 1997. Publisher: American Physical Society.

[87] Yanfei Wang and Ivan J. Dmochowski. Cucurbit[6]uril is an ultrasensitive ^{129}Xe NMR contrast agent. *Chemical Communications*, 51(43):8982–8985, May 2015.

[88] Qian Wei, Garry K. Seward, P. Aru Hill, Brian Patton, Ivan E. Dimitrov, Nicholas N. Kuzma, and Ivan J. Dmochowski. Designing ^{129}Xe NMR Biosensors for Matrix Metalloproteinase Detection. *Journal of the American Chemical Society*, 128(40):13274–13283, October 2006.

[89] James N. Weiss. The Hill equation revisited: uses and misuses. *The FASEB Journal*, 11(11):835–841, 1997. _eprint: https://faseb.onlinelibrary.wiley.com/doi/pdf/10.1096/fasebj.11.11.9285481.

[90] Christopher Witte, Vera Martos, Honor May Rose, Stefan Reinke, Stefan Klippel, Leif Schröder, and Christian P. R. Hackenberger. Live-cell MRI with Xenon Hyper-CEST Biosensors Targeted to Metabolically Labeled Cell-Surface Glycans. *Angewandte Chemie International Edition*, 54(9):2806–2810, 2015. _eprint: https://onlinelibrary.wiley.com/doi/pdf/10.1002/anie.201410573.

[91] Jan Wolber, Ian J. Rowland, Martin O. Leach, and Angelo Bifone. Perfluorocarbon emulsions as intravenous delivery media for hyperpolarized xenon. *Magnetic Resonance in Medicine*, 41(3):442–449, 1999. _eprint: https://onlinelibrary.wiley.com/doi/pdf/10.1002/%28SICI%291522-2594%28199903%2941%3A3%3C442%3A%3AAID-MRM3%3E3.0.CO%3B2-7.

[92] Xu Wu and Donald M. Bers. Free and Bound Intracellular Calmodulin Measurements in Cardiac Myocytes. *Cell Calcium*, 41(4):353–364, April 2007.

[93] Pengfei Xu, Zhiwei Shen, Baolin Zhang, Jun Wang, and Renhua Wu. Synthesis and characterization of superparamagnetic iron oxide nanoparticles as calcium-responsive MRI contrast agents. 389:560–566, December 2016.

[94] Bei Yang and Michael J. Bouchard. The Hepatitis B Virus X Protein Elevates Cytosolic Calcium Signals by Modulating Mitochondrial Calcium Uptake. *J Virol*, 86(1):313–327, January 2012.

[95] Serge D. Zemerov, Benjamin W. Roose, Mara L. Greenberg, Yanfei Wang, and Ivan J. Dmochowski. Cryptophane Nanoscale Assemblies Expand 129Xe NMR Biosensing. *Analytical Chemistry*, June 2018.

[96] Yudong Zhang, Zhengchao Dong, Shuihua Wang, Genlin Ji, and Jiquan Yang. Preclinical Diagnosis of Magnetic Resonance (MR) Brain Images via Discrete Wavelet Packet Transform with Tsallis Entropy and Generalized Eigenvalue Proximal Support Vector Machine (GEPSVM). *Entropy*, 17(4):1795–1813, April 2015. Number: 4 Publisher: Multidisciplinary Digital Publishing Institute.

[97] Yubin Zhou, Teryl K. Frey, and Jenny J. Yang. Viral calciomics: interplays between Ca2+ and virus. *Cell Calcium*, 46(1):1–17, July 2009.